

The University of Wisconsin Library
Manuscript Theses

Unpublished theses submitted for the Master's and Doctor's degrees and deposited in The University of Wisconsin Library are open for inspection, but are to be used only with due regard to the rights of the authors. Bibliographical references may be noted, but passages may be copied only with the permission of the authors, and proper credit must be given in subsequent written or published work. Extensive copying or publication of the thesis in whole or in part requires also the consent of the Dean of the Graduate School of The University of Wisconsin.

This thesis by Karen Lynn Byrum
has been used by the following persons, whose signatures attest their acceptance of the above restrictions.

A Library which borrows this thesis for use by its patrons is expected to secure the signature of each user:

NAME AND ADDRESS

DATE

A dissertation entitled

The Lepton Charge Asymmetry From W_{\pm} goes to μ on \pm Neutrino
Using Forward Muons at the Collider Detector at Fermilab

submitted to the Graduate School of the
University of Wisconsin-Madison
in partial fulfillment of the requirements for the
degree of Doctor of Philosophy

by

Karen Lynn Byrum

Degree to be awarded: December 19__ May 19 92 August 19__

Approved by Dissertation Readers:

Lee G. Pondrom

December 20, 1991

Major Professor

Date of Examination

David C. Williams

Francis Halzen

John H. Wiley
Dean, Graduate School

THE LEPTON CHARGE ASYMMETRY
FROM $W^\pm \rightarrow \mu^\pm \nu$
USING FORWARD MUONS AT THE
COLLIDER DETECTOR AT FERMILAB
by
K BYRUM

A thesis submitted in partial fulfillment of the
requirements for the degree of

DOCTOR OF PHILOSOPHY
(Physics)

at the
UNIVERSITY OF WISCONSIN - MADISON

1992

Abstract

This thesis is the first observations of forward-backward muon events from $W^\pm \rightarrow \mu^\pm \nu$ decays in $p\bar{p}$ collisions at $\sqrt{s}=1.8\text{TeV}$. These events were collected by the Collider Detector at Fermilab during the 1988-89 run and were used to measure the lepton charge asymmetry. An asymmetry of $-.06 \pm .27 \pm .01$ was measured where the .27 was the statistical uncertainty and the .01

Acknowledgements

First, I want to thank my advisor, Lee Pondrom for giving me the chance to become a particle physicist and for his continued support.

I want thank to Chris Wendt for his belief in my work, especially back in the early days when my analysis seemed hopeless. I still remember his pragmatic attitude back then of "it's only a machine". I want to thank both Chris and Jodi Lamoureux for all those little calibration, data-set creation, monte-carlo creation, etc... jobs that seemed to go on for an eternity.

I thank both John Skarha and Duncan Carlsmith for laying the groundwork for all forward muon analyses.

I want to thank Chris and Jodi for knowing how to have a "good time". I mean if it wasn't for Chris, how frequently would we have slam danced our way through the Urbana house? If it wasn't for Jodi, would you have ever danced with an inflatable cow? Actually, when it comes to having a good time, the list is quite long. I want to thank the "Urbana Boys" for being themselves (Hovhannes, Phil and Vic). No party has quite matched those held at the Urbana house, Brian,

Les, Tiny, Paul, Sandra, Brenna, Tom, David, John, Mikio, Satoru, Keith, Steve, Dee, Colin, Steve, Bob, Tom and anyone else that ever came.

I want to thank Leigh for Lorenzo and Juliano and to thank Jodi, Leigh, Carol, Ed, Liz, Bob, and anybody else that helped Callie, Fatboy, Apollo, Teggers, and Marina live.

I want to thank Erik for listening to all my gripes. Being the emotional vampire I am, it musta been tough.

I thank Beverly June for continually pulling me back into the world of relationships and emotions. I always feel renewed and more alive following a conscious dip in that world. Finally, I thank my parents and brother and sister for their love and support. There's nothing quite like family.

This work was supported by the United States Department of Energy
Contract DE-AC02-76ER00881.

Contents

Abstract	ii
Acknowledgements	iii
1 Introduction	1
1.1 Overview: The Standard Model	2
1.1.1 Fermions and Bosons	2
1.1.2 Interactions	4
1.2 The Parton Model and Structure Functions	6
1.3 Hadronic W Boson Production	9
1.3.1 General Features	9
1.3.2 The Inclusive Rapidity Distribution	11
1.3.3 Kinematics	14
1.4 $W \rightarrow \mu\nu$ Decay	15
1.5 Asymmetry Effects Due to Higher Order Corrections	19

2	Apparatus	24
2.1	The Tevatron Collider	24
2.2	The CDF Detector	27
2.2.1	The CDF Tracking Chambers	28
2.2.1.1	The Vertex Time Projection Chambers	28
2.2.1.2	The Central Tracking Chambers	32
2.2.2	Calorimeters	34
2.2.2.1	Gas Calorimeters	34
2.2.2.2	Endplug Electromagnetic Calorimeter	35
2.2.2.3	Endplug Hadron Calorimeter	35
2.2.2.4	Forward Electromagnetic Calorimeter	36
2.2.2.5	Forward Hadron Calorimeter	36
2.2.3	The CDF Level0 Trigger - Beam Beam Counters	37
2.3	The Forward Muon (FMU) System	38
2.3.1	The FMU Apparatus	38
2.3.2	The FMU Toroids	40
2.3.3	The FMU Drift Chambers	40
2.3.4	The FMU Scintillator Counters	44
2.3.5	The FMU Trigger	44
2.3.5.1	The HOPU Trigger Boards	45
2.3.5.2	The NUPU Trigger Boards	48
2.3.5.3	The Level1 Geometric Trigger Efficiency	50

2.3.5.4	FMU Level2 and Level3 Triggers	51
2.3.5.5	Detector Contributions to the Trigger Efficiencies	51
2.3.5.6	Group Failures and Single Chamber Losses	55
2.3.5.7	Single Wire Efficiencies	55
2.3.5.8	Trigger Electronics Efficiency	56
2.3.5.9	Losses Due to Scintillator Efficiencies	56
2.3.6	The FMU Luminosity	57
2.3.7	The FMU Momentum Resolution	58
3	The Inclusive Forward/Backward Muons	65
3.1	Introduction	65
3.2	The FMU Inclusive Data	65
3.3	Cut Efficiencies	68
3.3.1	The Calorimetry Cut	68
3.3.2	Six Hit Fit satisfying a 1-1-1 Road	71
3.3.3	The Track Fit $P(\chi^2)$ Cut	72
3.3.4	The Maxhit Cut	73
3.3.5	Fake Muon Contamination	77
3.3.6	Overall Efficiencies	80
3.4	Simulations	81
3.4.1	Decay-in-flight Spectrum	81
3.4.2	$W^\pm \rightarrow \mu^\pm \nu$ and $Z^0 \rightarrow \mu^+ \mu^-$ Spectra.	82

3.4.3	Bottom and Charm Decays	83
3.4.4	Detector Effects	83
3.4.5	Computer Codes	85
3.5	Comparison of Simulation to Data	86
3.5.1	East/West and +Q/-Q Asymmetries in the Data.	86
3.5.2	The dN/dP_t and $dN/d\eta$ Distributions	87
3.6	Results	92
4	The FMU $W^\pm \rightarrow \mu^\pm \nu$ Spectrum	100
4.1	Introduction	100
4.2	W Data Selection	100
4.2.1	The Isolation Cut.	101
4.3	Backgrounds	101
4.4	The Simulated Isolated Decay-in-flight Spectrum	103
4.5	High P_t decay-in-flight Muons.	104
4.6	Low P_t decay-in-flight Muons.	105
4.6.1	Enrichment Cuts	105
4.6.2	Fitting for the Background Fraction.	115
4.6.3	Uncertainties in the fitted background fraction	117
4.6.4	Cross-Checks on our Background Estimate	119
4.7	$Z \rightarrow \mu\mu$	123
4.8	QCD Background	125

4.9	Results	127
5	The Asymmetry Measurement	130
5.1	Trigger Bias For Low Statistics.	132
5.2	Charge Bias in Track Reconstruction and Tracking Cuts	135
5.3	Background Distributions	136
5.4	The Asymmetry.	139
5.5	The Asymmetry Error	140
5.6	Corrections to the Asymmetry	143
5.6.1	Higher Order Corrections.	143
5.6.2	Mismeasured Charged Tracks	146
5.7	CDF Asymmetry Results from other Detector Regions.	148
5.8	Conclusions	149
A	Efficiency of the Forward Muon $P(\chi^2)$ Cut	155
A.1	Introduction	155
A.2	Z^0 Data Compared to Simulation	156
A.3	Minimum Bias Data Compared to Simulation	158
A.4	Muon-In-Jet Data Compared to Simulation	163
A.5	Conclusion	165
B	Delta rays, photon conversions, bremsstrahlung and other physics processes responsible for the production of extra hits in the FMU	

drift cells	174
B.1 Origins	175
B.2 Multiplicity Distributions	179
B.3 Spatial Distributions	181
B.3.1 $\Delta\phi$ Distributions	181
B.3.2 ΔR Distributions	183
C The Predicted Decay in Flight Spectrum	187
C.1 The FMU Decay In Flight Normalization	187
C.2 The FMU $d\sigma/dP_t^\mu$ Distribution	192
C.3 The FMU $d\sigma/d\theta$ Distribution	194

List of Tables

2.1	FMU trigger configurations and associated luminosity for the 1988-89 CDF run	53
2.2	Contributions to the efficiency from detector components.	54
2.3	Momentum Resolution for Multiple Scattering, Chamber Resolution and Survey Uncertainties.	59
3.1	Efficiencies for finding a muon or random tower which passes a minimum energy requirement	71
3.2	Efficiencies for finding a muon which passes a maximum number of allowed FMU TDC hits in the trigger octant.	77
3.3	Efficiency of Inclusive Muon cuts	81
3.4	Ratio of East/West Values using Efficiencies and Data.	87
4.1	Upper limit on background from decay-in-flight muons with $P_t > 10\text{GeV}/c$, in the W signal region. The additional cuts on $P(\chi^2)$ and $ \eta $ are discussed in section 5.	105

4.2	Breakdown of event counts in two regions of P_t and two regions of η , used to fit for signal and background components in the data. .	115
4.3	Final Number of decay-in-flight muons and W muons as determined from the least squares fit. The number of CDF 1988-89 data events is also listed.	118
4.4	Systematic Uncertainty on Minimum Bias Background in FMU region $22 < P_t < 75$, $ \eta < 2.4$ and $P(\chi^2) > .02$	118
4.5	Number of Events with $P_t > 75\text{GeV}/c$ passing cuts in $ \eta < 2.4$ region and passing $P(\chi^2) > .02$	123
4.6	Z^0 Background	126
4.7	Measured number of forward muons	129
5.1	The predicted lepton asymmetry from the PAPAGENO monte carlo and after a forward muon detector simulation which includes trigger effects.	133
5.2	The average trigger efficiency for a specified mean P_t	134
5.3	Charge independence of the $P(\chi^2)$ cut.	137
5.4	Minimum bias Background for different asymmetry bins.	138
5.5	Z^0 Background for different asymmetry bins.	139
5.6	Summary of the number of observed events in each bin, the number of Z^0 background events and the efficiencies used for computing the asymmetry and the asymmetries themselves.	141

5.7	Weights for each partial derivative term used for computing the asymmetry error.	142
5.8	The error on the statistical error of the asymmetry is shown by varying the background fraction by one standard deviation.	143
5.9	The statistical and systematic errors to the lepton asymmetry.	144
5.10	Probability of fitter to mismeasure the charge.	148
A.1	A Comparison of the Efficiency of the χ^2 Probability Cut for the Z^0 Data to the Simulation.	158
A.2	The Efficiency of the χ^2 Probability Cut for Simulated W muon decays as different simulated processes are included.	159
A.3	The fraction of event passing $P(\chi^2) > .05$ both as a function of the measured muon P_t and as a function of the generated P_t for minimum bias events.	164
A.4	The efficiency of the $P(\chi^2)$ probability cut as a function of the measured muon P_t for both triggered and volunteer muon in jet events.	166
B.1	Percentage of extra hits which are correlated or uncorrelated produced in either the iron or in the chamber walls	177
B.2	Fraction of events that have extra hits	180
B.3	Fraction of extra hits that are correlated with other extra hits.	180

B.4	Parameterization of equations describing the radial spatial distributions for the 3 cases mention above.	186
C.1	Constants used in the decay in flight formula.	189
C.2	Integral inclusive cross section for various P_t^μ thresholds.	193

List of Figures

1.1	Parton model of a hadron-hadron reaction	7
1.2	a.)Quark structure functions extracted from an analysis of deep inelastic scattering data. b.)Shows the total valence and sea quark contributions to the structure of the proton.	9
1.3	$F_2(x, Q^2)$ vs Q^2 at different x values	10
1.4	W production cross section at Tevatron	12
1.5	Rapidity distribution of W^+ production at Tevatron	13
1.6	Asymmetry of the rapidity distribution for W^+ production at Tevatron	13
1.7	Schematic representation of $W \rightarrow \mu\nu$	16
1.8	Lepton Asymmetry as a function of Lepton Rapidity	18
1.9	Lepton Asymmetry as a function of Lepton Rapidity for different M_t cuts. Each contour represents a M_t bin of 2.5GeV.	20
1.10	Annihilation graphs	21
1.11	Compton graphs	21

1.12	K-factor vs W Rapidity	22
2.1	An Overhead View of the Fermilab Accelerator Complex	25
2.2	Perspective View of the CDF Detector	29
2.3	Side View of the CDF Detector	30
2.4	Two of the eight vertex time projection chambers modules	31
2.5	R- ϕ view of the CTC.	33
2.6	A beam's-eye view of one of the beam-beam counter planes.	39
2.7	FMU Drift Field Configuration. a.) Initial field line configuration. b.) Equilibrium field line configuration.	41
2.8	The components for the forward muon front detector plane are shown.	43
2.9	Schematic of the forward muon electronics during the 1988-89 CDF run.	46
2.10	Allowed hit patterns for DI-HOPU trigger boards.	47
2.11	Allowed hit patterns for NUPU trigger boards.	49
2.12	Trigger efficiency for wire 32 compared to the other wires.	51
2.13	NUPU 50 Trigger Efficiency	52
2.14	Average FMU Level1 Rate vs Average Integrated Luminosity	58
2.15	Schematic of FMU survey procedure	61
2.16	Cumulative Momenta Resolution vs Momenta	62
2.17	FMU - CMU Z^0 Invariant Mass $\langle GeV \rangle$	64

3.1	Energy distributions for inclusive forward muon events.	70
3.2	The $P(\chi^2)$ distribution and the Maxhit vs Muon azimuth scatter plot for forward muon events.	75
3.3	Maxhit Distribution for forward muons from FMU-CMU Z^0 candidates.	76
3.4	Strip Pad Distributions for Inclusive Muon Events a.) 1x1 tower centered on muon. b.) 1x1 tower centered on $\phi \pm 180^\circ$ from muon. c.) 1x3 tower centered on muon. d) 1x3 tower centered on $\phi \pm 180^\circ$.	79
3.5	$d\sigma/dP_t$ input muon spectrum	84
3.6	P_t and η distributions comparing data yields for the east and west sides of detector. a.)uncorrected P_t b.) corrected P_t c.)uncorrected η d.) corrected η	88
3.7	Inclusive Ratio of +Q/-Q compared to simulation	89
3.8	dN/dP_t distribution for inclusive forward muons compared to simulated processes.	93
3.9	dN/P_t distribution for inclusive forward muons compared to the sum of simulated processes.	94
3.10	$dN/d\eta$ distribution for inclusive forward muons compared to simulated processes.	95
3.11	$dN/d\eta$ distribution for inclusive forward muons compared to the sum of simulated processes.	96

3.12	dN/dP_t charged particle spectrum obtained from special stiff track trigger runs taken in the 1988-89 period.	97
3.13	dN/dP_t distribution for inclusive forward muons compared to the sum of the simulated processes including the uncertainties.	98
3.14	Corrected $dN/d\eta$ distribution for inclusive forward muons compared to the sum of the simulated processes including the uncertainties.	99
4.1	Distribution of E_t in a cone of $R = .55$ for FMU-CMU Z^0 candidates.	102
4.2	Distribution of reconstructed P_t for a simulation of low P_t decay-in-flight muons compared to the prediction for W events and to the CDF 1988-89 data. A minimum muon P_t of 2GeV/c is used.	107
4.3	Distribution of pseudorapidity for a simulation of low P_t decay-in-flight muons compared to the prediction for W events and to the CDF 1988-89 data. A minimum muon P_t of 2GeV/c is used.	108
4.4	Schematic of bend and sagitta definitions.	110
4.5	$P(\chi^2)$ distribution for low P_t decay-in-flight simulation, a.) W simulation. b.) minimum bias simulation. c.) CDF 88-89 data.	111
4.6	Distribution of reconstructed P_t for a simulated low P_t decay-in-flight muons compared to prediction for W events and to the CDF 1988-89 data,	113

4.7	Distribution of pseudorapidity for simulated low P_t decay-in-flight muons compared to the prediction for W events and to the CDF 1988-89 data,	114
4.8	$P(\chi^2)$ for muons with $22 < P_t < 75\text{GeV}/c$, $ \eta < 2.4$ and $P(\chi^2) > .02$. 120	
4.9	P_t Distribution for muons with $P_t > 18\text{GeV}/c$, $ \eta < 2.4$ and $P(\chi^2) > .02$. 121	
4.10	Pseudorapidity distribution for muons with $22 < P_t < 75\text{GeV}/c$, $ \eta < 2.8$ and $P(\chi^2) > .02$	122
4.11	Azimuthal separation between muon and the leading jet for events with a jet satisfying $E_t > 10\text{GeV}$. a.) CDF W candidates; b.) CDF non-isolated FMU sample; c.) Papageno events normalized to CDF W candidates.	128
5.1	Schematic of Trigger Detector Effects to W Decay Asymmetry. . .	150
5.2	Forward Muon Lepton Asymmetry compared to Zeroth order theory Predictions.	151
5.3	Forward Muon $P_t(W)$ Distribution (GeV/c)	152
5.4	Forward Muon Lepton Asymmetry as a function of $P_t(W)$ for the rapidity interval $2 < \eta < 2.4$ and $P_t^\mu > 22\text{GeV}/c$	153
5.5	CDF Lepton Asymmetry compared to Zeroth order theory Predictions.	154

A.1	The χ^2 distribution from the simulated data set of $Z \rightarrow \mu\mu$ a.) for 3 degrees of freedom. b.) for 4 degrees of freedom. A comparison between monte carlo and CDF 88-89 data c. χ^2 d. $P(\chi^2)$	168
A.2	Event Quantities for the CDF 88-89 Minimum Bias Data Set. . .	169
A.3	The χ^2 distribution from the minimum bias simulated data a.) for 4 degrees of freedom. b.) for badly mismeasured events. A comparison between monte carlo and CDF 88-89 data c. χ^2 d. $P(\chi^2)$	170
A.4	Fraction of events passing the $P(\chi^2) > .05$ for different minimum bias spectrum shapes.	171
A.5	Fraction of events passing the $P(\chi^2) > .05$ for different scattering and extra hit models.	172
A.6	Event Quantities for the CDF 88-89 Muon-in-Jet Data Set.	173
B.1	Vertex Positions for Extra Hits in units of cm. a.) Front Plane Z positions. b.) Front Plane X,Y positions. c.) Mid Plane Z positions. d.) Rear Plane Z positions.	176
B.2	Momentum distribution for extra hits originating in either the chamber walls (figures a., c. and e.) or the iron (figures b., d., and f.)	178

Chapter 1

Introduction

The Tevatron proton-antiproton collider at Fermilab (CDF), operating at $\sqrt{s} = 1.8$ TEV, provides the world with the highest center of mass energy to study fundamental physics processes. It is the thrust of this thesis to measure $W^\pm \rightarrow \mu^\pm \nu$ decays and extract a lepton asymmetry measurement. The lepton asymmetry can be used in one of two measurements. One can assume the parton densities in the incident hadrons are well measured by other experiments and test the standard model $(V - A)$ coupling of the weak force, or one can assume the standard model $(V - A)$ coupling is correct and measure the parton densities. A measurement of the parton densities at values of x and Q^2 where W 's and Z^0 's are produced could lead to improved predictions for $\sigma(W)/\sigma(Z)$ [1] [2]. (where x is the average fractional momenta carried by the quarks and Q^2 is the center of mass energy of the interaction).

This thesis is based on data taken during the CDF 1988-89 run using forward-backward muon triggers. The forward- backward muon chambers cover the angular regions between $7^\circ - 16^\circ$ and $164^\circ - 173^\circ$. The 1988-89 CDF run marks the first observation of forward-backward W production. In the remainder of this chapter, the theoretical motivation of this thesis will be discussed.

1.1 Overview: The Standard Model

The current physical theory of physics postulates the universe as we know it to be composed of two kinds of particles, fermions and bosons and four fundamental interactions, gravitational, electromagnetic, weak and strong. Fermions are the constituents of matter and are pointlike spin $\frac{1}{2}$ objects. Bosons have integral spin and are the carriers of the quanta for the fundamental interactions. These interactions, with the exception of gravity, can be described by renormalizable gauge invariant theories. The theories use currents to describe how fermions interact with each other by the emission or absorption of gauge bosons.

1.1.1 Fermions and Bosons

The fermions can be grouped into doublets of three families of quarks and leptons with each successive family being more massive. Each fermion also has an accompanying anti-particle associated with it. The masses are not predicted by theory, but are measured experimentally. The neutrino masses are zero or close

to zero with current limits setting the $M_{\nu_e} < 18$ eV [3]. The three families of leptons and quarks are shown below:

$$\begin{pmatrix} \nu_e \\ e \end{pmatrix} \begin{pmatrix} \nu_\mu \\ \mu \end{pmatrix} \begin{pmatrix} \nu_\tau \\ \tau \end{pmatrix}$$

$$\begin{pmatrix} u \\ d \end{pmatrix} \begin{pmatrix} s \\ c \end{pmatrix} \begin{pmatrix} t \\ b \end{pmatrix}$$

With the exception of the (t) top quark, all of the fermions listed have been observed. The present limit on the mass of the top quark as measured at CDF was found to be $M_t > 89$ GeV/ c^2 [4].

The fundamental difference between leptons and quarks is their behavior under the interactions. The leptons are blind to the strong interaction whereas the quarks participate in all four interactions. A fourth family is in principle possible, however recent experiments at e^+e^- colliders have ruled out the possibility of a fourth neutrino unless its mass is in excess of ~ 30 GeV/ c^2 [5]. The fractionally charged quarks combine to produce particles of integer charge. These composite particles called hadrons come in two types of combinations of quarks, mesons which are composed of a quark and an anti-quark and baryons which are composed of either three quarks or three anti-quarks. The quark model is able to explain the abundance of subatomic particles in the same way as the atomic model explains the Periodic Table of elements.

1.1.2 Interactions

All charged particles participate in the electromagnetic interaction which is described by the field theory of quantum electrodynamics (QED). The boson mediator is the massless neutral spin 1 photon which couples to electric charge through a vector current.

The strong interaction is described by the field theory of quantum chromodynamics (QCD). A strong "color charge" is carried by quarks as well as the mediators of the strong force, the gluons. This "color charge" is the quantity which is conserved. There are three colors of strong charge, commonly referred to as red, green, and blue as well as three anti-colors used to describe the anti-particles. Eight massless neutral colored gluons mediate the strong interaction. The strong interaction combines quarks in such a way as to produce the colorless baryons and mesons.

The weak interaction was first observed in nuclear β decay, but the development of a complete weak theory didn't occur until the 1960's when Glashow, Weinberg and Salam (GWS) proposed the electroweak theory which unified the electromagnetic and weak interactions. The mediators of the weak interaction are massive spin 1 bosons known as the W^+ , W^- and Z^0 . The fundamental fermions carry a "weak charge" also known as isospin and it is this weak charge which the massive bosons couple to. However, one of the peculiarities of the weak interaction is the fact that charged bosons couple only to the left handed fermions. The

"left handedness" refers to the helicity of the fermion which can have its helicity aligned along the direction of its motion (referred to as "right handed") or the fermion can have its helicity aligned opposite to its direction of motion (referred to as "left handed"). This is known as the $V - A$ axial vector current of the weak interaction. One of the unanswered questions of particle physics is why the weak charged current interaction couples to only left handed fermions.

The unification of the electromagnetic and weak interactions, commonly called the "electroweak" theory, is described by the renormalizable $SU(2)_{left} \times U(1)$ non-abelian gauge field theory proposed by Glashow, Weinberg and Salam. This theory, when combined with QCD, is commonly referred to as the Standard Model. In electroweak theory, the bosons are described by a massless isovector triplet and a massless isosinglet.

$$\begin{aligned} W_\mu &= W_\mu^1 W_\mu^2 W_\mu^3 \\ &B_\mu \end{aligned} \tag{1.1}$$

Through a process known as Spontaneous Symmetry Breaking (SSB), three of the bosons acquire mass while the fourth boson remains massless in such a way that the renormalizability of the theory is maintained. The effect of SSB is essentially to demand a preferred direction in weak isospin space such that a linear combination of the neutral bosons above become the physically distinct mass eigenstates which we measure in the laboratory. The weak mixing angle θ_W

describes how the bosons transform into the observed mass eigenstates.

$$\begin{array}{ccc} W^+ & W^- Z^0 & \text{Weak Bosons} \\ & \gamma & \text{Photon} \end{array} \quad (1.2)$$

As a result of this model, the weak boson masses were predicted in terms of θ_W and eventually discovered at CERN in 1983 [6]. Weak interactions are allowed to couple across generations and this mixing is described by the Kobayashi-Maskawa (K-M) matrix [7]; however, there is no direct evidence of mixing between lepton families. This is not too surprising since in the limit of zero neutrino mass, lepton mixing is prohibited.

One final feature of the electroweak model is the introduction of the Higgs boson. This spin 0 boson is required by the SSB process to give the weak bosons mass. The Higgs particle has yet to be discovered and the theory makes no predictions for its mass. However, the theory does predict an upper bounds on the Higgs mass.

1.2 The Parton Model and Structure Functions

Bjorken's parton model states that the nucleon is composed of pointlike components called partons [8]. These have since been identified as quarks. The proton is described as three valence quarks accompanied by many quark-antiquark pairs. These quark-antiquark pairs are known as the "sea" quarks. The sea quarks are thought to be radiated by the valence quarks so that to a first approximation,

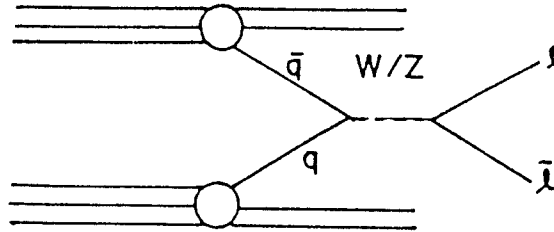


Figure 1.1: Parton model of a hadron-hadron reaction

the three lightest flavors are assumed to occur with roughly the same frequency and momentum distributions. The charm and heavier quarks are neglected with the assumption that they will be a small contribution to the sea quarks. In a $p\bar{p}$ collision which produces a W boson, one single parton in the proton collides with a single parton in the antiproton. The remaining partons, called spectator partons, do not participate in the interaction. Very generally, the parton model representation of a hadron-hadron reaction is shown in figure 1.1. The cross section for this reaction can be expressed schematically as

$$d\sigma(q + \bar{q} \rightarrow W + X) = \sum_{i,j} f_i^{(q)} f_j^{(\bar{q})} d\hat{\sigma}(i + j \rightarrow W + X') \quad (1.3)$$

where $d\hat{\sigma}$ is the parton level subprocess cross section which can be, in principle, calculated from theory. The f_i 's are defined to be the parton probability distribution functions which predict the probability of finding a parton of a given species (i) inside the proton. The parton probability distributions are used to describe the parton structure functions which are the distributions measured at deep inelastic experiments (DIS). The quark and antiquark structure functions can be written.

$$q_i(x_l, Q^2) = x f_i(x_l, Q^2) \quad (1.4)$$

where $i = u\bar{u}d\bar{d}s\bar{s}c\bar{c}\dots$. The summed over quarks contain both valence and sea contributions. The gluon structure function is written similarly

$$g(x_l, Q^2) = x f_g(x_l, Q^2). \quad (1.5)$$

Once the parton probability distribution at some value of Q^2 is known, the momentum transferred dependence can be calculated using the theory of QCD.

Common to most literature is the definition of the F_2 structure function which is just a sum over equation 1.4. The structure functions cannot be calculated theoretically, rather algorithms are used to predict $q_i(x_l, Q^2)$ for any i, x, Q based on experimental data. Commonly used fits to the data are those of Eichten-Hinchliff-Lane-Quigg (EHLQ) [9] and Martin-Roberts-Stirling (MRS) [10]. Figure 1.2 shows the quark structure functions extracted from an analysis of deep inelastic scattering data [8]. The Q^2 dependence of structure functions is predicted by QCD via the Altarelli-Parisi equations [11] [8]. This dependence is logarithmic and comes about due to gluon bremsstrahlung. Figure 1.3 shows how the F_2 structure function increases at small x with increases Q^2 from CERN data. [8] Using the formalism of the Altarelli-Parisi equation, a structure function measured at a particular value of $Q^2 = Q_0^2$ can be evolved to any value of Q^2 .

EHLQ structure functions are based on DIS experimental data from the early 1980's using lowest order QCD evolution. MRS structure functions are from newer experimental data (mid 1980's) and use the next to lowest order QCD evolution. DIS experiments are able to put errors of approximately 10 % on

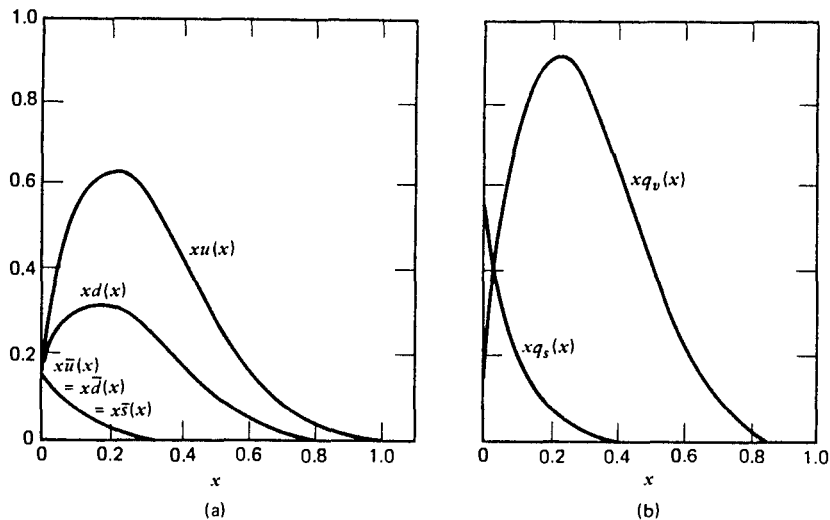


Figure 1.2: a.) Quark structure functions extracted from an analysis of deep inelastic scattering data. b.) Shows the total valence and sea quark contributions to the structure of the proton.

the quark and antiquark structure functions. The errors on the gluon structure functions are much larger since the weak and the electroweak DIS probes do not couple to gluons. However, the gluon field carries at least half of the net momentum of the parton as determined from measurements of the charged protons momenta [12].

1.3 Hadronic W Boson Production

1.3.1 General Features

Weak bosons are produced in hadronic collisions by annihilation of a quark-antiquark pair. Because of the $(V - A)$ coupling of the weak force, the W bosons

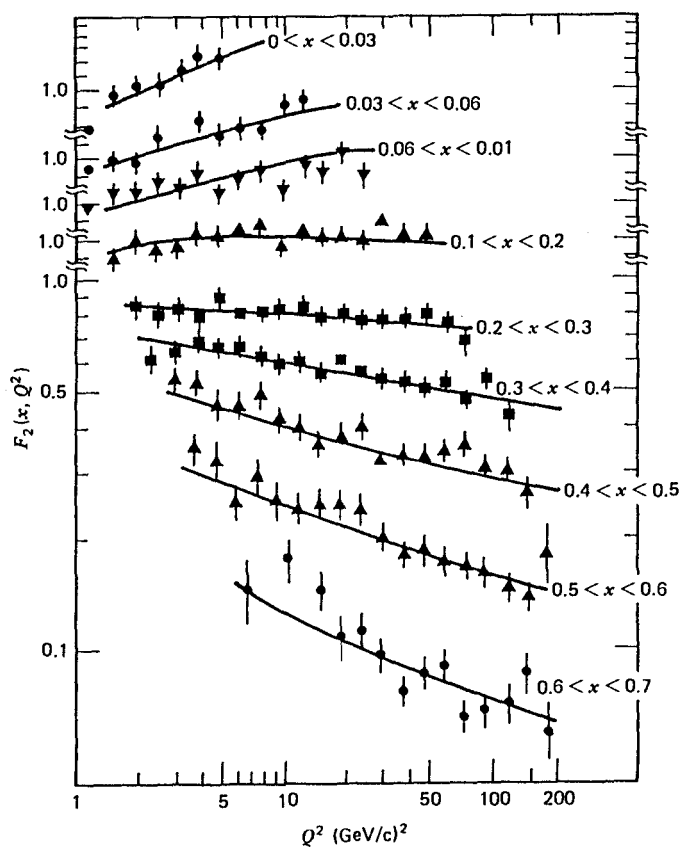


Figure 1.3: $F_2(x, Q^2)$ vs Q^2 at different x values

are predicted to be almost fully polarized along the anti-proton direction. At $\sqrt{s} = 1800$ GeV more than 85% of the W 's are created by valence-valence plus valence-sea interactions as shown in figure 1.4 [2]. For these interactions, the basic processes involved in forming a W as predicted by the standard model are:

$$\begin{aligned} u + \bar{d} &\rightarrow W^+ \quad \text{or} \quad u + \bar{s} \rightarrow W^+ \\ d + \bar{u} &\rightarrow W^- \quad \text{or} \quad s + \bar{u} \rightarrow W^- \end{aligned} \quad (1.6)$$

The left processes are the most common, with a u (\bar{u}) quark from the proton (antiproton) and with a \bar{d} (d) from the antiproton (proton). The sea (s) quarks in the above processes are mostly sea strange quarks. The charm quark content is expected to contribute about 4% at $\sqrt{s} = 1800$ GeV and the contribution from the heavier b and t sea quarks is believed to be negligible [2].

1.3.2 The Inclusive Rapidity Distribution

Since u quarks are known to have, on average, higher momentum than d quarks, the W^+ 's tend to be boosted in the proton direction while W^- 's tend to be boosted in the antiproton direction. A useful variable for describing the direction of W production is the rapidity variable. It is defined as

$$y = \frac{1}{2} \log\left(\frac{E^W + P_z^W}{E^W - P_z^W}\right) \quad (1.7)$$

where E^W is the energy of the W boson and P_z^W is the longitudinal component of the momentum. Using this variable, the inclusive rapidity distribution for

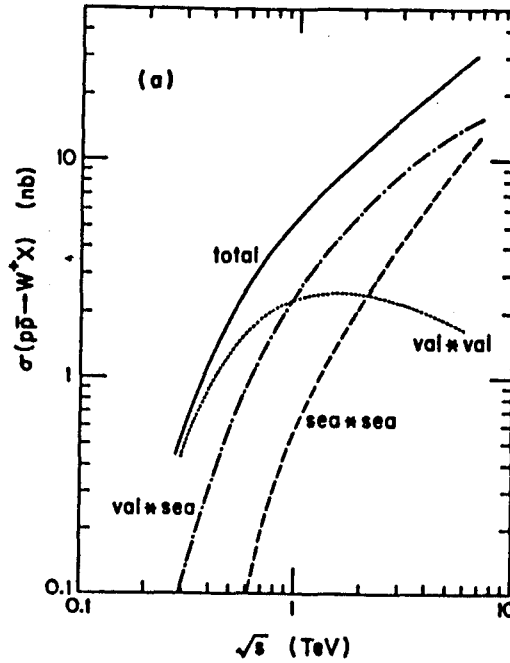


Figure 1.4: W production cross section at Tevatron

production of a W^+ is shown in figure 1.5 [2]. As observed in this figure, the shape of the distribution depends on the choice of structure function. The asymmetry in the rapidity distribution is defined as [1]

$$\begin{aligned}
 A_{W^+}(+y) &= A_{W^-}(-y) \\
 &= \frac{\sigma_{W^+}(y) - \sigma_{W^+}(-y)}{\sigma_{W^+}(y) + \sigma_{W^+}(-y)}.
 \end{aligned}
 \tag{1.8}$$

The asymmetry of the rapidity distribution for W^+ production at the Tevatron is shown in figure 1.6 [2].

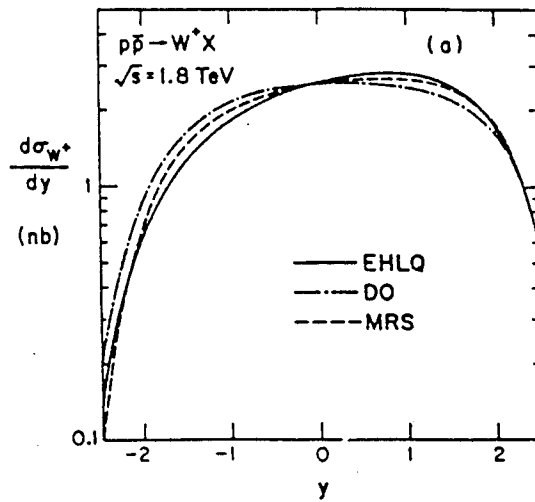


Figure 1.5: Rapidity distribution of W^+ production at Tevatron

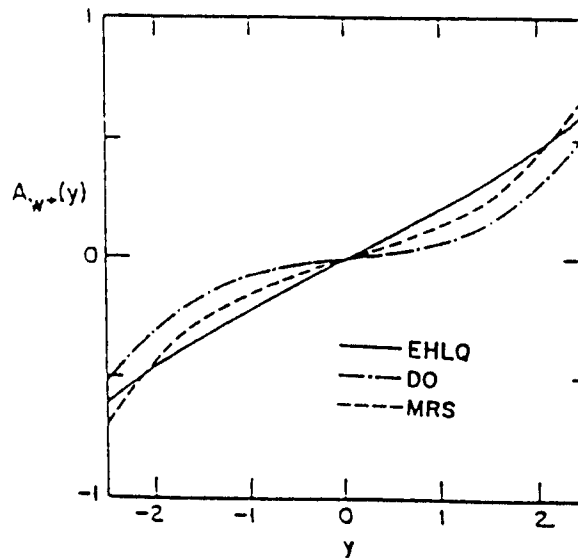


Figure 1.6: Asymmetry of the rapidity distribution for W^+ production at Tevatron

1.3.3 Kinematics

When the parton probability distributions of equation 1.3 are summed over, the inclusive cross section in equation 1.8 can be written as:

$$\begin{aligned} \sigma(p\bar{p} \rightarrow W + X) &= \frac{2\pi G_F}{3\sqrt{2}} x_1 x_2 * \\ &([u(x_1)\bar{d}(x_2) + \bar{d}(x_1)u(x_2)] \cos^2 \theta_C \\ &+ [u(x_1)\bar{s}(x_2) + \bar{s}(x_1)u(x_2)] \sin^2 \theta_C). \end{aligned} \quad (1.9)$$

where the charm quark and heavier quark contributions have been ignored and θ_C is the Cabibbo angle. The u, d, s ($\bar{u}, \bar{d}, \bar{s}$) are the quark and (antiquark) parton probability distributions and x_1, x_2 are the fraction of proton momentum carried by the quarks (antiquarks).

The parton momentum fractions are required by kinematics to satisfy

$$\begin{aligned} x_1 x_2 &= \frac{M_W^2}{s} \\ x_1 - x_2 &= X_W. \end{aligned} \quad (1.10)$$

M_W is the mass of the W , $\sqrt{s} = 2E$ where E is the energy of the proton (antiproton) beam and X_W is the momentum fraction of the W . When these equations are combined with the definition of the rapidity variable, the solutions to the parton fractional momenta are given as

$$\begin{aligned} x_1 &= \frac{M_W}{\sqrt{s}} \exp^{+y} \\ x_2 &= \frac{M_W}{\sqrt{s}} \exp^{-y}. \end{aligned} \quad (1.11)$$

Substituting the values of $M_W = 80$ GeV and $\sqrt{s} = 1800$ GeV into equations 1.11 leads to a solution for x .

Insight into the definition of the asymmetry given y can be obtained by inserting equation 1.9 into equation 1.8 and then rearranging.

$$A_{W^+}(y) \approx \frac{u_1(y)d_2(-y) - d_1(y)u_2(-y)}{u_1(y)d_2(-y) + d_1(y)u_2(-y) + 2s_1(y)s_2(-y)} \quad (1.12)$$

Equation 1.12 shows how the asymmetry of the W is related to the parton probability distributions. (Figure 1.2 shows the $xu(x)$ and $xd(x)$ quark probability distributions for the EHLQ1 structure functions.

1.4 $W \rightarrow \mu\nu$ Decay

What we measure in the laboratory is the W decay lepton. This decay is determined by the $(V - A)$ coupling of the charged weak current. Since the W is produced polarized in the direction of the antiproton beam, helicity conservation demands a preferred direction for the lepton. As shown in figure 1.7, positively charged leptons are preferentially emitted in the anti-proton direction while negatively charged leptons are preferentially emitted in the proton direction. The leptons are distributed according to

$$\frac{dN}{d \cos \theta^*} = \left(1 + \frac{q}{|q|} \cos \theta^*\right)^2 \quad (1.13)$$

where q is the charge of the lepton and θ^* is the angle of the lepton with respect to the anti-proton direction in the W rest frame.

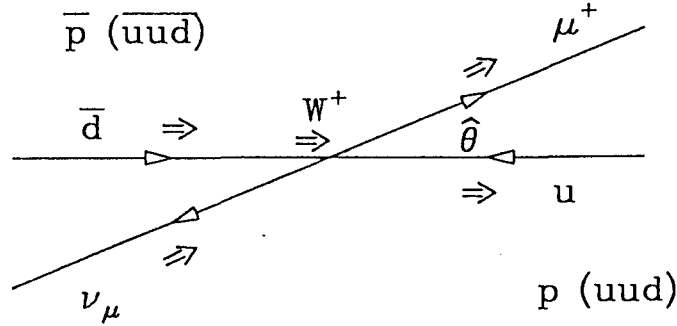


Figure 1.7: Schematic representation of $W \rightarrow \mu\nu$

A small fraction of W 's will be produced by sea quarks. For these events, the W is equally likely to be polarized in the proton or antiproton direction [13]. These events will dilute the decay charge asymmetry.

What is measured in the laboratory is the lepton charge and momentum and the transverse momentum of the neutrino, the latter which is inferred from the calorimetry. Since the longitudinal momentum of the neutrino is not observed, the rapidity of the W cannot be directly reconstructed. If the mass of the W is imposed on the lepton-neutrino system, two solutions to the longitudinal neutrino motion can be determined. These are given as

$$P_z^\nu = \frac{P_z^\mu (M_W^2 + 2P_t^\mu P_t^\nu \cos \phi)}{2(P_t^\mu)^2} \pm \frac{P_t^\mu \sqrt{(M_W^2 + 2P_t^\mu P_t^\nu \cos \phi)^2 - 4(P_t^\mu P_t^\nu)^2}}{2(P_t^\mu)^2} \quad (1.14)$$

where μ denotes the muon, ν denotes the neutrino, M_W is the mass of the W particle and ϕ is the angle between the μ and ν transverse momentum vectors in the lab frame.

At the energies available at the SPS $p\bar{p}$ collider at CERN, the W rapidity distribution was sufficiently narrow such that one of the solutions to the neutrino longitudinal motion was kinematically prohibited. By choosing the lowest momentum solution, they were correct for about 76% of their events [14]. At Tevatron energies, however, the W rapidity distribution is rather broad and the technique used for the SPS energies does not work in the central rapidity region. From Monte-Carlo studies, it was determined that guessing the lower P_z^ν solution would give the correct W rapidity for about 52% of the events in the central region of $|\eta| < 1.0$ and $P_t > 20\text{GeV}/c$. In the forward region, however the SPS method selects the correct solution for about 85% of the events in the region of $2.0 < |\eta| < 2.4$ and $P_t > 22\text{GeV}/c$. Therefore, not only are we able to measure the lepton asymmetry in the forward region, but we can also measure the W asymmetry.

Since the effect of the W rapidity distribution on the final state charged lepton rapidity is known to be a simple sum of the W rapidity plus the lepton rapidity in the W center of mass system, the lepton asymmetry can be used to measure the effect of different parton structure functions. It is useful to use the pseudorapidity variable when referring to the lepton since $y = \eta$ when $E \gg m$ where E is the energy of the particle and m is the particle mass. Since the leptons from W decays have large momentum compared to the lepton mass, the $E \gg m$ condition is

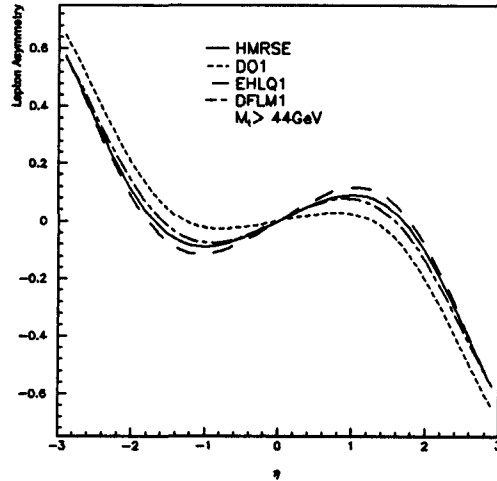


Figure 1.8: Lepton Asymmetry as a function of Lepton Rapidity

true. The pseudorapidity variable is defined as

$$\eta = -\ln\left[\tan\left(\frac{\theta}{2}\right)\right] \quad (1.15)$$

The lepton asymmetry is given by

$$A_l(\eta) = \frac{N^+(\eta) - N^-(\eta)}{N^+(\eta) + N^-(\eta)} \quad (1.16)$$

where $N^+(\eta)$ is the number of events with charge times pseudorapidity > 0 and $N^-(\eta)$ is the number of events with charge times pseudorapidity < 0 . Figure 1.8 shows the lepton asymmetry as a function of pseudorapidity. As noted in Figure 1.8, different choices of structure functions predict different lepton asymmetries. The (V-A) decay asymmetry, A_l is opposite to the W asymmetry, A_W where the latter is due to differences in the $u(x)$ and $d(x)$ distributions. By using

different M_t (or similarly P_t) cuts, the asymmetry due to the structure functions can be enhanced over the V-A decay asymmetry. This is because as the $M_t \rightarrow 80\text{GeV}/c^2$, the angle of the muon with respect to the anti-proton direction in the W rest frame approaches 90° where the decay asymmetry is zero. For higher M_t bins, the asymmetry due to the structure functions is larger than the decay asymmetry. Figure 1.9 shows how the lepton asymmetry as a function of pseudorapidity changes for different M_t bins.

1.5 Asymmetry Effects Due to Higher Order Corrections

The corrections to the Drell-Yan model of the lepton pair production come from the emission of real gluons, figure 1.10, and from Compton graphs, figure 1.11, [15].

The first order contribution to the inclusive rapidity distribution for the production of a W^+ can be expressed as [2]

$$\frac{d\sigma}{dy}(\text{DY} + \text{Higher Order Corrections}) = K(y) \frac{d\sigma}{dy}(\text{DY}) \quad (1.17)$$

where $K(y)$ is the factor associated with higher order contributions in QCD and is defined as

$$K(y) = \frac{\sigma_{DY}(y) + \sigma_R(y) + \sigma_V(y) + \sigma_C(y)}{\sigma_{DY}(y)} \quad (1.18)$$

where σ_{DY} is the cross section for the lowest order Drell-Yan process, σ_R the

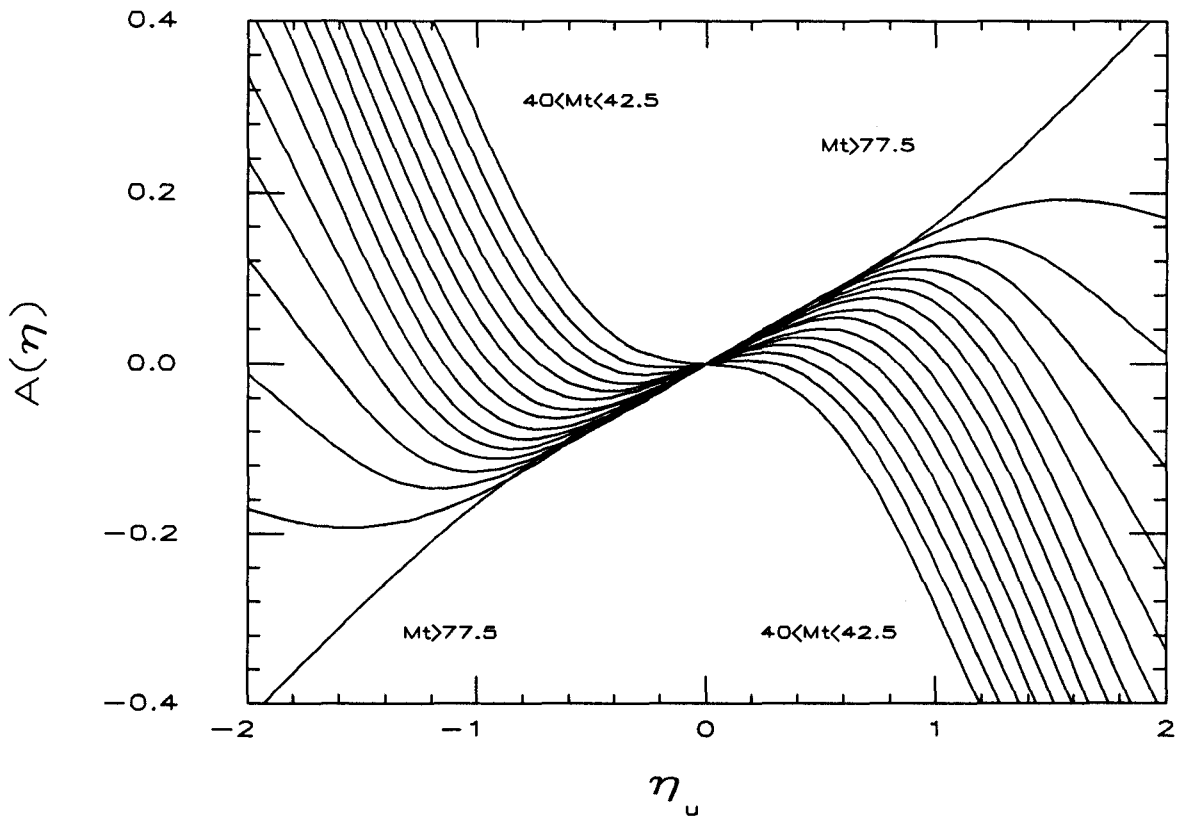


Figure 1.9: Lepton Asymmetry as a function of Lepton Rapidity for different M_t cuts. Each contour represents a M_t bin of 2.5GeV.

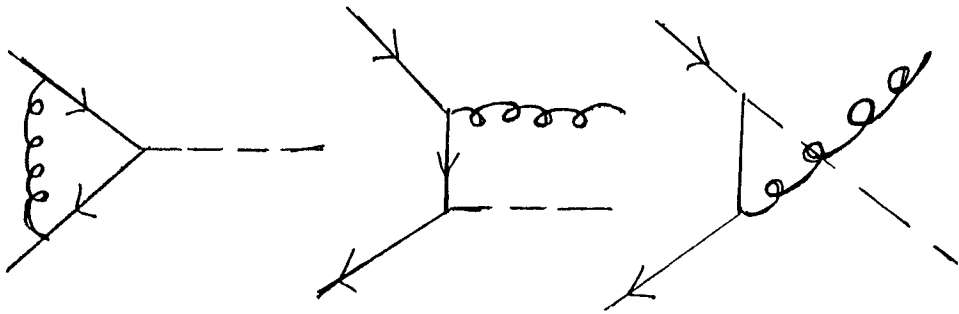


Figure 1.10: Annihilation graphs

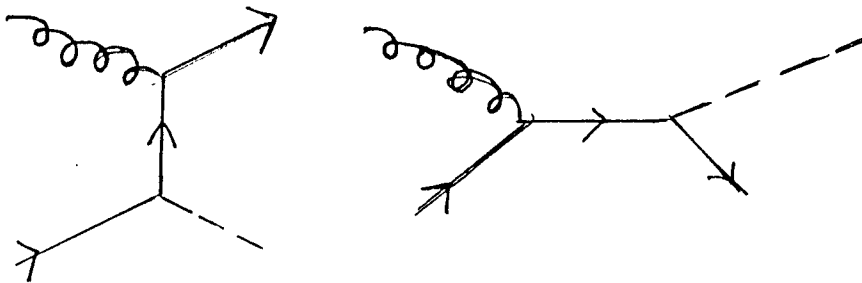


Figure 1.11: Compton graphs

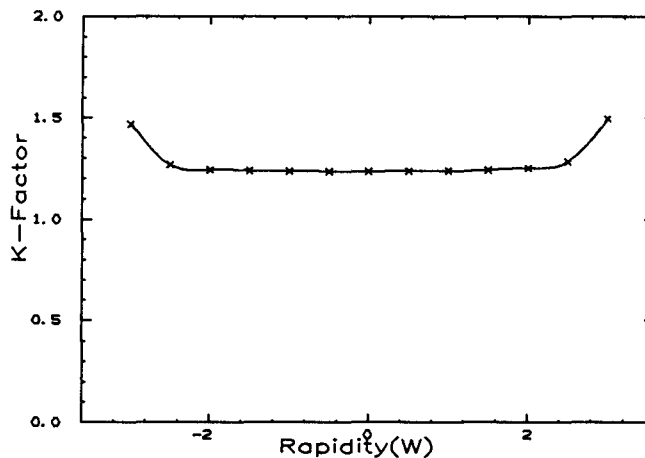


Figure 1.12: K-factor vs W Rapidity

Drell-Yan cross section with the radiation of a real gluon, σ_V the Drell-Yan cross section with the vertex correction and σ_C is the Compton term.

$K(y)$ is basically independent of rapidity over the range $0 < |y| < 2.5$ as shown in figure 1.12 [16]. The W asymmetry is thus mostly determined by the $d\sigma_{DY}/dy$ distribution (Figures 1.5 and 1.6). For that reason, we do not expect the higher order terms to have much affect on the W asymmetry.

However, we measure the lepton rapidity (which is just a sum of the W rapidity and the rapidity of the lepton in the W center-of-mass system). The presence of higher order diagrams can give the W transverse motion which will affect the measured lepton asymmetry. Transverse motion of the W tends to deflect the initial W polarization away from the beam direction thus washing out

the lepton decay asymmetry [13].

Chapter 2

Apparatus

2.1 The Tevatron Collider

The Tevatron Collider located at Fermi National Accelerator Laboratories is the world's highest energy proton-antiproton collider. Figure 2.1 shows an overhead view of the Fermilab accelerator complex.

The proton beam is created when H^- ions are injected into a linear accelerator called the LINAC. The LINAC accelerates the ions to approximately 500 MeV and then injects them into the booster. In the booster, the electrons are stripped off and the bare protons are accelerated to 8 GeV and then injected into the main-ring.

The main ring is a 400 GeV proton synchrotron constructed out of conventional magnets with a radius of 1000 meters. The synchrotron was initially used for fixed target high energy experiments, but is now used as an injector to the

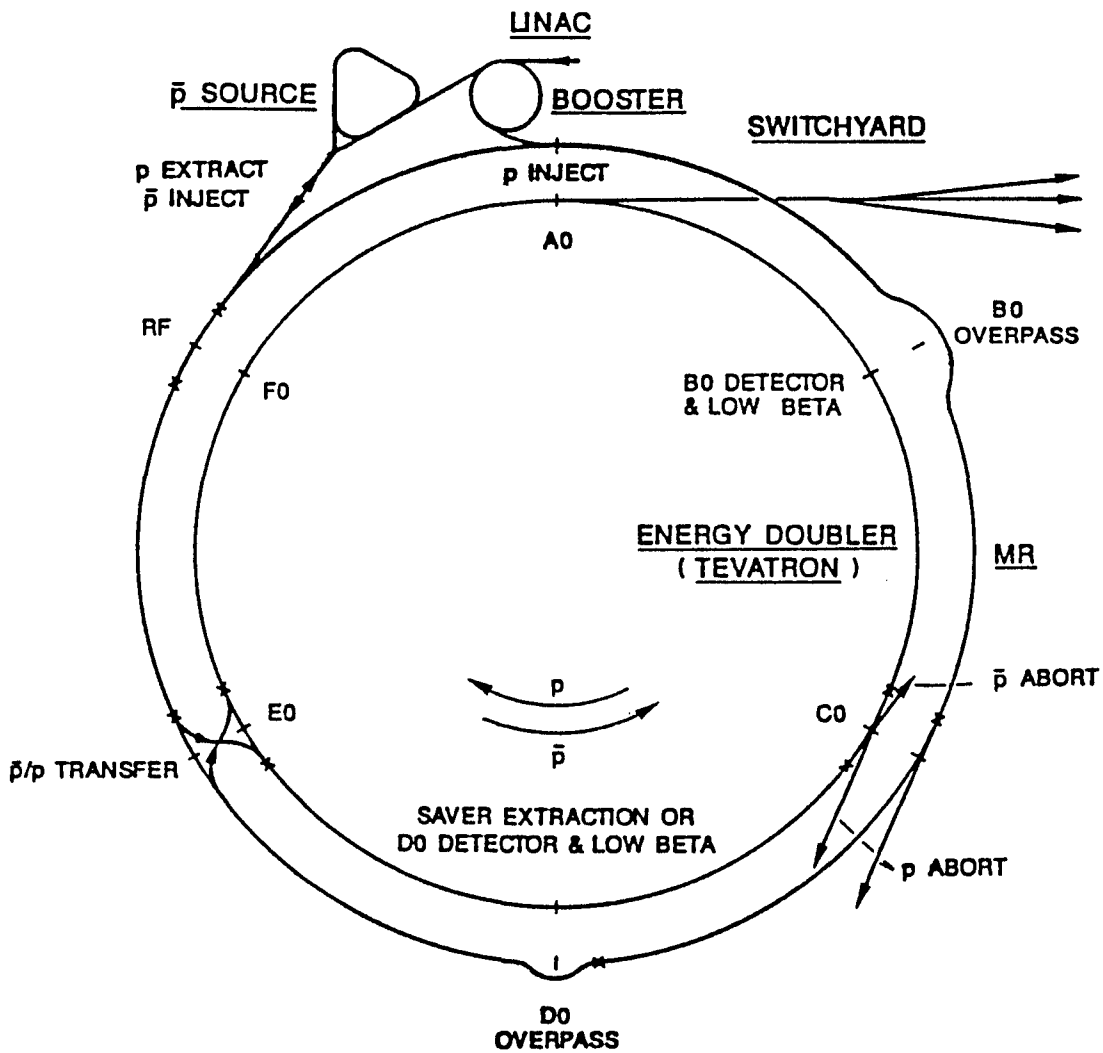


Figure 2.1: An Overhead View of the Fermilab Accelerator Complex

Tevatron and for the production of antiprotons. The Tevatron ring consists of superconducting magnets which are located in the same ring as the main ring. With the superconducting magnets, particles are accelerated to 900 GeV.

Antiprotons of $8 \pm \Delta E$ GeV are produced when 120 GeV protons from the main ring strike a tungsten target. The antiprotons are then focused by a lithium lens and are steered into the debuncher. The main purpose of the debuncher is to reduce the energy spread of the bunches to match the acceptance required by the accumulator. This is done by increasing the time spread of the bunches using radio frequency bunch rotation. A process called stochastic cooling is also used in the debuncher to reduce the transverse motion of the beam. After two seconds in the debuncher, the antiprotons are injected into the accumulator where further stochastic cooling is performed. The antiproton accumulator operation, also called stacking, continues until a sufficient number of antiprotons have been collected ($\approx 10^{10}$ /hour for about 24 hours).

To achieve colliding beams, 6 bunches of protons are extracted from the booster and injected into the main ring. The bunches are accelerated to 120 GeV after which the main ring is radio frequency phase locked to the Tevatron and the protons are transferred to the Tevatron. A similar process is performed on the antiprotons by extracting them from the accumulator and injecting them into the main ring.

Once the antiprotons have been transferred to the Tevatron, further radio frequency adjustments are made to the $p\bar{p}$ beam so one of the twelve crossing

points occurs inside the CDF detector. The particles are then accelerated to 900 GeV together in the same tunnel. Since the charge of the antiproton is opposite the charge of the proton, the antiprotons travel in the opposite direction from the proton. Once the particles have been accelerated, special focussing low-beta quadrupole magnets located on both sides of the CDF interaction point are used to focus the beam at the crossing point located inside the CDF detector region. The squeezing of the beam increases the initial luminosity by decreasing the beam width profile at the CDF interaction point. The luminosity is given by

$$L = \frac{N_p N_{\bar{p}} C}{4\pi\sigma^2}. \quad (2.1)$$

where N_p and $N_{\bar{p}}$ are the numbers of protons and antiprotons per bunch. C is the bunch crossing rate and σ^2 is the RMS beam width profile in the horizontal and vertical direction. The luminosity degrades with time due to decreasing N_p and $N_{\bar{p}}$ as well as an increasing σ^2 . Typical beam lifetimes during the 1988-89 CDF run were on the order of 12 hours.

2.2 The CDF Detector

The Collider Detector at Fermilab (CDF) is a 5000 ton multi purpose magnetic detector built to study the particles produced in $p\bar{p}$ collisions. Figure 2.2 shows a perspective view of the CDF detector and figure 2.3 shows a side view of the detector. The CDF coordinate system defines the positive z axis along the direction traveled by the protons (from the west going towards the east). The

y-axis is vertically upward and the x axis is radially outward from the center of the tevatron ring with the positive axis pointing north. With these definitions, θ and ϕ are defined with the usual conventions. This thesis is primarily concerned with muon detection. The parts of the CDF detector required for muon detection and analysis will be discussed in the remainder of this chapter.

2.2.1 The CDF Tracking Chambers

2.2.1.1 The Vertex Time Projection Chambers

The Vertex Time Projection Chambers (VTPC) consisted of eight octagonal modules covering 2.8 meters surrounding the interaction region. A picture of the VTPC is shown in figure 2.4. These chambers were closest to the beam and were embedded in the superconducting solenoidal 1.5 Tesla field. The VTPC chambers measured the event vertex position in the Z direction using the R-Z track coordinates of primary particles produced in $p\bar{p}$ collisions. The variable Z is defined as the distance along the beam line from the center of the detector and the variable R is defined as the radial distance from the beam.

Each VTPC module had a central high voltage grid that divided it into two drift regions. Electrons drifted in a 50/50 mixture of argon-ethane away from the center grid until they passed through a cathode grid and entered one of the two proportional chamber endcaps in which were located sense wires and cathode pads. The arrival time of the electrons at the sense wires gave a picture of the event in the R-Z plane. Adjacent modules were rotated relative to each other

Figure 2.2: Perspective View of the CDF Detector

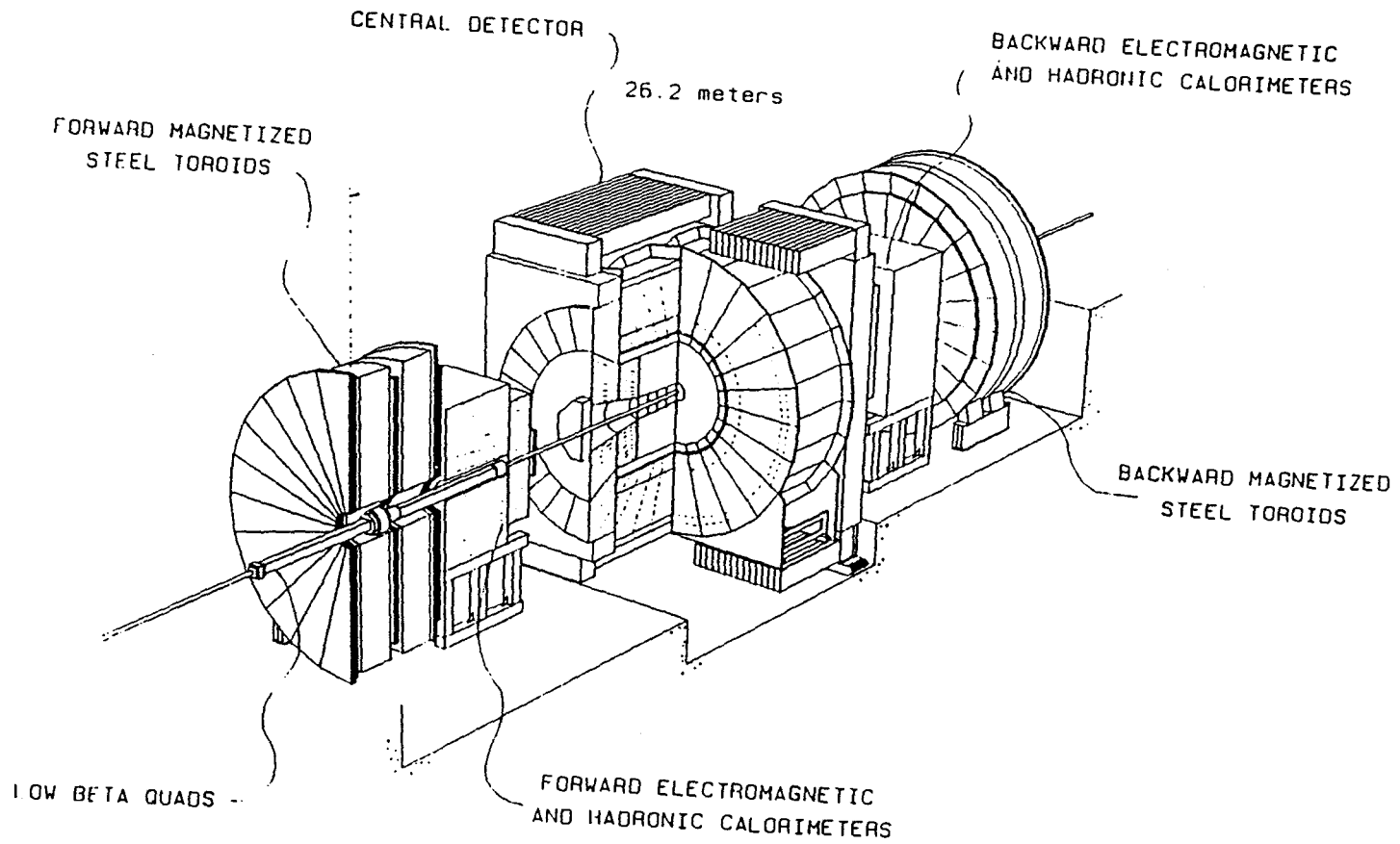
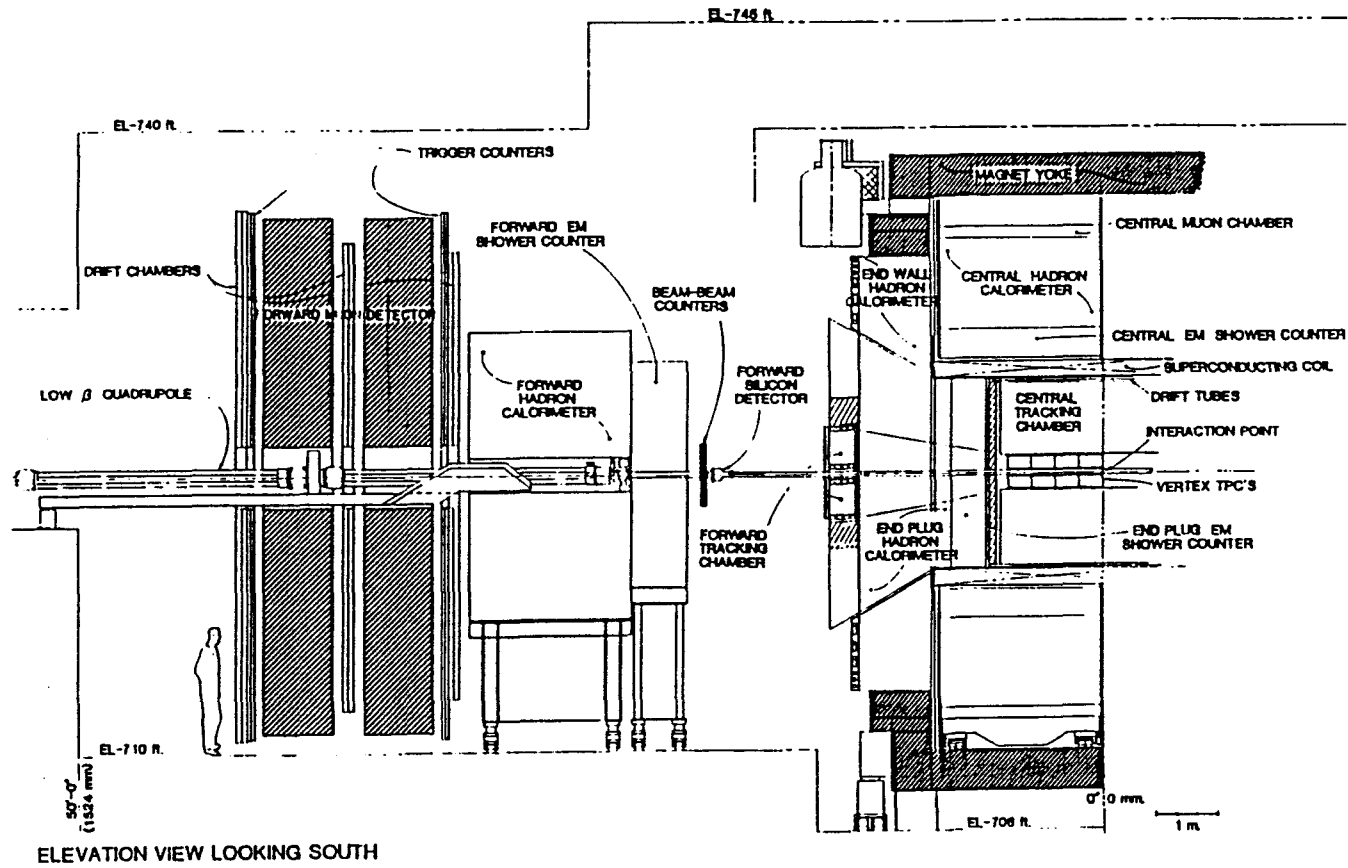


Figure 2.3: Side View of the CDF Detector



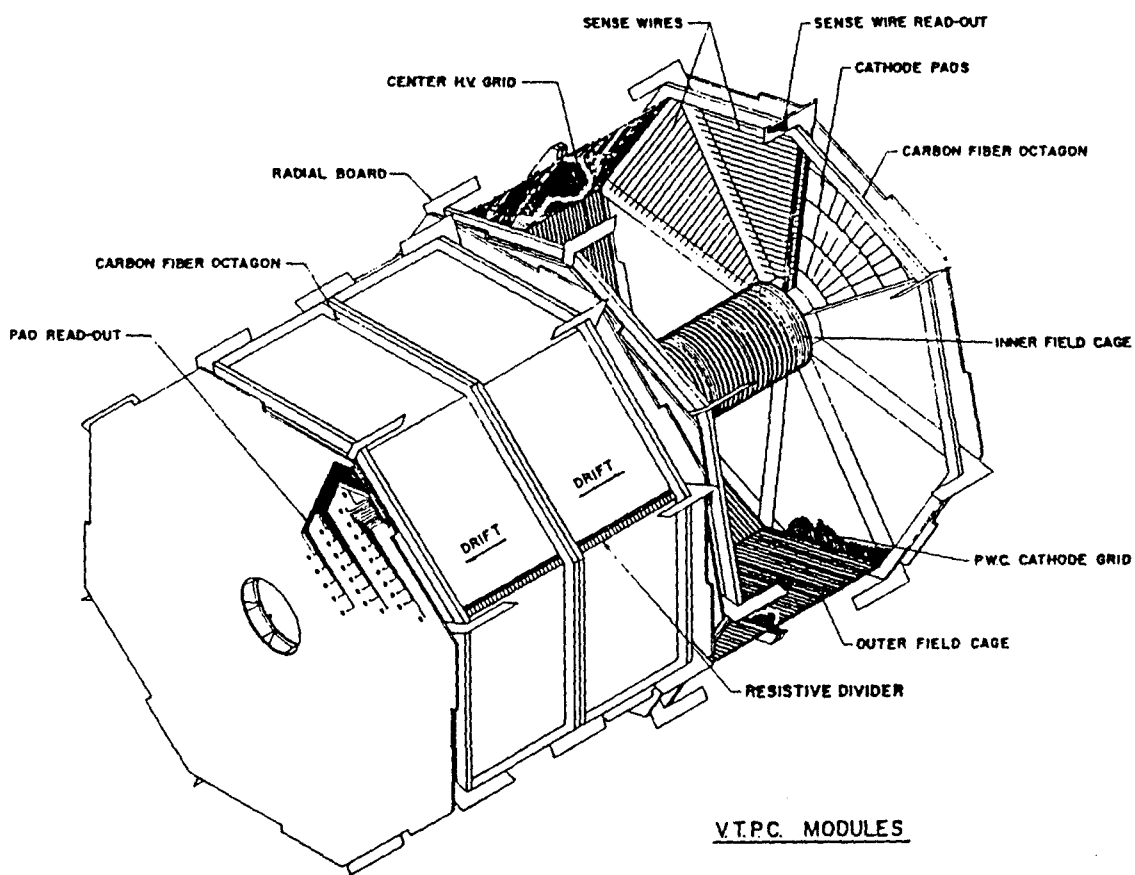


Figure 2.4: Two of the eight vertex time projection chambers modules

by 11.3° in ϕ to eliminate inefficiencies near octant boundaries and to provide ϕ information for small angle stereo.

The VTPC system determined event topologies over the range of polar angles $3.5^\circ < \theta < 176.5^\circ$ and could identify multiple interactions in the same beam crossing. At the average 1988-89 CDF run luminosities of $10^{30} \text{ cm}^{-2} \text{ s}^{-1}$, one in five events contained two interactions.

The Z resolution of the VTPC was a function of the polar angle θ . For tracks with $\theta = 90^\circ$, the Z resolution was found to be $420 \mu\text{m}$ rising to $1100 \mu\text{m}$ for tracks with $\theta = 11^\circ$ [17].

2.2.1.2 The Central Tracking Chambers

The Central Tracking Chambers (CTC) surrounded the VTPC and were also embedded in the solenoidal magnetic field. The CTC occupied a volume over 5 meters long and 3 meters in diameter and was designed to measure the track parameters of charged particles in the R- ϕ plane. Figure 2.5 shows the R- ϕ view of the CTC.

The CTC was a wire chamber with 84 layers of sense wires arranged into 9 superlayers. Each of the five axial superlayers contained 12 sense wire layers and provided R- ϕ information. The remaining four stereo superlayers contained 6 sense wires and were tilted by $\pm 3^\circ$ with respect to the beamline. The stereo superlayers were interwoven between the axial superlayers and provided the R-Z information. Both axial and stereo superlayers are divided into cells which were

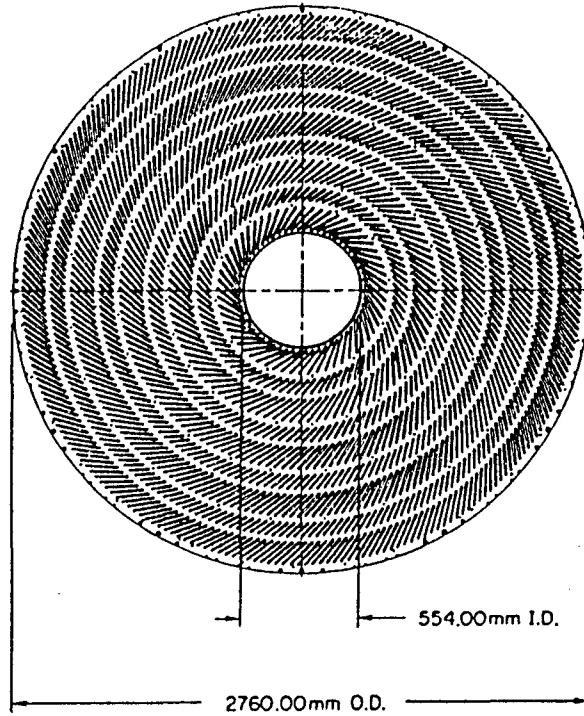


Figure 2.5: R- ϕ view of the CTC.

tilted by 45° with respect to the radius vector to determine an azimuthal drift direction as well as to resolve tracking ambiguities.

For tracks with $p_t > 1$ GeV, the axial superlayers measured the azimuthal R- ϕ position in each layer to better than $200 \mu\text{m}$. The stereo layers measured the R-Z position with a resolution of 6 mm. The RMS momentum resolution of the CTC was given by $\Delta P_t/P_t = .0020 P_t \text{ GeV}/c$ for isolated tracks in the region of $40^\circ < \theta < 140^\circ$ and where P_t was in units of GeV/c. If the additional constraint that the track was required to pass through the nominal R- ϕ beam position was used, the resolution was improved to $\Delta P_t/P_t = .0011 P_t \text{ GeV}/c$.

Tracks with $\theta < 40^\circ$ or $\theta > 140^\circ$ did not pass through all the superlayers of the CTC and the momentum measurement was degraded. Algorithms were devised to extend the track fitting abilities to smaller angles with some success.

However, the limiting angles fell short of the forward muon detector regions.

2.2.2 Calorimeters

Located outside of the solenoidal magnet were the CDF sampling electromagnetic and hadronic calorimeters. These calorimeters, which were mechanically divided into three η regions, covered the full η range of ± 4.2 and the full azimuthal range. η was the pseudorapidity variable defined in Equation 1.15 of chapter 1. All of the calorimeters were designed with projective towers such that they pointed at the nominal interaction region. The central calorimeter towers (region 1, $|\eta| < 1.1$) were .1 units of η wide by 15° in ϕ , the plug calorimeter towers (region 2, $1.1 < |\eta| < 2.4$) and the forward calorimeter towers (region 3, $2.4 < |\eta| < 4.2$) were .1 units of η wide by 5° in ϕ .

The calorimeters at CDF were of two types. In the central region, scintillator calorimeters were used for good resolution. In the plug and forward regions, gas calorimeters were used because of higher multiplicities. Gas calorimeters also allowed easy segmentation into smaller sized towers which was demanded if a constant unit of rapidity was to be maintained.

2.2.2.1 Gas Calorimeters

Both the electromagnetic and hadronic calorimeters in the plug and forward region used a 50/50 mixture of argon-ethane gas for the calorimeter sampling medium. A small percentage of alcohol was also added to the gas to prevent glow

discharge. The gas gain for each of these calorimeters was initially measured in a test beam. Calibration of each system was maintained during the 1988-89 CDF run using Fe55 sources.

2.2.2.2 Endplug Electromagnetic Calorimeter

The endplug electromagnetic calorimeter (PEM) used a sampling medium that consisted of 34 layers of gas filled proportional tubes interspersed with a lead absorber with a total of 16 radiation lengths. The PEM system consisted of two cylindrical modules, east and west. The modules were located at ± 173 cm from the nominal beam interaction. Each module was symmetrically divided into 4 quadrants, each of which occupied a single gas volume. Each layer of the gas was sampled by approximately 156 proportional tubes epoxied to sheets of etched copper clad panels. The cathode pads were ganged to form projective towers with three depth segments containing 5, 24 and 5 layers which provided information about longitudinal electron shower development. The calorimeter resolution was found to be

$$\frac{\sigma(E)}{E} = \frac{28\%}{\sqrt{E}} + 2\% \quad (2.2)$$

2.2.2.3 Endplug Hadron Calorimeter

The endplug hadronic calorimeter PHA used a sampling medium that consisted of 20 layers of gas filled proportional tubes interspersed with a steel absorber with an interaction length of $6.3/\cos \theta$. The PHA calorimeter was located directly

behind the PEM calorimeter maintained the same tower structure. As in the PEM, the cathode pads were ganged to form projective towers. The calorimeter resolution was found to be

$$\frac{\sigma(E)}{E} = \frac{86\%}{\sqrt{E}} + 4\% \quad (2.3)$$

2.2.2.4 Forward Electromagnetic Calorimeter

The forward electromagnetic calorimeter (FEM) consisted of 30 sampling layers of proportional tube chambers separated by lead sheet absorbers with a total of 25.5 radiations lengths. Two calorimeter modules located at ± 650 cm from the nominal beam interaction comprised the FEM system. The proportion tube chambers were constructed with cathode pads which were ganged longitudinally into towers with 2 depth segments to provide information on shower development. The anode wires were ganged together in five groups per quadrant layer and used primarily for diagnostic purposes, but also provided some longitudinal profile information. The FEM detector resolution was found to be

$$\frac{\sigma(E)}{E} = \frac{25\%}{\sqrt{E}} + .5\% \quad (2.4)$$

2.2.2.5 Forward Hadron Calorimeter

The forward hadronic calorimeter (FHA) consisted of 27 layers of proportional tube chambers separated by a steel absorber with a total interaction length of $8/\cos\theta$. The FHA was located directly behind the FEM and maintained the

same tower structure. Each of the FHA calorimeter modules was divided into 4 quadrants that consisted of proportional tube chambers with cathode pad read-out. The cathode pads were ganged longitudinally in projective towers with no depth segmentation. Each anode plane was divided into 6 regions and read out to give additional information on longitudinal shower development. The FHA calorimeter resolution was found to be

$$\frac{\sigma(E)}{E} = \frac{140\%}{\sqrt{E}} \quad (2.5)$$

2.2.3 The CDF Level0 Trigger - Beam Beam Counters

A four-level combined hardware and software trigger system was used during the 1988-89 CDF run. All triggers were gated on the beam-beam crossing, which occurred every $3.5 \mu\text{sec}$. The lowest level of the CDF trigger, called Level0, used the beam beam counters (BBC) to select inelastic collisions. Level0 inhibited the next crossing to wait for detector signals at Level1. If the thresholds set at Level1 were satisfied, more complex pattern requirements could be made at Level2. Finally, Level3 was a software trigger, and for the Forward Muon triggers running the same code as the offline analysis.

The beam beam counters consisted of two scintillator hodoscopes located on the front face of each forward electromagnetic calorimeter. Each BBC consisted of two planes of 16 scintillator counters, arranged in a criss-cross grid centered on the beam as shown in Figure 2.6. Four beam beam counters were used in each quadrant. A coincidence between counters on one side of the interaction

region (East,West) with the counters on the other side (West,East), within a 15 ns gate centered on 20 ns after the beam crossing constituted a East-West Level0 trigger. The cross section for this process was measured to be $\sigma(\text{beam-beam counters})=(44\pm 3)\text{mb}$ [18].

The Level0 trigger was also used as a minimum bias trigger. For this thesis, muon triggers were required in conjunction with the Level0 trigger. The muon trigger levels will be discussed in later sections.

2.3 The Forward Muon (FMU) System

2.3.1 The FMU Apparatus

The CDF forward-backward muon system consisted of two spectrometers which measured muon position and momentum over the angular regions $3^\circ < \theta < 16^\circ$ and $164^\circ < \theta < 177^\circ$. Each spectrometer consisted of two toroidal magnets with three planes of electrodeless drift chambers and two planes of scintillator counters. Each successive plane had a larger radius to maintain the solid angular acceptance. Each plane of chambers or counters was divided into 24 15° wedge shaped components to cover the full azimuthal range. The drift chambers were supported by a "spider-web" type structure which was hung from the top of the toroids and the counters were supported by mounts welded to the face of the magnets [19] [20].

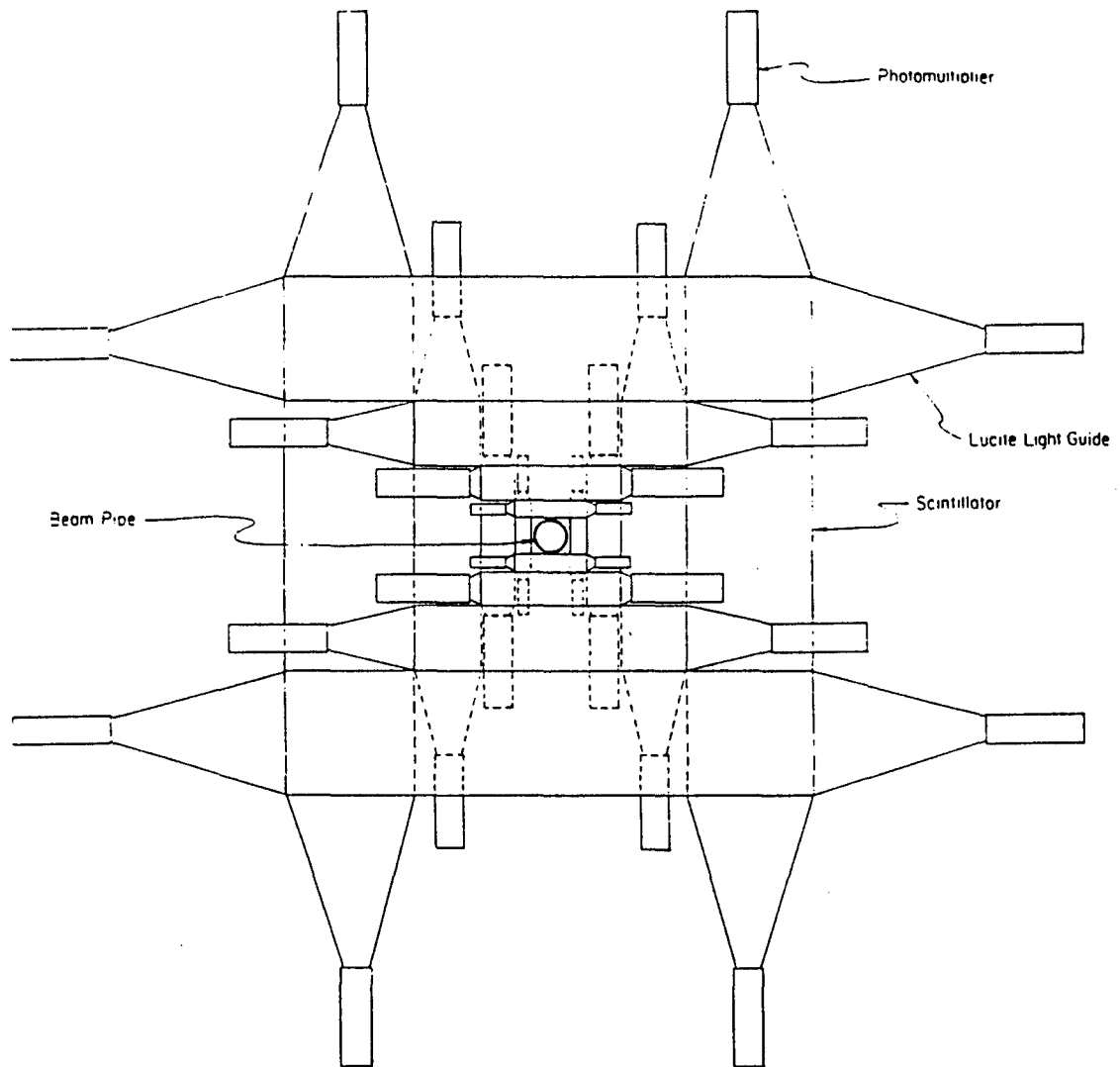


Figure 2.6: A beam's-eye view of one of the beam-beam counter planes.

2.3.2 The FMU Toroids

Two 395 ton cast steel toroidal magnets each with dimensions 7.6 m o.d. x 1.0 m i.d. x 1.0m thick were located in each of the forward and backward detector regions. Each toroid had four rectangular coils consisting of 28 turns of copper conductor to provide an azimuthal field in the steel. The toroids separated at the vertical centerline into halves for mobility purposes. When the toroidal halves were pushed together, they left a 3 mm gap at the top which allowed for magnetic field measurements. A coil current of 1000 Amps produced a field which varied from 2 Tesla at the inner radius to 1.6 Telsa at the outer radius [21]. Differences in the magnetic field variation between the four toroids were at the 5% level.

2.3.3 The FMU Drift Chambers

The drift field in the electrodeless FMU drift chambers was shaped by an equilibrium distribution of charges on the inside insulating chamber walls. The time needed to establish this equilibrium was dependent on the background radiation level. Figure 2.7 shows how the field lines change as the stable charge configuration is established for a chamber cell. Inside the collision hall of CDF, background radiation levels were large enough to establish equilibrium charge distributions within a hour.

Each chamber plane consisted of 24 drift chambers segmented in ϕ into 15° wedges. Each drift chamber consisted of two planes of drift cells (as shown in Figure 2.7) with one plane staggered relative to the other to resolve the left-right

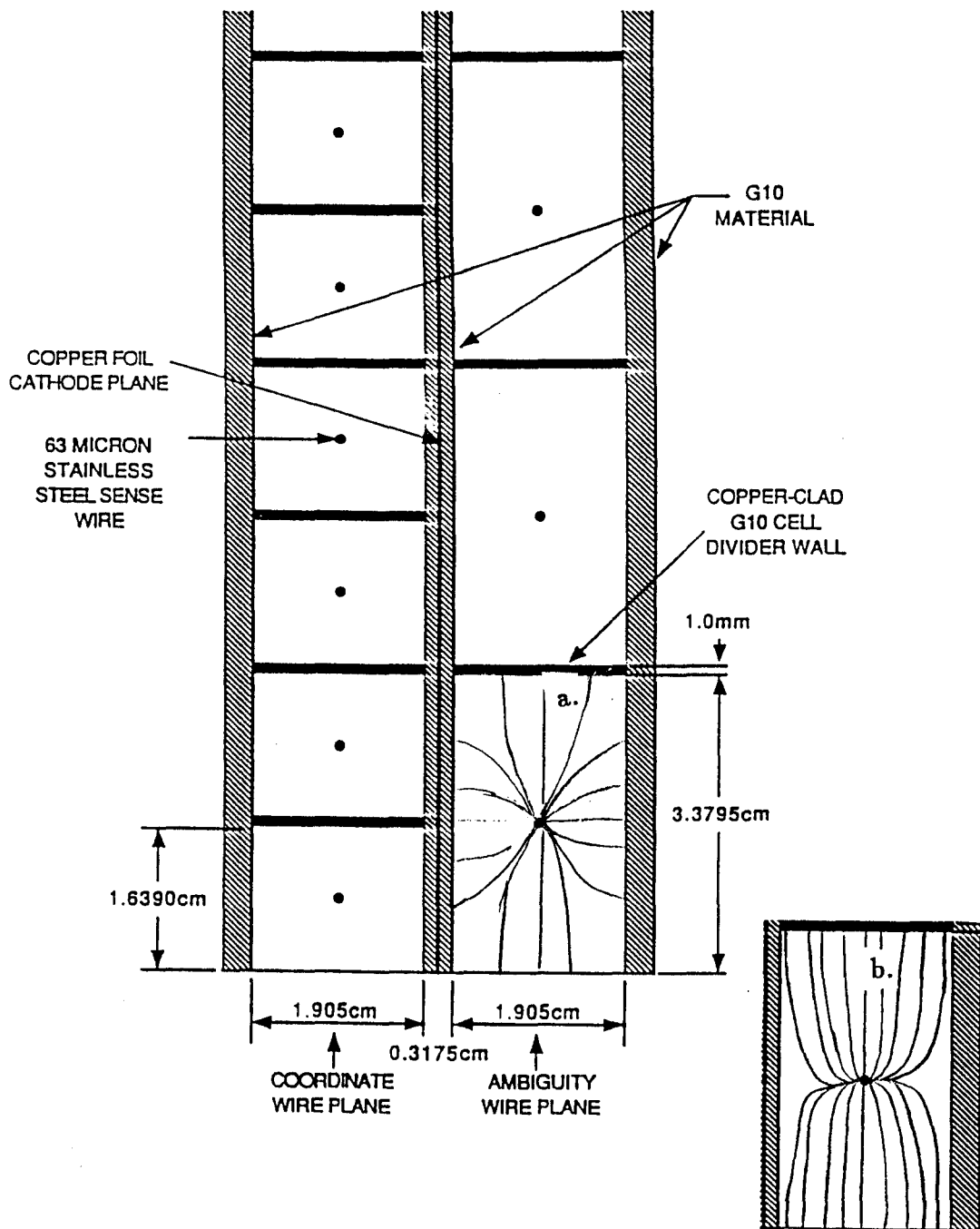


Figure 2.7: FMU Drift Field Configuration. a.) Initial field line configuration.
b.) Equilibrium field line configuration.

ambiguity of the particle track. Each drift chamber itself was staggered relative to its neighbor to eliminate detector dead spots at wedge boundaries. Each drift cell contained an anode wire strung along a chord of the wedge. Figure 2.8 is a schematic showing the components for the forward muon front detector plane. The chamber cell sizes were averaged into groups of 8 yielding 7 different η bins for one plane of cells (referred to as the coordinate plane) and 5 different η bins for the second plane of cells (referred to as the ambiguity plane). A common copper foil cathode plane further divided the chambers into 5° bins in ϕ . The cathode planes were also segmented into .3 units of η .

The drift chambers contained a mixture of 50/50 argon-ethane which produced a constant drift velocity of $5 \text{ cm}/\mu\text{s}$. The voltage on the anode sense wire depended on the chamber cell size. Values between 3 - 6 kV were maintained which led to an overall chamber efficiency of 98% [22]. The sense wires were read out by multihit TDC's. Three sense wires adjacent in ϕ were ganged together to reduce the number of electronic channels. The ϕ segmentation was maintained by both the counters and the cathode pad signals. The cathode pad signals were read out using Rabbit electronics.

The calibrations of the FMU chamber resolution are described elsewhere [22]. A test setup calibration using cosmic ray muons was found to give a position resolution of $450 \mu\text{m}$.

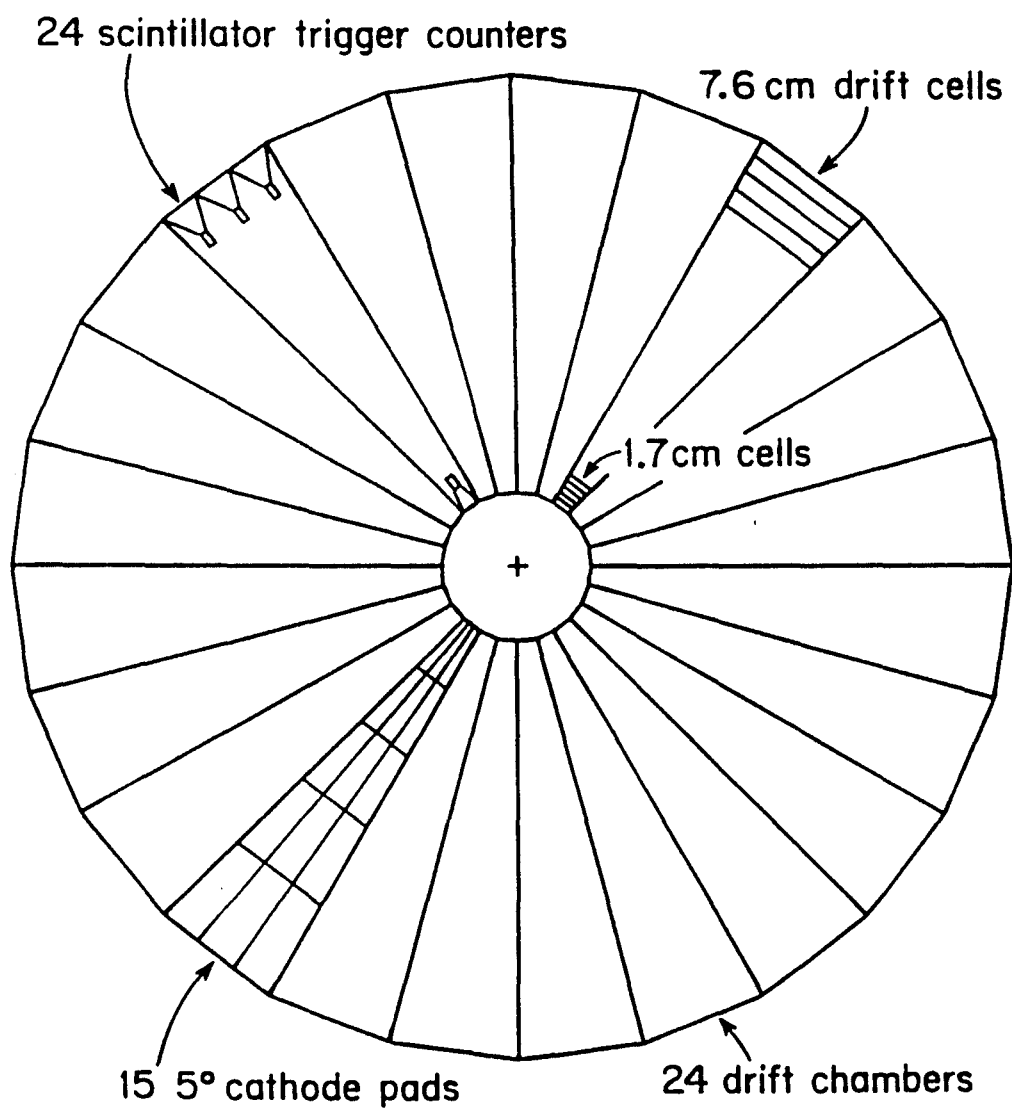


Figure 2.8: The components for the forward muon front detector plane are shown.

2.3.4 The FMU Scintillator Counters

Each plane of the 10 % naphthalene-doped acrylic scintillator was segmented in ϕ into 24 15° wedges. Each wedge was instrumented with light pipes containing a 180° bend and four Amperex 2202B photo-multiplier tubes. Three of the phototubes were located at the outer radius of each scintillator wedge and one single phototube was located at the inner radius of the wedge. A Schmitt-trigger circuit was placed in each phototube base and this circuit provided an ECL logic pulse for each anode pulse exceeding 10 mV. The .OR. of the phototube signals from a wedge was latched for use in the trigger. A light emitting diode pulsing scheme allowed for online calibrations.

A small gap between adjacent scintillator wedges created dead regions in the scintillator ϕ acceptance. The gap distance between each set of scintillator wedges was measured at the outer radii of the wedge. The azimuthal acceptance for the scintillator counters in the east region ($3^\circ < \theta < 16^\circ$) was found to be $96.4 \pm .1$ % while the azimuthal acceptance in the west region ($164^\circ < \theta < 177^\circ$) was found to be $96.9 \pm .1$ %

2.3.5 The FMU Trigger

Figure 2.9 shows a schematic of the forward muon trigger electronics used for the 1988-89 CDF run. (A description of much of the FMU electronics is described elsewhere [23]). The Level1 trigger took advantage of the projective tower structure maintained in the drift cells. A complication of forward muon analyses is

that the trigger configuration changed during the run. Two different Level1 trigger boards were used. Both used custom electronics boards to search projective towers for a coincidence of hits. The main difference between the two triggers was that one was more efficient at selecting real muons, thus reducing the trigger rate.

2.3.5.1 The HOPU Trigger Boards

The first FMU trigger used Half-Octant Pattern Units or HOPU boards and a Scintillator Hodoscope and Muon Pattern Unit or SHAMPU. Each HOPU contained the logic to analyze the wire hit information from a wedge of 45° in ϕ and 9° in θ ($7^\circ < \theta < 16^\circ$) and determined whether a muon had passed one of three P_t thresholds defined by the hit pattern.

The original HOPU trigger, consisting of a coincidence between 3 coordinate wires, yielded an unacceptably large rate. To solve this problem, a temporary DI-HOPU trigger was installed. Two HOPUs were used for each octant wedge with one HOPU searching the coordinate plane wires and the other HOPU searching the ambiguity plane wires. A valid DI-HOPU trigger required a 3-wire coincidence among coordinate hits and also a 3-wire coincidence among ambiguity hits. The two coincidences were not required to be satisfied in the same octant, however. Figure 2.10 shows the allowed hit patterns for the DI-HOPU 100% P_t thresholds used during the 1988-89 run. This trigger corresponded to a coincidence between hits in the n th cell of an octant in each chamber plane.

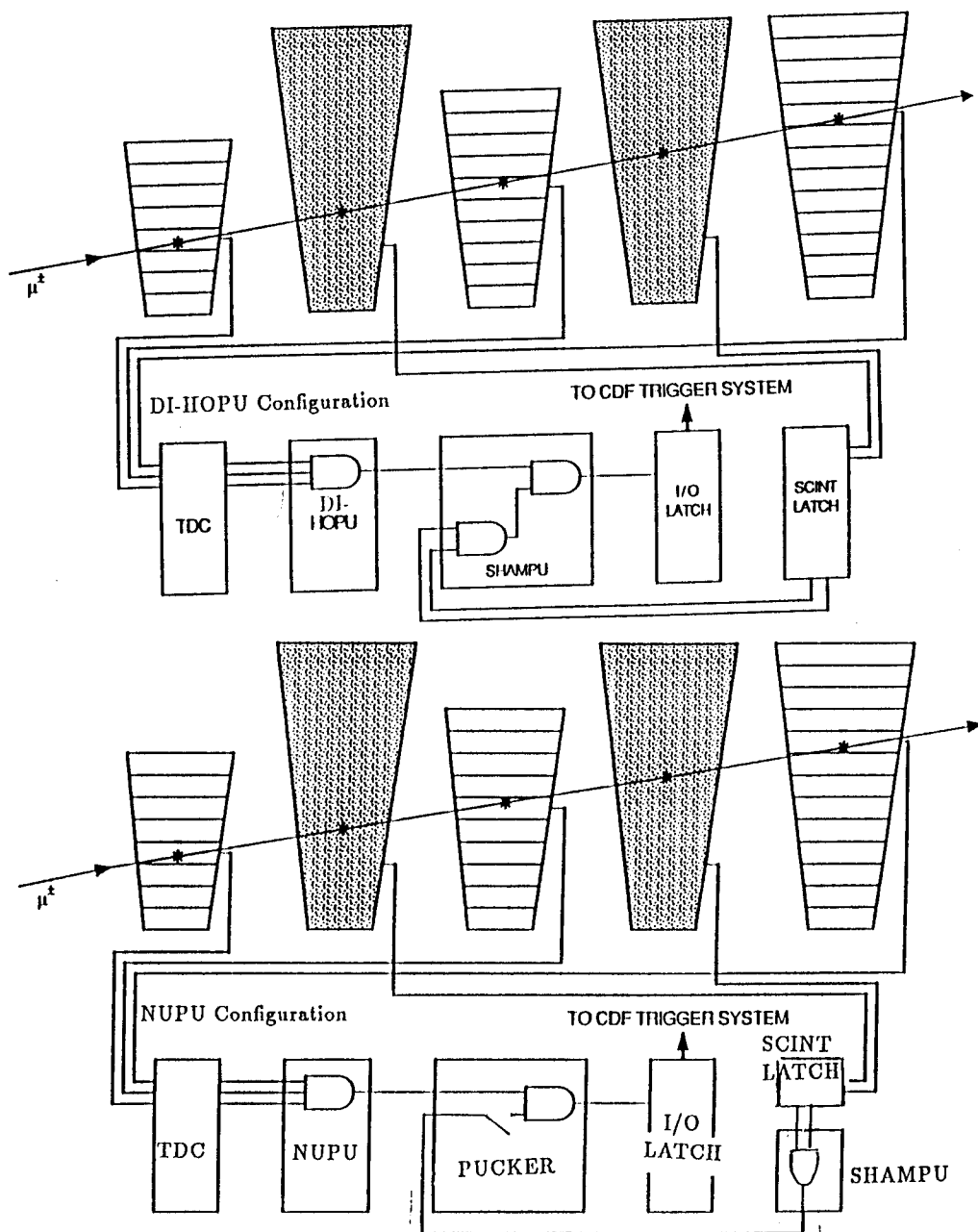
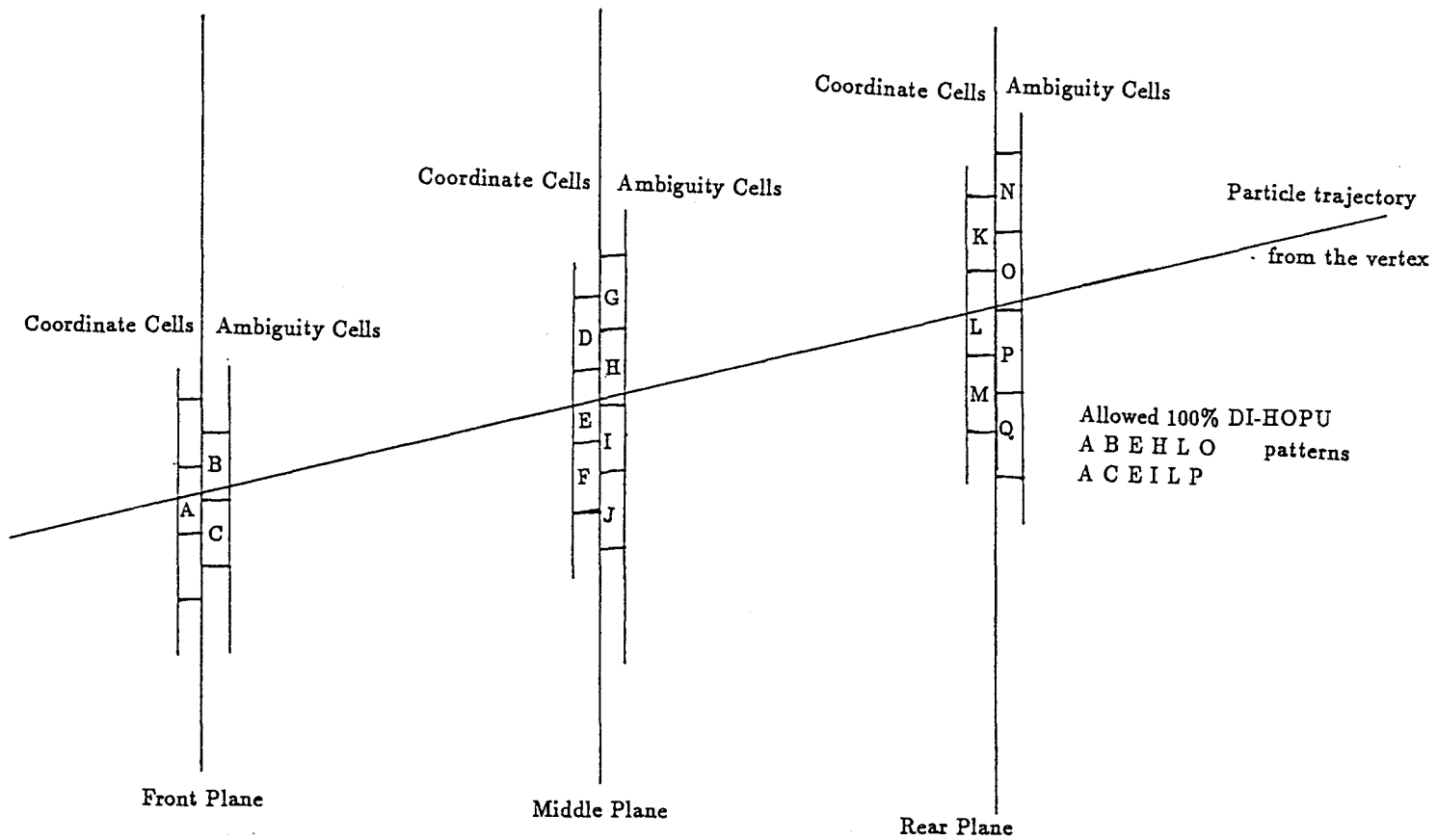


Figure 2.9: Schematic of the forward muon electronics during the 1988-89 CDF run.

Figure 2.10: Allowed hit patterns for DI-HOPU trigger boards.



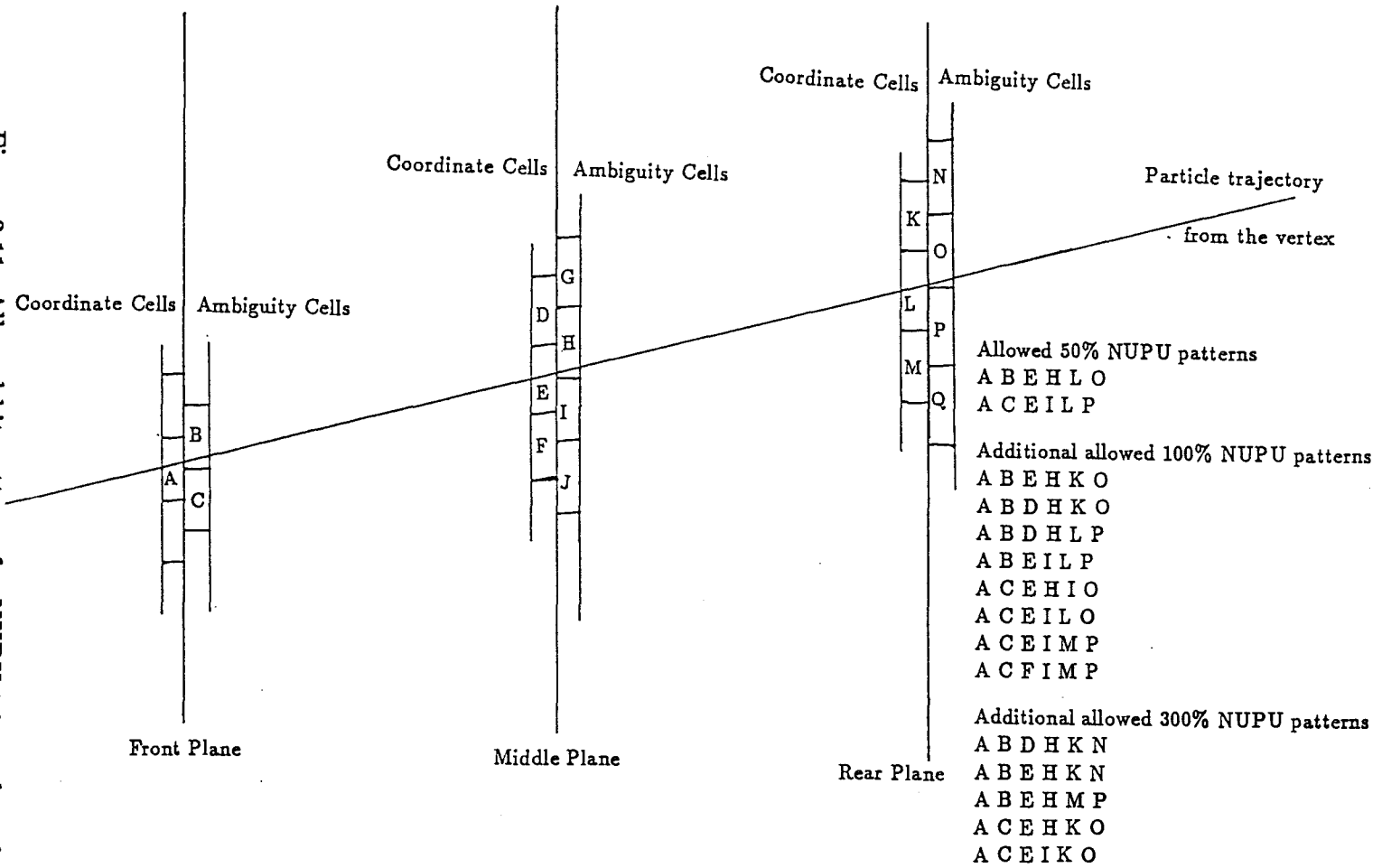
The SHAMPU unit performed several functions. Initially, even before the HOPU unit completed its pattern search, the SHAMPU unit looked for hits in the scintillator wedges for coincidences and formed a logical OR of all the wedges in one octant. The scintillator information for each octant was sent to the corresponding HOPU and was used by that unit as a requirement for a trigger. The SHAMPU unit also acted as a receiver for the information from the HOPU's. It determined if there was a coincidence between a coordinate and ambiguity HOPU. Thus, a FMU Level1 trigger required a scintillator match along with a coincidence between a coordinate and ambiguity HOPU.

2.3.5.2 The NUPU Trigger Boards

In the second trigger the 3 coordinate wires were required to line up in both η and ϕ with the 3 ambiguity wires. This was achieved with a new trigger board that searched for a 6 wire coincidence within one octant. One New Half Octant Pattern Units, called a NUPU, replaced both the coordinate and ambiguity HOPUs.

The NUPU boards shipped wire coincidence information for three thresholds to the PUCKER module which usurped the SHAMPU module. Figure 2.11 shows the allowed hit patterns for all three NUPU P_t thresholds. The NUPU 50% threshold was used to select data and used hit patterns identical to the DI-HOPU 100% P_t threshold trigger for drift cells with the first coordinate wire > 32 . The PUCKER module also received the scintillator information from the SHAMPU and correlated the wire triggers with the scintillator coincidences to

Figure 2.11: Allowed hit patterns for NUPU trigger boards.



determine the FMU level 1 trigger.

2.3.5.3 The Level1 Geometric Trigger Efficiency

The geometric trigger acceptance as a function of transverse momentum was determined using a forward muon detector simulator [24]. (This program is discussed in greater detail in Chapter 3.) For the present discussion, however muons with fixed P_t and fixed charge were generated uniformly over detector end and azimuth position. The θ distribution was also uniformly distributed and included the effects of a vertex smeared about the interaction point by $\sigma = 30\text{cm}$.

The NUPU 50% trigger differed from the DI-HOPU 100% trigger for wire cells 28 - 32 due to the hardware design of the boards. For the remainder of the wires cells, however the NUPU 50% trigger efficiency as a function of P_t is identical to the DI-HOPU 100% curve due to the fact that the allowed hit patterns are identical. For that reason, the data acceptance uses only wire cells 33-55.

The NUPU 50% trigger efficiency as a function of P_t was also found to be independent of the choice of wire cell as shown in figure 2.12. The combined efficiency for wires ≥ 33 is shown in figure 2.13 for both positive and negative charges. A trigger preference for negatively charged muons exists due to the fact that muons enter the toroids at an angle. Because the toroidal field defocuses positively charged tracks, they undergo a larger multiple scattering and thus see more magnetic field than the negatively charged tracks. For this reason the positively charged tracks are bent out of the trigger road more frequently than

the negatively charged ones [23].

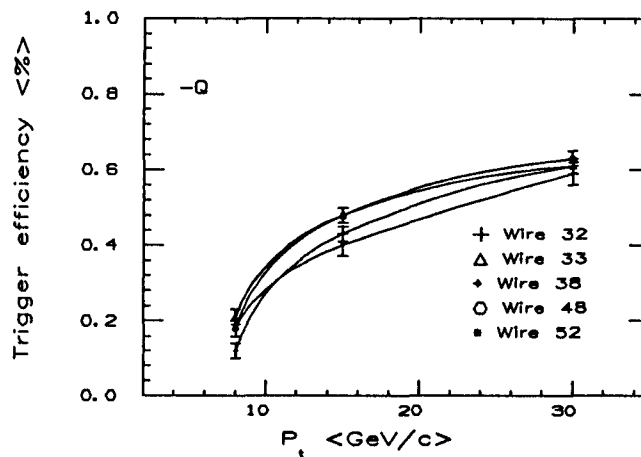


Figure 2.12: Trigger efficiency for wire 32 compared to the other wires.

2.3.5.4 FMU Level2 and Level3 Triggers

The Level2 trigger acceptance was automatic for FMU, except for a pre-set maximum trigger rate of 0.1Hz. The FMU Level3 trigger used the offline tracking code to require a reconstructed muon track with no quality cuts.

2.3.5.5 Detector Contributions to the Trigger Efficiencies

The FMU detector contributions to the trigger efficiencies include four sources of deadness. First, there are failures of groups of wires or of entire wire chambers. Second, there are single wire efficiencies. Third, there are trigger losses from

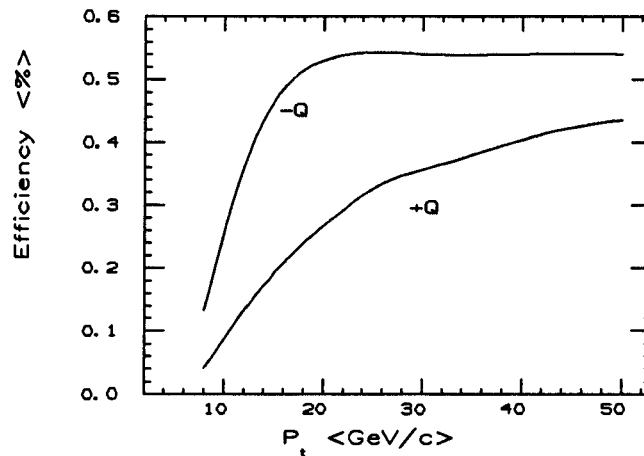


Figure 2.13: NUPU 50 Trigger Efficiency

broken components in the trigger boards and associated connectors and cables and fourth, there are losses due to scintillator efficiencies. The detector efficiency is the product of these four numbers.

There were several complications in determining the detector efficiencies due to changes in the detector configuration during the 1988-89 run. The first of these has already been discussed and this was due to the fact that several trigger configurations were used. The second complication was the result of an HV accident which occurred during December 1988. Since many channels were disabled, the chambers with their associated electronics were removed from the collision hall and fixed. When the chambers and electronics were reinstalled, the prior arrangement was not preserved.

RUNS	TRIG	CDF $\int L dt$ (1/nb)	FMU $\int L dt$ (1/nb)
R15880 - R16566	HOPU	102.1 \pm 6.9	4.9 \pm 1.9
R16567 - R18199	DI-HOPU	1345.2 \pm 91.5	668.4 \pm 63.2
Christmas Repair			
R18685 - R18847	DI-HOPU	139.0 \pm 9.5	92.1 \pm 6.7
R18848 - End	NUPU	2047.1 \pm 139.2	1037.1 \pm 70.7
total		4060.2 \pm 276.1	1802.5 \pm 142.5

Table 2.1: FMU trigger configurations and associated luminosity for the 1988-89 CDF run

The FMU detector efficiency is thus defined for four data taking periods, The effects of wire group failures, single wire efficiencies, trigger electronics efficiencies and scintillator efficiencies are combined to determine the detector efficiency for that period. The average of the products, weighted by the FMU luminosity for each trigger configuration, is the overall efficiency for the 1988-89 CDF run. The combined result is an efficiency of $.457 \pm .023$ on the west end and $.368 \pm .019$ on the east end. The run numbers and luminosities for the relevant portions of the run are listed in Table 2.1. Table 2.2 lists the detector contributions to the trigger efficiencies separately for the east and west ends of the detector for each portion of the run [25]. Each of the detector contributions is now described in more detail.

	R15880-16566	R16567-18199	R18685-18847	R18848-End	weighted average
6 hit eff.					
west	.620 ± .036	.620 ± .036	.631 ± .028	.631 ± .028	
east	.421 ± .046	.421 ± .046	.592 ± .029	.592 ± .029	
group eff.					
west	.787 ± .060	.870 ± .086	.895 ± .014	.937 ± .011	
east	.774 ± .087	.846 ± .071	.621 ± .009	.957 ± .009	
single eff.					
west	1.00 ± .01	1.00 ± .01	1.0 ± .01	1.0 ± .01	
east	.917 ± .009	.917 ± .009	.958 ± .010	.958 ± .010	
scint. eff.					
west	.751 ± .024	.751 ± .024	.751 ± .024	.978 ± .014	
east	.733 ± .028	.733 ± .028	.751 ± .028	.976 ± .014	
trig elec eff					
west	1.00 ± 0.00	.903 ± .014	.903 ± .014	.903 ± .014	
east	1.00 ± 0.00	.903 ± .014	.903 ± .014	.903 ± .014	
overall trig					
west eff	.366 ± .037	.366 ± .044	.383 ± .023	.522 ± .026	.457 ± .023
east eff	.219 ± .035	.216 ± .031	.233 ± .016	.478 ± .026	.368 ± .019

Table 2.2: Contributions to the efficiency from detector components.

2.3.5.6 Group Failures and Single Chamber Losses

Failures of groups of wires or of entire wire chamber octants occurred due to broken HV connections or gas impurities caused by leaks in the wire chambers. A similar effect occasionally resulted from TDCs which were temporarily disabled to mask hot FMU trigger octants. A group failure removes two hits from a 6-hit track since each chamber contains both a coordinate and ambiguity plane. Therefore, group failures are not counted by the single hit efficiency calculation which uses the ratio of 5-hit to 6-hit tracks. The group failures were identified on a run by run basis by observing wire occupancies [26].

There were three chambers which failed to produce any hits or tracks in the CDF 1988-89 run. On the east end of the detector, two chambers in one run configuration and one chamber in a second run configuration contain no tracks. Since there are 24 chambers in a plane, the efficiency of the remaining chambers is

$$\epsilon_{sc} = \frac{\text{working chambers}}{24}. \quad (2.6)$$

This is called "single eff" in Table 2.2.

2.3.5.7 Single Wire Efficiencies

The single wire efficiency is a measure of the uncorrelated losses of trigger roads when a single wire was absent from the trigger. These losses are best measured by sampling tracks in events which were recorded due to some non FMU trigger.

The number of tracks which are missing a single chamber hit is compared to the number with all six hits in order to determine the single wire efficiency. Using this method, the efficiency is found to range from 86.5% to 92.4% for different sections of the 1988-89 CDF run. The efficiency for a 6-hit track is ϵ^6 and this is called "6 hit eff." in Table 2.2 in

2.3.5.8 Trigger Electronics Efficiency

The majority of the forward muon data ($P_t > 5$) was collected using the NUPU 50% trigger. This trigger was installed for all runs greater than 18848, excluding special runs. Events selected by some non-FMU trigger were used to determine if the hardware performed as expected. (This is different than the geometric trigger road efficiency which was described earlier.)

The trigger electronics in efficiency is accounted for by a small number of mechanical failures in the jumper wires between the TDC and the NUPU boards. Due to a similar hardware arrangement for the DI-HOPU trigger, we use the same number for this run configuration.

2.3.5.9 Losses Due to Scintillator Efficiencies

Since a coincidence of the DI-HOPU or NUPU trigger with a scintillator match was required for runs prior to run 18848 during 1988-89 CDF run, trigger losses were also attributed to scintillator efficiencies. This efficiency was measured by looking for an associated scintillator match in volunteer muon tracks. As noted

in Section 3.4, however, even before considering the scintillator efficiency, the requirement of a scintillator match in the trigger reduces the acceptance to approximately 96% due to ϕ gaps. Runs without the scintillator requirement were assigned a 100% efficiency.

2.3.6 The FMU Luminosity

The forward muon triggered data sample received less luminosity than the rest of the CDF detector due to a prescale factor and to short periods when the FMU trigger was disabled. The prescale factor was a result of the .1Hz Level2 rate limit and therefore changed as the instantaneous luminosity changed. The majority of the prescaling occurred during high luminosity runs since at a luminosity equal to $L = (10^{30})\text{cm}^{-2}\text{sec}^{-1}$, the Forward muon Level1 trigger rate was approximately equal to .1Hz. Figure 2.14 shows the average FMU Level1 rate as a function of average integrated luminosity.

The CDF luminosity has been calculated for each tape based on the number of beam-beam (see Section 2.2.3) corrected for multiple interactions in a single crossing. The FMU luminosity is calculated by multiplying the CDF luminosity by the FMU trigger prescale factor on a run by run basis. The run numbers and luminosities for the relevant portions of the run are listed in Table 2.2. Error bars include a 6.8% uncertainty in the CDF luminosity, statistical errors from the Level1 and Level2 scaler values. The FMU integrated luminosity is $(1.802 \pm .142)pb^{-1}$. This reflects an average prescale factor of .45 and $(4.060 \pm .276)pb^{-1}$ of CDF integrated

luminosity.

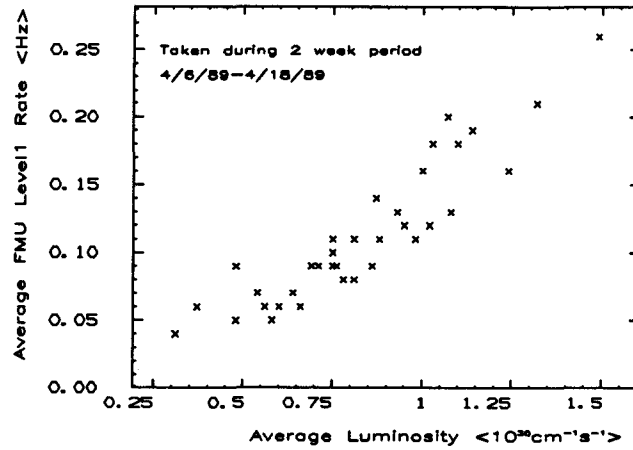


Figure 2.14: Average FMU Level1 Rate vs Average Integrated Luminosity

2.3.7 The FMU Momentum Resolution

The momentum resolution $\Delta P/P$ of the forward muon detector was also determined using the FMU fast M.C. simulation and is expressed as

$$\frac{\Delta p}{p} = \sqrt{(.166)^2 + (.0019 * P/GeV)^2} \quad (2.7)$$

The components are multiple scattering, chamber resolution and survey misalignment. Table 2.3 lists the momentum resolution for each of these components. As shown in this table, the resolution from multiple scattering is momentum independent [23] and for muons up to momenta of $100 \text{ GeV}/c$, the resolution is

Momentum Resolution Components	$\Delta P/P$
Multiple Scattering	$.166 \pm .004$
Chamber Resolution = 650 microns	$.0015 \pm .0003 * P$
Survey Uncertainties	$.0012 \pm .0003 * P$

Table 2.3: Momentum Resolution for Multiple Scattering, Chamber Resolution and Survey Uncertainties.

dominated by the multiple scattering. As the momentum exceeds 100 GeV/c, the chamber resolution and survey errors become significant. Muons arising from the decay of W and Z's produced in the forward region have average momenta around 150 GeV/c with some muon momenta extending beyond 200 GeV/c. Thus the effect of the latter two resolution components is quite significant to this analysis.

The specifics of the survey and alignment of the forward muon drift chambers is described in detail elsewhere [23]. However, to understand the errors introduced by misalignment, a brief description is repeated here. The forward muon drift chambers were mounted with precision located dowel pins to an aluminum support frame which consisted of 2 separable half circles. Figure 2.15 shows the general features of how a drift chamber attaches to the aluminum support frame. The survey alignment was performed by measuring the (x,y) position of tooling balls which were attached to the inner radius of several drift chambers

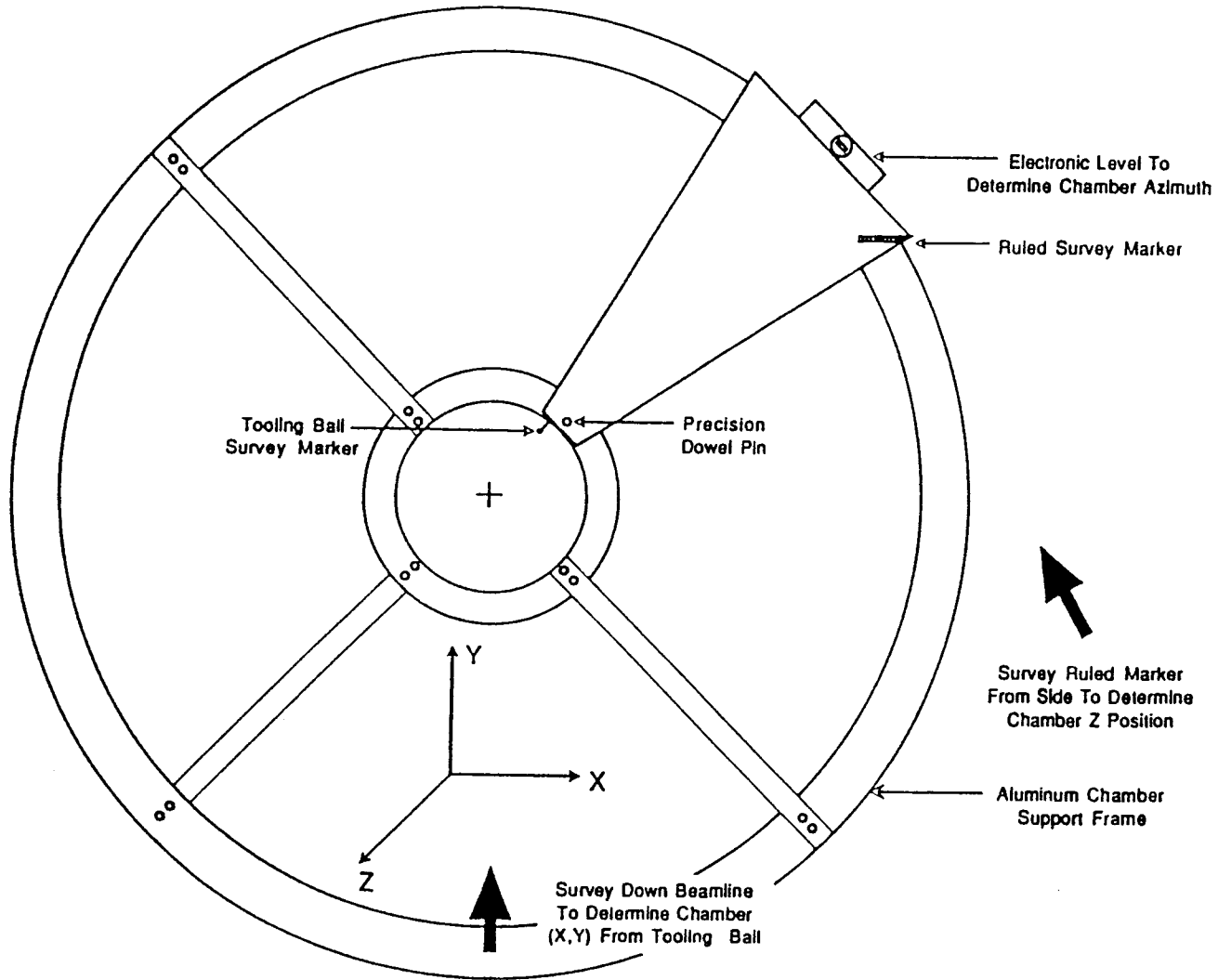
for each plane. The tooling balls were then referenced to the dowel pins which attached the drift chambers to the aluminum frame. The (z) positions of the drift chambers were determined by surveying the precision rulers attached to both the outer and inner radii of the chambers. This method of surveying was estimated to introduce a (x,y) error of +/- 500 microns using typically 5 tooling balls per chamber plane. Using on average 6 precision rulers per plane, the (z) error was estimated at 2. mm. The curvature of the track is less sensitive to z errors. A (z) error of 2.0 mm can be compared to a position radius error by the relationship $\delta r = \delta z * \tan \theta = 472$ microns at $\theta = 12^\circ$ [23].

Figure 2.16 is a plot of the momentum resolution and shows the effect of both the chamber resolution and survey error to the momentum resolution.

The FMU-CMU Z candidates were used to calibrate the momentum resolution of the FMU system. This value is also plotted in figure 2.16 for a comparison against monte carlo predictions. The momentum resolution used for determining the CMU momentum was good to within .1% P_t GeV/c and the angle of the FMU was well measured. If the FMU-CMU invariant mass is constrained to be 91.1 GEV, then the true FMU momentum, P_{true} can be determined. The quantity P_{true} can be used to determine the relative curvature error by the following equation [27]

$$\begin{aligned} \Delta P &= P_{FMU} - P_{true} \\ \text{Relative Curvature Error} &= \frac{Q}{\Delta P} \end{aligned} \quad (2.8)$$

Figure 2.15: Schematic of FMU survey procedure



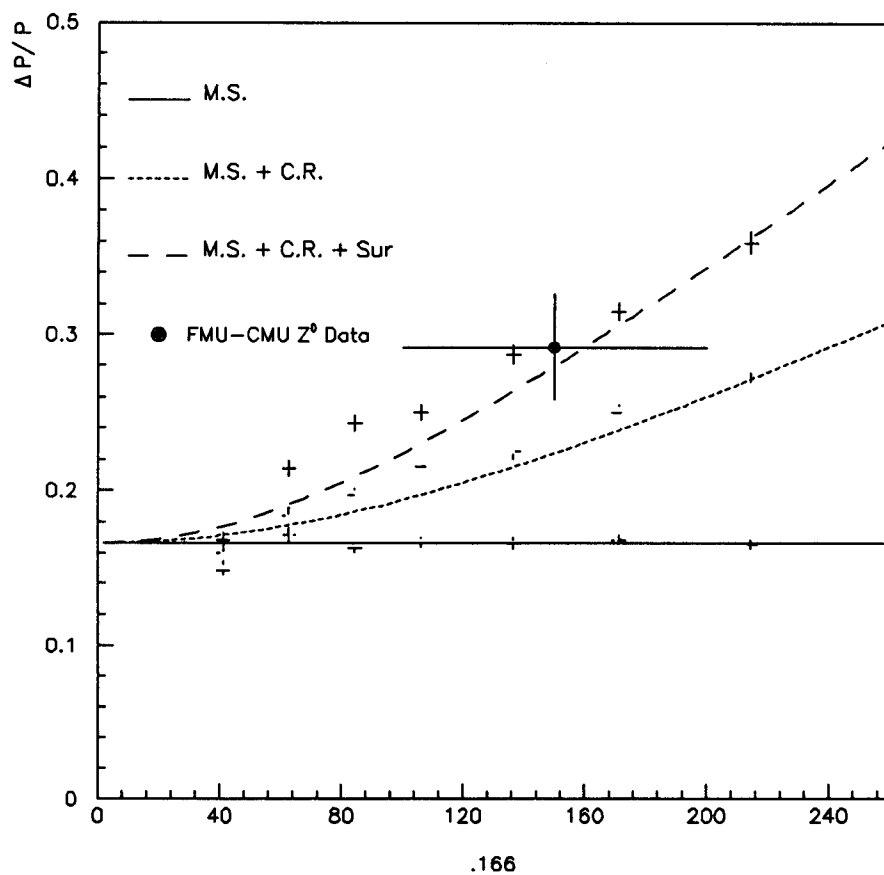


Figure 2.16: Cumulative Momenta Resolution vs Momenta

where Q is the measured charge of the forward muon track. The relative curvature error is plotted in Figure 2.17a and we estimate the momentum resolution of the FMU system from the sigma of this distribution to be $.292 \pm .068$. Alternately, we plot the invariant FMU-CMU Z^0 mass in Figure 2.17c and estimate the FMU momentum resolution from the width of this figure to get $\Delta P/P = .237 \pm .051$. These two estimates for the FMU momentum resolution agree with each other and with the estimate from a Monte Carlo analysis.

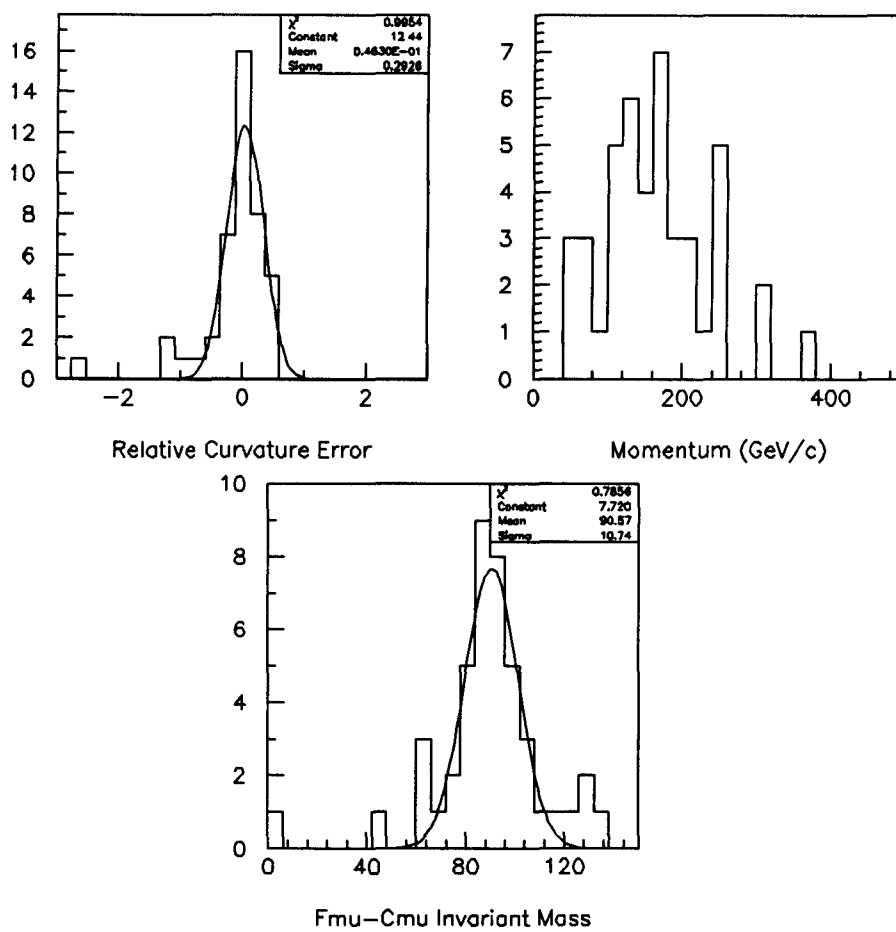


Figure 2.17: FMU - CMU Z^0 Invariant Mass $\langle GeV \rangle$

Chapter 3

The Inclusive

Forward/Backward Muons

3.1 Introduction

In this chapter, I discuss the inclusive muon data and show some inclusive spectrums. In the next chapter, I then focus on one part of the inclusive P_t spectrum, namely $P_t > 18\text{GeV}/c$ and study muon events from the process $W^\pm \rightarrow \mu^\pm \nu$.

3.2 The FMU Inclusive Data

The forward muon inclusive data set consists of forward muon triggered events selected from the MUO04 Production stream. The CDF production stream was a set of data tapes analyzed with the latest calibrations for tracking, calorimetry, etc. Forward muon events were written to this stream if a forward muon object

bank (FMUO) was present. An FMUO bank was created if the tracking algorithm was able to fit a track with a minimum of 5 chamber hits in a 1-3-3 road configuration that was constrained to pass through the nominal event vertex. (See Figure 2.11 for a description of the 1-3-3 road configuration.)

Tracks were reconstructed with the FMTRK module using a chamber resolution of 650 microns [22] as well as a radial matching requirement of .5cm to associate coordinate-ambiguity wire hits. In addition, a pad threshold of 800 ADC counts was used to identify the azimuth position to within 5° . If the first plane had an unambiguous signal, the track ϕ would be determined at this plane. However, if there were two or more pad signals above a user specified threshold (The optimal value was found to be in the range of 500-1000 ADC counts), the fitting algorithm would skip this plane and proceed to plane 2 to determine the track ϕ position. If the fitting algorithm was able to determine ϕ from a pad signal, the error in the ϕ measurement would be set to $\pm 2.5^\circ$. If all 3 planes of pads were ambiguous, the fitting algorithm would use the scintillator counters to determine track ϕ and the error would be set to $\pm 7.5^\circ$. If a unique ϕ could not be determined by the scintillators, the fitting algorithm would assign the muon azimuthal position at the middle of the octant and the error would be set to $\pm 22.5^\circ$. Since the curvature of tracks in the forward toroids is in the $r - \theta$ direction, the momentum measurement is less sensitive to ϕ uncertainties. The fitting algorithm also required the coordinate-ambiguity match to be within .5cm and the chamber resolution was set at 650 μ .

The original tracking code executed in production used a different version of the FMTRK module with 500 micron resolution and no pad ADC threshold. The newer version included several minor tracking fixes, plus the 1988-89 survey constants. Since there were no initial track quality cuts on the data, there is no efficiency associated with this revision.

After the retracking (second iteration of tracking), there were 79,731 muon candidates. These events were then required to satisfy quality cuts listed below. These cuts will be referred to as the "standard FMU cuts". These cuts are discussed in more detail in Section 3.3.

- Calorimeter energy cut depending on which calorimeter the track traversed.
 1. Forward electromagnetic calorimeter (FEM) > .2GeV
 2. Forward hadronic calorimeter (FHA) > 1.5GeV
 3. Plug electromagnetic calorimeter (PEM) > .1GeV
 4. Plug hadronic calorimeter (PHA) > .9GeV
- Track fit must have a χ^2 probability ($P(\chi^2) > .02.$)
- The first hit is on wire ($W) \geq 33$. The allowed range $33 \leq W \leq 55$ corresponds to $2.65 \leq |\eta| \leq 1.95$ for an event vertex $z_{vtx}=0$.
- Number of FMU TDC hits used in the fit = 6 (out of a possible 6).
- Require that hits used in the track fit satisfy the 1-1-1 road configuration

which defines a valid FMU trigger. (See Figure 2.11 for a description of the 1-1-1 road configuration.)

- The number of FMU TDC hits (Maxhit) is 17 or less in the region $3^\circ < \theta < 16^\circ$ in the triggered octant containing the track. (6 hits in an octant constitute a trigger).
- Forward Muon Level2 required. The Level2 trigger was identical to the Level1 trigger except for the prescale factor.
- One VTCS bank required with $|z_{vtx}| < 100\text{cm}$. The VTPC track was not required to match the FMU track.
- Track $P_t > 6\text{GeV}/c$

We are left with 2,822 events after requiring the standard cuts. These events comprise the inclusive forward muon data set used in this analysis.

3.3 Cut Efficiencies

3.3.1 The Calorimetry Cut

Muons are identified in part by the minimum ionizing signal which they deposit in the calorimetry. The calorimeter energy signal for forward muon tracks is defined to be the sum of energy in a 3 x 3 array of calorimeter towers centered on the muon. This corresponds to a cone of $.1 \leq \Delta R \leq .2$ around the muon where $\Delta R = \sqrt{\Delta\phi^2 + \Delta\eta^2}$. For muons pointing to the middle of a calorimetry

tower, $\Delta R \leq .15$. Cut values were determined from a sample of clean forward muon events that were selected using the standard cuts with the exclusion of the calorimetry cut. In addition, the muons were required to have a pad signal (ADC counts > 1000) in the $\eta - \phi$ tower associated with the muon in two of the three chamber planes as well as have an accompanying stub in the VTPC chambers with track matching parameters satisfying $|\theta_{fmu} - \theta_{vtpc}| < 1.5^\circ$ and $|\phi_{fmu} - \phi_{vtpc}| < 15^\circ$. The electromagnetic and hadronic energy distributions for these events are shown in Figure 3.1 for both forward and plug calorimeters. All of the calorimeters show a clean minimum ionizing signal which peaks at about .7GeV in the electromagnetic calorimeters and at about 3GeV in the hadronic calorimeters. Efficiencies for muons passing several calorimeter cut thresholds are listed in Table 3.1.

Also determined was the probability for selecting random noise in the calorimeter. A cone, which was identical in size to the associated muon cone, was randomly selected in either the plug or forward regions. The cone was centered on a tower that was at least four η towers and/or five ϕ towers from the muon tower. The percentage of random towers passing the calorimeter cuts is also listed in table 3.1.

From the data, we determined that the following cuts would preferentially select for muons: .1GeV of energy in the PEM, .9GeV of energy in the PHA, .2GeV of energy in the FEM and 1.5GeV of energy in the FHA. These values were selected so that the plug and forward calorimetry efficiencies would match

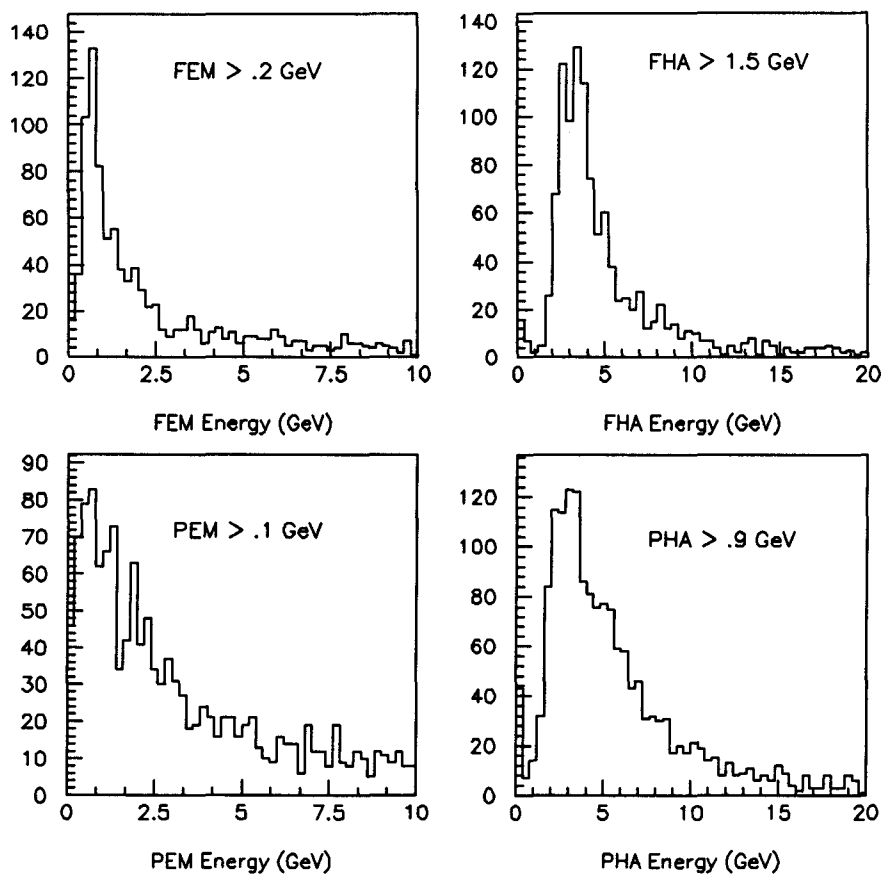


Figure 3.1: Energy distributions for inclusive forward muon events.

	Muons passing cut	Random towers passing cut
Forward	(%)	(%)
Em >.1 and Ha>1.	98.5±.4	13.2±.9
Em >.2 and Ha>1.	98.2±.4	11.8±.9
Em >.2 and Ha>1.5	97.9±.4	7.8±.8
Plug		
Em >.1 and Ha>.9	97.0±.5	4.8±.5
Em >.15 and Ha>1.	96.3±.6	3.9±.4
Em >.15 and Ha>1.5	94.8±.7	3.1±.5

Table 3.1: Efficiencies for finding a muon or random tower which passes a minimum energy requirement

each other as well as minimize the amount of random noise. These cut values were found to be $97.4 \pm .5\%$ efficient at selecting forward muons.

3.3.2 Six Hit Fit satisfying a 1-1-1 Road

Since the FMU level1 trigger required 6 hits to satisfy the 1-1-1 road configuration, the requirement that the offline tracking algorithm also use 6 hits in the track fit is somewhat redundant. It is listed as a cut because the number of hits used for a track fit is allowed to be either 5 or 6 depending on which fit produces

the lowest χ^2 .

The level3 online tracking algorithm required a minimum of 5 hits to be used in the track fit and these hits were required to satisfy the 1-1-1 road configuration. In the offline reconstruction the road is enlarged to 1-3-3 to allow for volunteer forward muon events. Figure 2.11 of Chapter 2 showed the geometry specifications for the 1-1-1 and 1-3-3 road configuration. It is often the case that an event with extra hits will satisfy the level1 trigger and level3 reconstruction requirements, but when the reconstruction road is enlarged the tracking algorithm will use a different set of hits to produce a fit with a lower χ^2 . In this case, the track fit with the lowest χ^2 is most likely the true track and the event is selected because extra hits satisfy the muon trigger. By requiring that the offline reconstruction match the online reconstruction (of level3), we eliminate the events selected because extra hits had satisfied the trigger.

3.3.3 The Track Fit $P(\chi^2)$ Cut

The track fit χ^2 probability, $P(\chi^2)$ was required to be $P(\chi^2) > .02$. A detailed description of the χ^2 distribution of the forward muon fitting algorithm is explained in Appendix 1. We summarize those results here.

Ideally, requiring the $P(\chi^2)$ to be greater than .02 should be 98% efficient at selecting signal events. However, this efficiency is degraded due to chamber efficiency, the production of extra hits, the 100ns deadtime required by the FMU electronics for identifying multiple hits in a signal drift cell, and survey misalign-

ments. The effect of each of these contributions is listed in Table A.2 of Appendix 1.

Figure 3.2a shows the $P(\chi^2)$ distribution for muons selected using the standard cuts with the exclusion of the $P(\chi^2)$ cut. The efficiency for selecting W^\pm/Z^0 signal events with $P(\chi^2) > .02$ was estimated to be $88.7 \pm .1\%$ from a detector simulation of W and Z^0 decays. The efficiency for selecting simulated muons with generated $P_t > 6\text{GeV}/c$ was found to be consistent with this number. Once the input simulated muon P_t was allowed to be less than $6\text{GeV}/c$ however, mismeasured very soft muons degraded the $P(\chi^2)$ efficiency value slightly for simulated bottom and charm muons and severely for simulated minimum bias muons. Since we are only interested in muons with $P_t > 6\text{GeV}/c$, the $P(\chi^2)$ efficiency for detecting these events should be similar for all muon sources.

3.3.4 The Maxhit Cut

The number of FMU TDC hits in the track octant was also used to select good muon events. A minimum of 6 hits in the drift chambers is required for a triggered muon event. The production of extra hits from processes like delta rays and bremsstrahlung interactions can increase the number of observed hits. These physics processes are modeled in the simulation. Another process which can produce extra hits occurs when the protons circulating in the main ring scrape the walls of the beam pipe in the main ring tunnel to produce hits in the forward muon chambers which is termed "main ring splash". No attempts are made at

trying to model this spurious process. Instead, a cut on the maximum number of TDC hits (Maxhits) in the region $3^\circ < \theta < 16^\circ$ for the triggered octant is used to eliminate events contaminated with main ring splash. This cut can be calibrated due to the fact that main ring splash has the characteristic signature of producing extra hits in only the top half of the detector. This is because the main ring beam pipe circulates above the CDF detector. This splash is more easily identified in events without the $P(\chi^2)$ cut. Figure 3.2b shows the Maxhit vs azimuthal angle distribution for muons which were required to pass the standard cuts with the exclusion of both the Maxhit cut and the $P(\chi^2)$ cut. The enhancement of total hits in the triggered octant for muons in the upper half of the detector, ($0^\circ < \phi < 180^\circ$) is clearly evident. From this figure, we determined that a cut of $\text{Maxhit} \leq 17$ would get rid of these splash events. From the figure, we see this value is not a crisply defined quantity. The motivation for choosing our value is based on the FMU-CMU Z^0 Maxhit distribution which is shown in Figure 3.3.

Since the statistics of the FMU-CMU Z^0 data set were small, the efficiency of this cut was determined for real events (i.e. non-splash events) using the sample of clean forward muon events that had passed the standard muon cuts with the exclusion of the Maxhit cut and that had travelled through the bottom half of the detector. In addition, these muons were required to have a pad signal (ADC counts > 1000) in the $\eta - \phi$ tower associated with the muon in two of the three chamber planes as well as have an accompanying stub in the VTPC chambers with

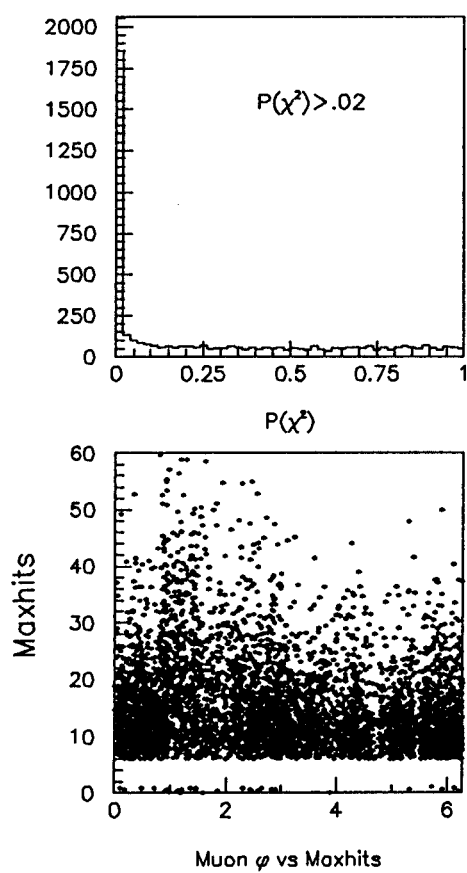


Figure 3.2: The $P(\chi^2)$ distribution and the Maxhit vs Muon azimuth scatter plot for forward muon events.

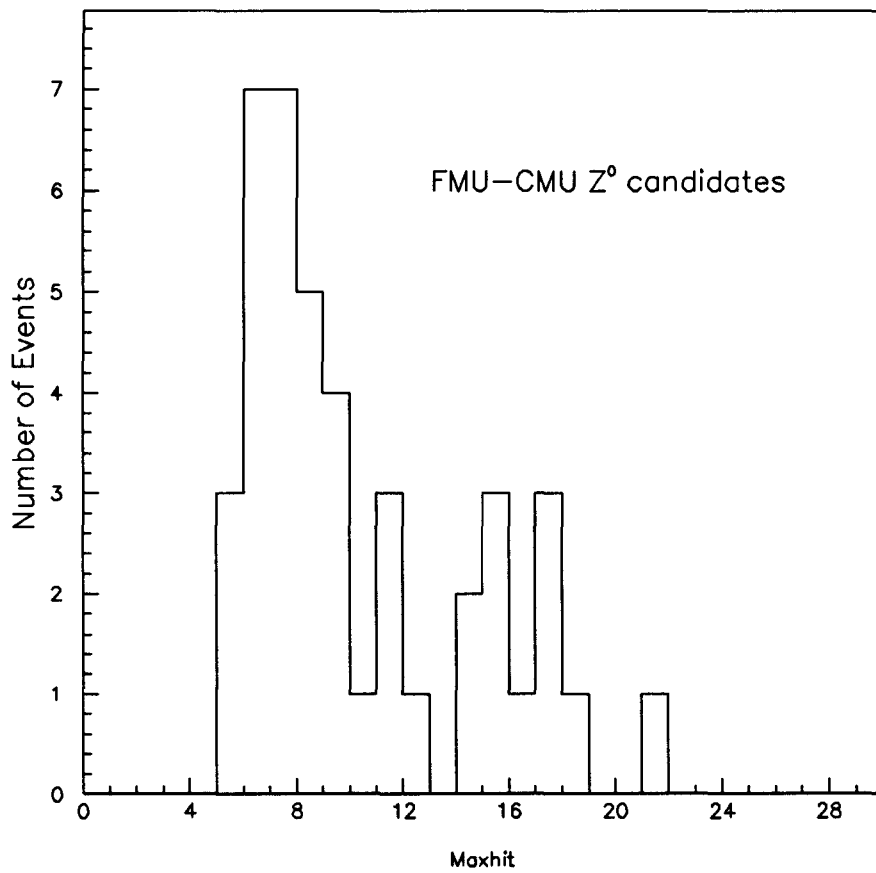


Figure 3.3: Maxhit Distribution for forward muons from FMU-CMU Z^0 candidates.

Maxhit Cut Value	Efficiency for $180^\circ < \phi < 360^\circ$
≤ 15	$.79 \pm .01$
≤ 17	$.86 \pm .01$
≤ 19	$.914 \pm .009$
≤ 23	$.988 \pm .004$

Table 3.2: Efficiencies for finding a muon which passes a maximum number of allowed FMU TDC hits in the trigger octant.

track matching parameters passing $|\theta_{fmu} - \theta_{vtpc}| < 1.5^\circ$ and $|\phi_{fmu} - \phi_{vtpc}| < 15^\circ$. The efficiencies for several Maxhit values are listed in Table 3.2 for the lower half of the detector. (This efficiency was verified using a subset of the clean sample of muons, the muon plus jet events. For this case, the events were required to have the largest cluster of energy, $E_t > 10\text{GeV}$. Muons were also required to satisfy $\Delta r < .6$ where $\Delta r = \sqrt{\Delta\phi_{\mu-jt}^2 + \Delta\eta_{\mu-jt}^2}$. The muon plus jet Maxhit efficiency values were the same within statistics as the quoted values in Table 3.2.)

3.3.5 Fake Muon Contamination

A fake muon is a track reconstructed from random chamber background hits. The muon events selected by the standard cuts are estimated to contain less than 1% fake muon contamination. The forward muon pad signals are used to support

this assertion. Figure 3.4a is the pad adc signal for the inclusive muons where the pad signal from all three planes of drift chambers are shown in the figure for the $\eta - \phi$ tower associated with the muon. Shown in Figure 3.4b is the same plot for the opposite ϕ pad tower. A typical muon will show a pad ADC signal of greater than 2000 adc counts while a fake muon will show less than 1000 adc counts and more likely 0 ADC counts. The pile up at zero observed in figure 3.4a is not entirely attributed to a fake muon signal (4.8% of events in this figure have less than 1000 adc counts in more than 1 chamber plane). Most of these zeros are more a result of the track ϕ uncertainty in the fit and pad inefficiency than of a fake muon signal.

Since the ϕ of the track is determined by the first unambiguous pad signal, muons crossing the ϕ boundary between planes would show a strip signal in a different ϕ tower for different planes. This will result in some fraction of events which show an ADC signal in neighboring ϕ towers between planes. Figure 3.4c is a distribution of the sum of adc counts in the 1×3 ($\eta - \phi$) array of towers $(\eta) - (\phi - 5^\circ, \phi, \phi + 5^\circ)$ centered on the muon. Only .3% of the events in Figure 3.4c have less than 1000 ADC counts in more than one chamber plane. Figure 3.4d is a similar plot of the adc counts in the 1×3 array of towers centered on the ϕ opposite to the muon.

This .3% can further be attributed to inefficient or broken pad channels rather than fake muon contamination. Broken pad channels are identified as channels which never recorded a signal larger than the pedestal of the Rabbit electronics.

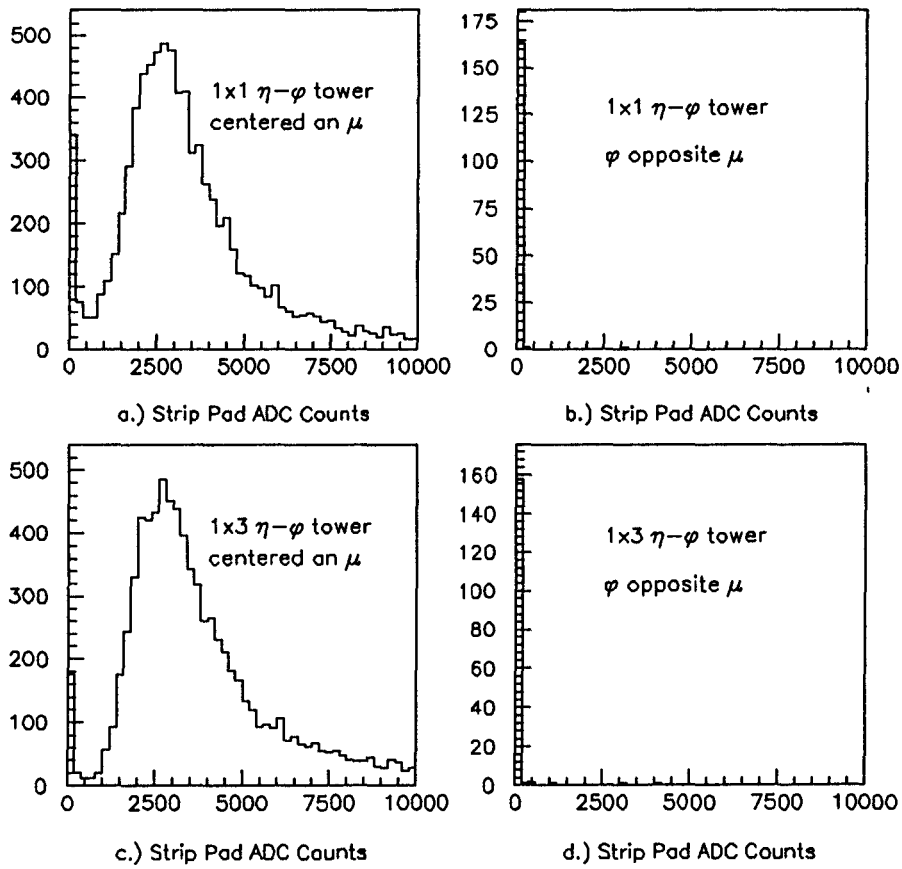


Figure 3.4: Strip Pad Distributions for Inclusive Muon Events a.) 1x1 tower centered on muon. b.) 1x1 tower centered on $\phi \pm 180^\circ$ from muon. c.) 1x3 tower centered on muon. d) 1x3 tower centered on $\phi \pm 180^\circ$.

A small percentage, $(2.62 \pm .46)\%$, of the pad channels never registered more than 1000 ADC counts during the whole run [28]. These broken channels are the major contributor to the pad inefficiency. The probability that three pads will have two or more dead channels is $(.20 \pm .08)\%$ which is comparable with the residual fake muon background estimate.

In conclusion, the fake muon contamination is estimated to be less than 1% for muons satisfying the standard cuts listed in section 2 once the neighboring $\eta - \phi$ strip towers are searched for the muon signal.

3.3.6 Overall Efficiencies

The FMU detector efficiencies were listed in Table 2.2 of Chapter 2. The overall efficiency for the inclusive FMU sample is defined as the product of the FMU detector efficiency with the selection cut efficiencies. This is listed in Table 3.3. The selection cuts include the calorimetry cut, the multi-hit splash cut, and the $P(\chi^2)$ cut. The efficiency for these three data cuts was determined in earlier sections. Since selection cuts are not expected to be correlated, the overall efficiency is just the product of the individual cut efficiencies.

Not included in the selection cut efficiencies is the geometric trigger acceptance, including the requirement that the reconstructed track satisfy an allowed trigger pattern (1-1-1 road cut) and that triggers are used only for coordinate wires 33-55. The 1-1-1 road cut reflects the online trigger requirements and is included in the geometric trigger efficiency. The acceptance of the detector and

Efficiency Description	East Side Efficiency	West Side Efficiency
Calorimetry cut	.974±.005	.974±.005
Maxhits≤17	.86±.01	.86±.01
$P(\chi^2) > .02$.887±.010	.887±.010
Trigger Detector Eff. (Chamber Eff.+ Scint. Eff. + Group Eff.)	.368±.019	.457±.023
Overall Efficiency	.273±.015	.340±.018

Table 3.3: Efficiency of Inclusive Muon cuts

trigger are implemented in the detector simulation monte-carlo.

3.4 Simulations

3.4.1 Decay-in-flight Spectrum

In order to simulate the background due to decay-in-flight muons, it is necessary to know the P_t and η spectra of the parent particles (π, K) in the forward region. Minimum bias muons are generated from π and K decays. One simulation uncertainty is how this spectrum breaks up into π, K and protons(p). This is presumably P_t dependent for hadron P_t 's less than a few GeV/c. At hadron

P_t 's larger than a few GeV, the K/π and p/π ratios are believed to be constant [29], [30]. For the P_t values relevant to this analysis, we use a constant particle composition of $58\pm 12\%$ pions, $21\pm 4\%$ kaons and $21\pm 4\%$ protons.

The minimum bias normalization is determined using the minimum bias cross section and the integrated luminosity into the FMU system. (The details of this calculation are in Appendix 2.) The minimum bias cross section for decay in flight muons with $P_t > 2\text{GeV}/c$ is given by

$$\sigma(\pi \rightarrow \mu, K \rightarrow \mu)_{P_t > 2\text{GeV}/c} = 10338.5 \pm 1344.0nb \quad (3.1)$$

3.4.2 $W^\pm \rightarrow \mu^\pm \nu$ and $Z^0 \rightarrow \mu^+ \mu^-$ Spectra.

ISAJET was used to generate bosons from collisions of quark and antiquarks in the proton and antiproton and then to decay the W^\pm into muon-neutrino pairs or decay the Z^0 into muon-muon pairs. Only zeroth order diagrams were included using the EHLQ1 structure functions. The W^\pm mass was assumed to be $80\text{GeV}/c^2$ and the Z^0 mass was assumed to be $90\text{GeV}/c^2$.

The normalization is determined using the W^\pm/Z^0 cross section and the integral luminosity into the FMU system. The boson cross sections used in this analysis are CDF results [31].

$$\sigma(W^\pm \rightarrow \mu^\pm \nu) = 2.23 \pm .200nb \quad (3.2)$$

$$\sigma(Z^0 \rightarrow \mu^+ \mu^-) = .217 \pm .021nb. \quad (3.3)$$

3.4.3 Bottom and Charm Decays

[28] Bottom and charm events are generated with ISAJET version 6.21. This program uses tree level diagrams for b and c production and includes initial and final state gluon bremsstrahlung. The normalization is determined by comparing ISAJET's $d\sigma/d\eta dP_t^2$ distribution for b and c quarks over the rapidity region $|\eta| < .5$ to a theoretical curve calculated by Nason, Dawson, and Ellis (NDE) [32] which includes next to leading order diagrams. The ISAJET results are renormalized to match the NDE calculation by introducing a "K" factor. The "K" factor used for bottom was $K_{bot} = 1.5$ and for charm was $K_{charm} = 1.7$ [28].

The input muon $d\sigma/dP_t$ distribution for the range $1.9 < |\eta| < 2.7$ is shown in Figure 3.5 for each of the muon components described in the preceding sections.

3.4.4 Detector Effects

The FMU simulations include the interactions of muons with matter in the calorimeters and toroids as well as the toroid magnetic field. Energy losses are modelled by a dE/dx routine in CDFSIM which includes Landau fluctuations. Multiple scattering is included but is complicated by the fact that a correct treatment is unavailable. The Gaussian approximation to multiple scattering drastically underestimates the tails, whereas the Moliere model assumes point-like nuclei for scattering centers and thus overestimates the number of scatters with $E\Delta\theta \geq 100MeV$. We use the Moliere model in the simulations used for this

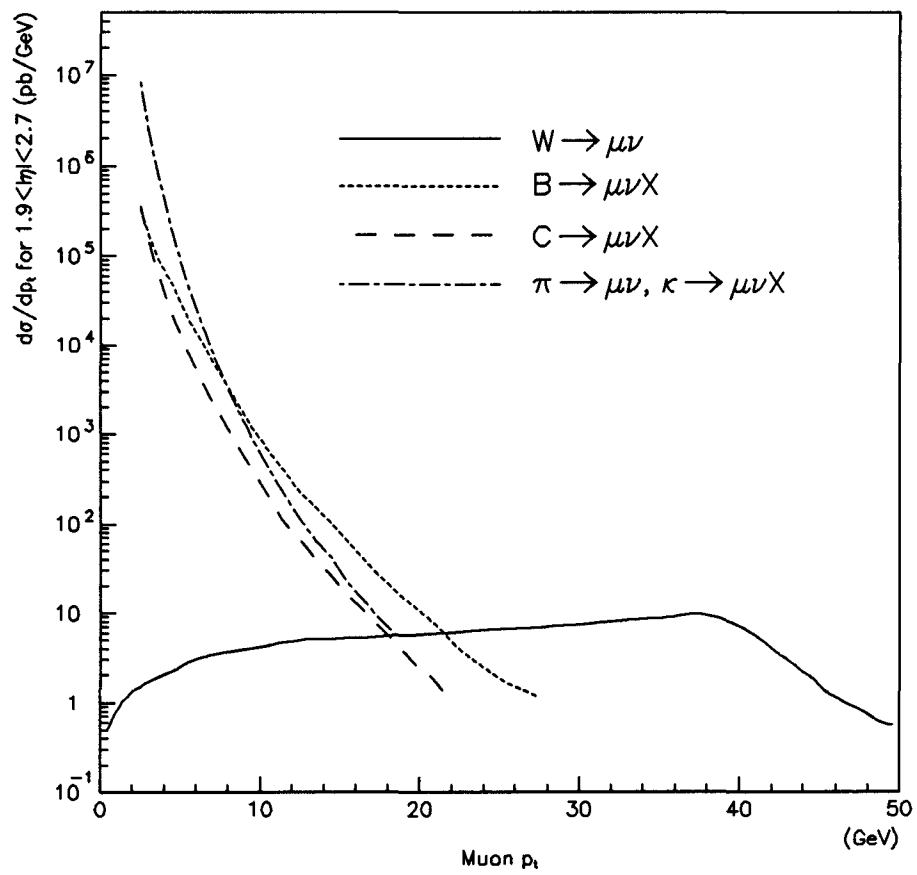


Figure 3.5: $d\sigma/dP_t$ input muon spectrum

analysis.

As the muons pass through the toroid system, extra hits may arise from processes like delta rays and bremsstrahlung interactions. The simulation uses a parameterization of the extra hit multiplicity and spatial distributions obtained from a detailed GEANT simulation [33]. These distributions have been compared to observation and are described elsewhere (Appendix 2, [34]).

Additional detector effects are included as follows. Muon hit positions are smeared by 650 microns which corresponds to the measured chamber resolution for the CDF 1988-89 run. The single-hit chamber efficiency is set at 95%. The electronics cannot resolve two muon hits in the same cell separated by less than 100nsec; the second hit is lost. This 100ns deadtime is included in the simulation. The wire positions are smeared by .05cm in the x-y plane and .2cm in z to account for uncertainties in survey measurements, including the appropriate correlation between coordinate and ambiguity wires in the same chamber. For 10% of the chambers, we double the survey error in order to study the effect of a non-Gaussian tail.

3.4.5 Computer Codes

For the decay in flight backgrounds, a special purpose generator was written. Minimum bias decays were generated from π and K decays, starting with a parameterization of the CDF inclusive charged particle P_{\pm} spectrum [35] together with a flat rapidity distribution.

The detector simulation was implemented separately in CDFSIM and in a stand alone forward muon simulator optimized for speed [24]. Results from CDFSIM and from the fast simulator were checked for consistency, and large statistics samples were then generated using the fast simulator.

The FMU NUPU 50% trigger is fully simulated, tracks are reconstructed with the same tracking module used for the actual data, and the offline selection cuts are applied.

3.5 Comparison of Simulation to Data

3.5.1 East/West and +Q/-Q Asymmetries in the Data.

In comparisons of east detector distributions to west detector distributions, the CDF 1988-89 data show an asymmetry. There are more events on the west side of the detector than on the east side. This asymmetry can be explained by the detector efficiencies listed in Table 2.2. Namely, the overall trigger efficiency for the west side is $45.7 \pm 2.3\%$ while for the east this efficiency is $36.8 \pm 1.9\%$. Table 3.4 lists the ratio for east/west overall efficiencies as well as the ratio for the east/west number of inclusive events. The data ratio is very consistent with the ratio predicted by the efficiency estimates. When the CDF 1988-89 data is corrected for detector efficiencies and trigger efficiencies, the P_t and η distributions of the two detector ends match each other quite well. Figure 3.6 shows the uncorrected and corrected dN/dP_t and $dN/d\eta$ spectrums for the two

East/West Overall	East/West Inclusive
Efficiencies	Data Events
$.805 \pm .058$	$.804 \pm .027$

Table 3.4: Ratio of East/West Values using Efficiencies and Data.

sides of the detector.

The data also show more negatively charged tracks compared to positively charged tracks due to the geometric trigger efficiency. (The trigger efficiency curve was shown in Figure 2.13.) Figure 3.7 shows the ratio of +Q/-Q tracks for monte carlo data compared to the CDF 1988-89 data. Again, the agreement between monte carlo and data is quite good. Thus the charge asymmetry observed in the data is purely geometrical and explained by the trigger requirements.

3.5.2 The dN/dP_t and $dN/d\eta$ Distributions

To compare the data directly to the simulation, the simulated distributions are corrected for data cut and detector efficiencies. The corrected simulated data is then compared to the CDF 1988-89 data in Figures 3.8 through 3.14. The first two plots show distributions of dN/dP_t for each of the simulated sources of muons and their sum. The second two plots show similar distributions for $dN/d\eta$. From these figures, we see the simulated distributions match the data in both general shape and overall normalization. Even though the agreement is rather good, the

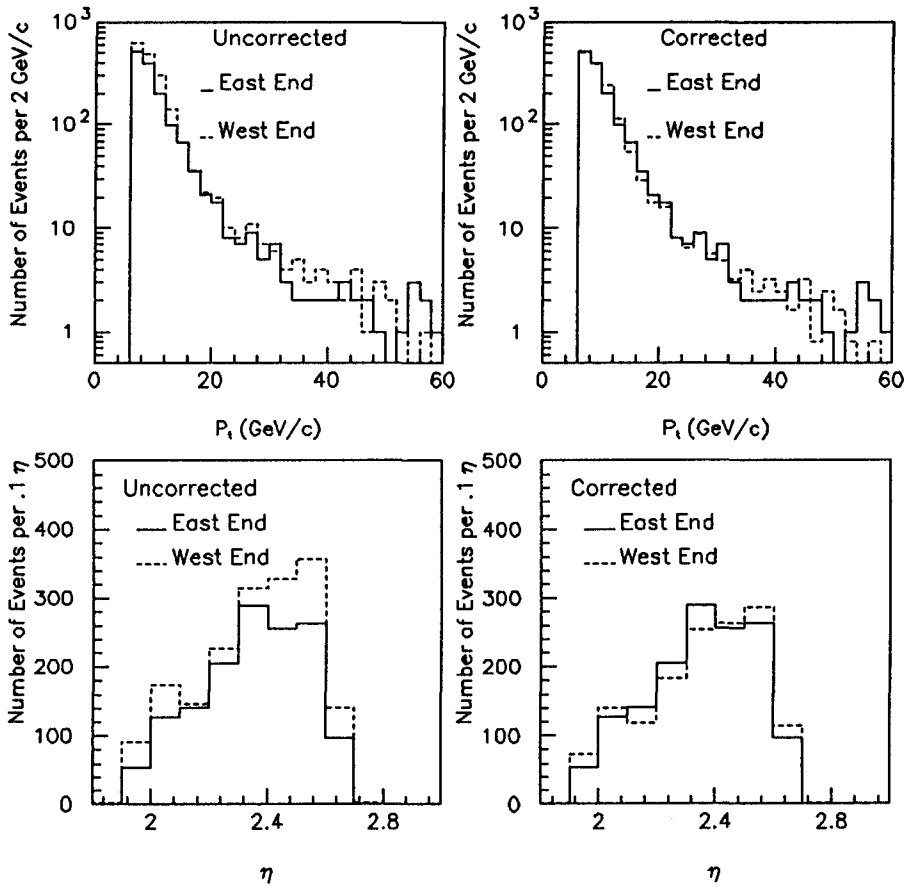


Figure 3.6: P_t and η distributions comparing data yields for the east and west sides of detector. a.) uncorrected P_t b.) corrected P_t c.) uncorrected η d.) corrected η .

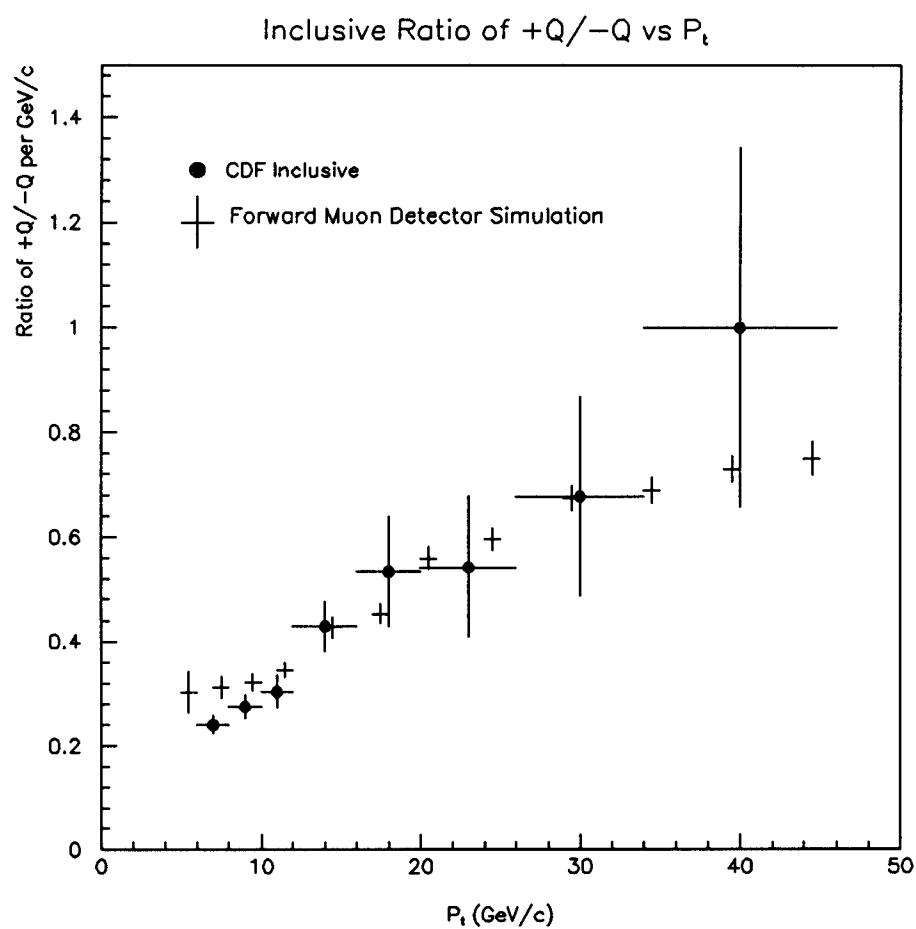


Figure 3.7: Inclusive Ratio of $+Q/-Q$ compared to simulation

following comments concerning the input minimum bias and heavy flavor spectra used in the simulation should be considered.

First, the minimum bias spectrum shape in the forward region has not been measured, but is assumed to be the same as the spectrum shape measured in the central detector. In the central region, CDF has measured the inclusive charged particle P_t spectrum down to very low P_t [35]. There is an uncertainty in the extrapolation of the inclusive π, K spectra to the forward η region. For very low P_t , $dN/d\eta$ is expected to be nearly flat in η . This is supported by the measured constant value of the number of charged tracks per unit of pseudorapidity for the entire interval $|\eta| < 3.0$ [36]. For higher values of P_t , say 10GeV/c or more, $dN/d\eta$ may behave more like the distribution of jets, falling off as $|\eta|$ increases above 2. Thus at fixed $|\eta|=2.$, the spectrum falls even faster with P_t than at $\eta=0$.

Secondly, the extended charged particle spectrum obtained from special stiff track trigger runs taken in the 1988-89 period [37] indicate that the P_t spectrum in the region of $P_t > 10\text{GeV}/c$ falls less rapidly than the CDF published spectrum [35]. Figure 3.12 shows the extended charged particle spectrum. The triggers used the Freeman-Foster track processor to select events with tracks above P_t thresholds 5,8, or 10GeV/c. The data points in Figure 3.12 below 5GeV/c are from the CDF published spectrum[35]. Note that the higher P_t points lie above the curve[35] parameterizing $0 < P_t < 5\text{GeV}/c$.

In the face of these uncertainties we may make two claims for the forward region $2 < |\eta| < 3$. First, the spectrum at low P_t is given by the CDF inclusive

spectrum [35] with errors dominated by the uncertainty in particle composition. Secondly, in the region $10 < P_t < 18 \text{ GeV}/c$, the production yield errors include the uncertainty in spectrum shape as given by the stiff-track results observed in the central region (Figure 3.12), which is characterized by a similar fit with exponent $n=8.0$. Finally, an absolute normalization of the minimum bias spectrum at higher P_t 's ($P_t > 20$) cannot be obtained since it is dominated by simulation uncertainties, but is probably at the level of a factor 1.5-2. This is because of the large rate due to mismeasured multiply scattered soft muons and will be discussed in extensive detail in Chapter 4. In the softer P_t region ($P_t < 18$), the signal of real muons is so much larger that the mismeasurement contribution is negligible.

Finally, one of the main uncertainties in the production yield at low p_t comes from the theoretical uncertainty of the bottom and charm quark cross sections. There are obvious sources for errors in these calculations. The effect of higher orders in the calculation is not completely understood, and it is far from clear that the perturbative series is close to converging. Furthermore, there is the measured cross section from CDF which used electrons in the central calorimeter [38] that indicates the bottom cross section of NDE is smaller than the measured cross section by a factor between 2 and 3. For charm, higher orders are proportionately larger so predictions are a priori even less reliable [28].

In order to show that the data yield is consistent within the range of uncertainty in the simulated processes, the data is compared to the maximum and

minimum uncertainty of the simulated processes in Figures 3.13 and 3.14. The uncertainty band includes the uncertainty in the π/K ratio, the bottom and charm cross sections and the uncertainty in the detector efficiencies and data acceptance cuts. The data show good agreement with our understanding of the FMU spectra.

3.6 Results

In conclusion, For muons selected using the standard cuts, the east/west data yield and charge asymmetry are consistent with the detector and trigger efficiencies. The data yield is consistent with the expected yield and that the shape of the data distributions are consistent with the uncertainty of the soft muon contributions.

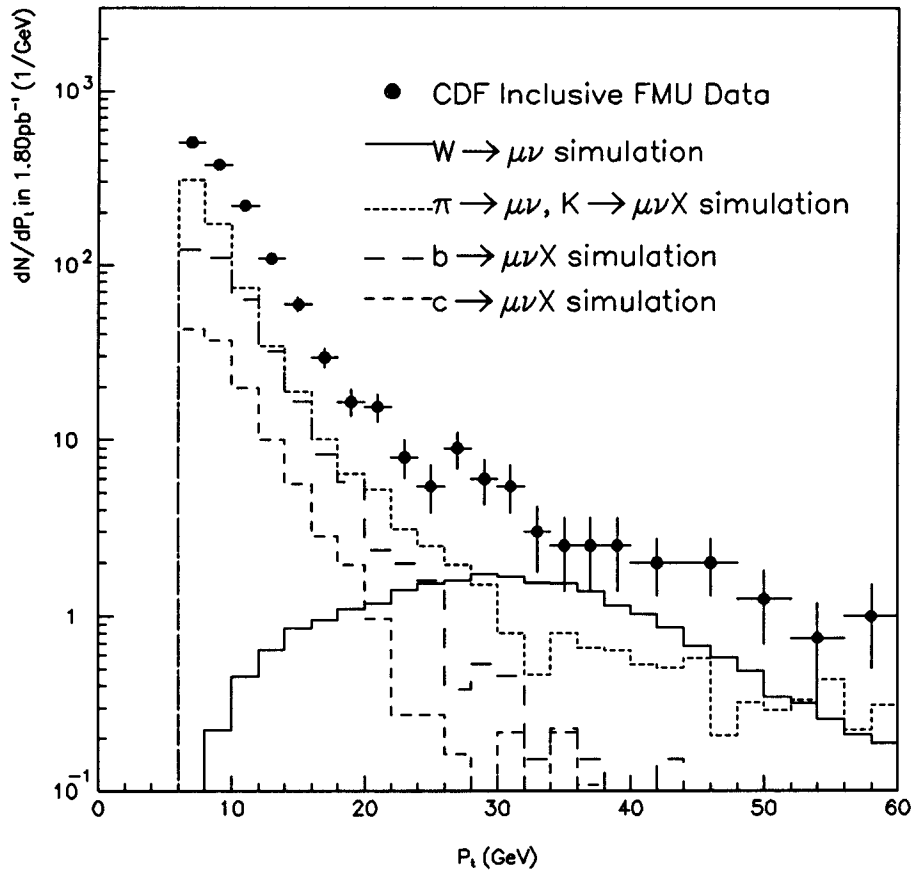


Figure 3.8: dN/dP_t distribution for inclusive forward muons compared to simulated processes.

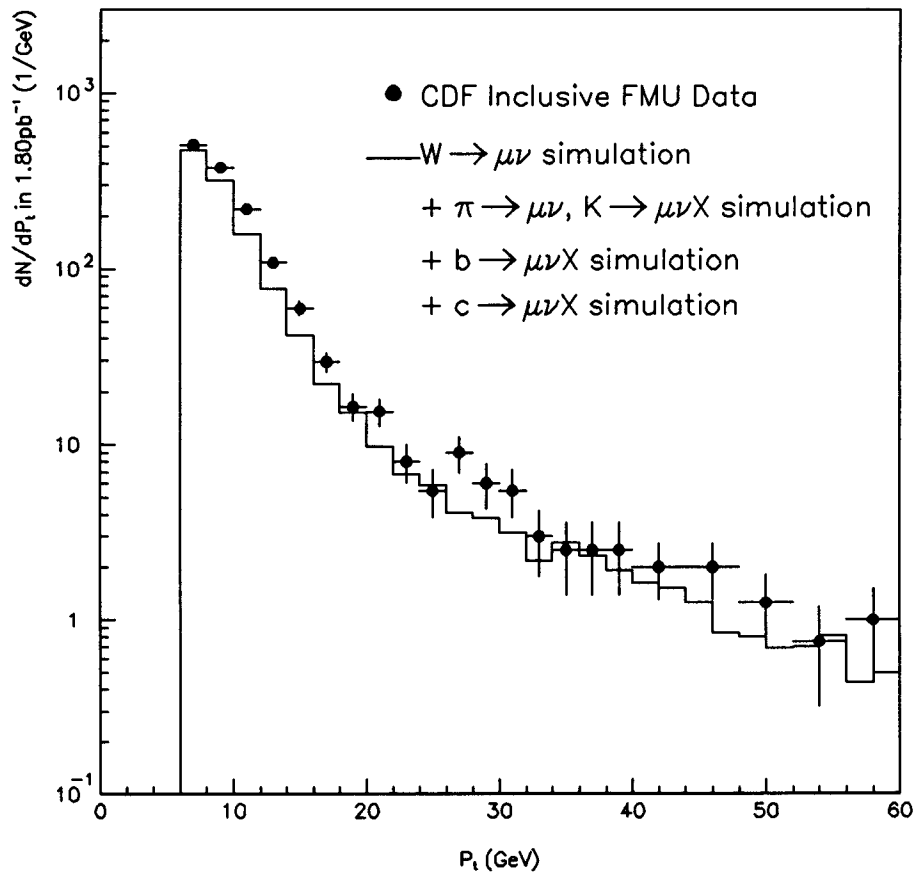


Figure 3.9: dN/P_t distribution for inclusive forward muons compared to the sum of simulated processes.

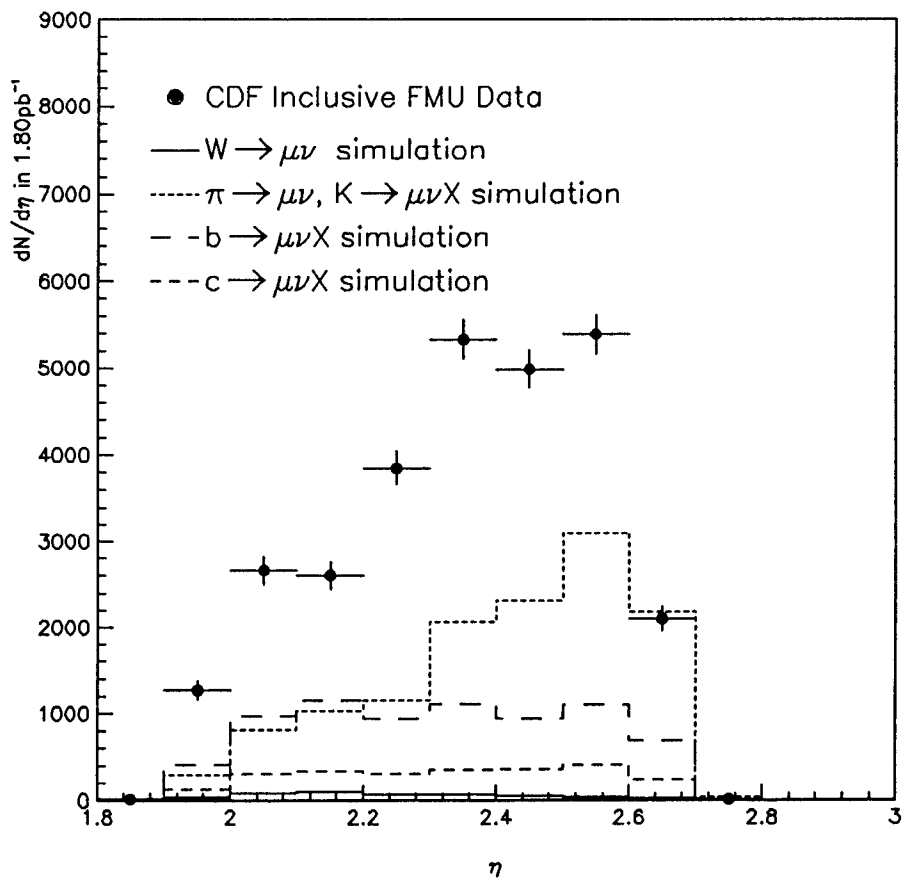


Figure 3.10: $dN/d\eta$ distribution for inclusive forward muons compared to simulated processes.

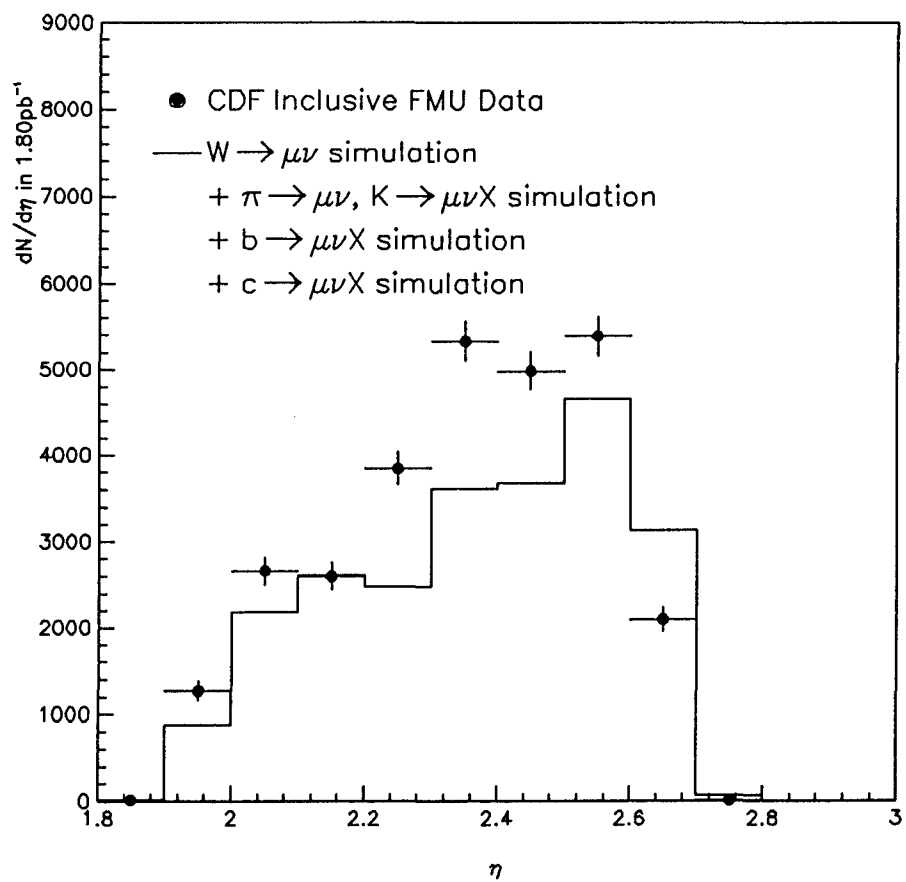


Figure 3.11: $dN/d\eta$ distribution for inclusive forward muons compared to the sum of simulated processes.

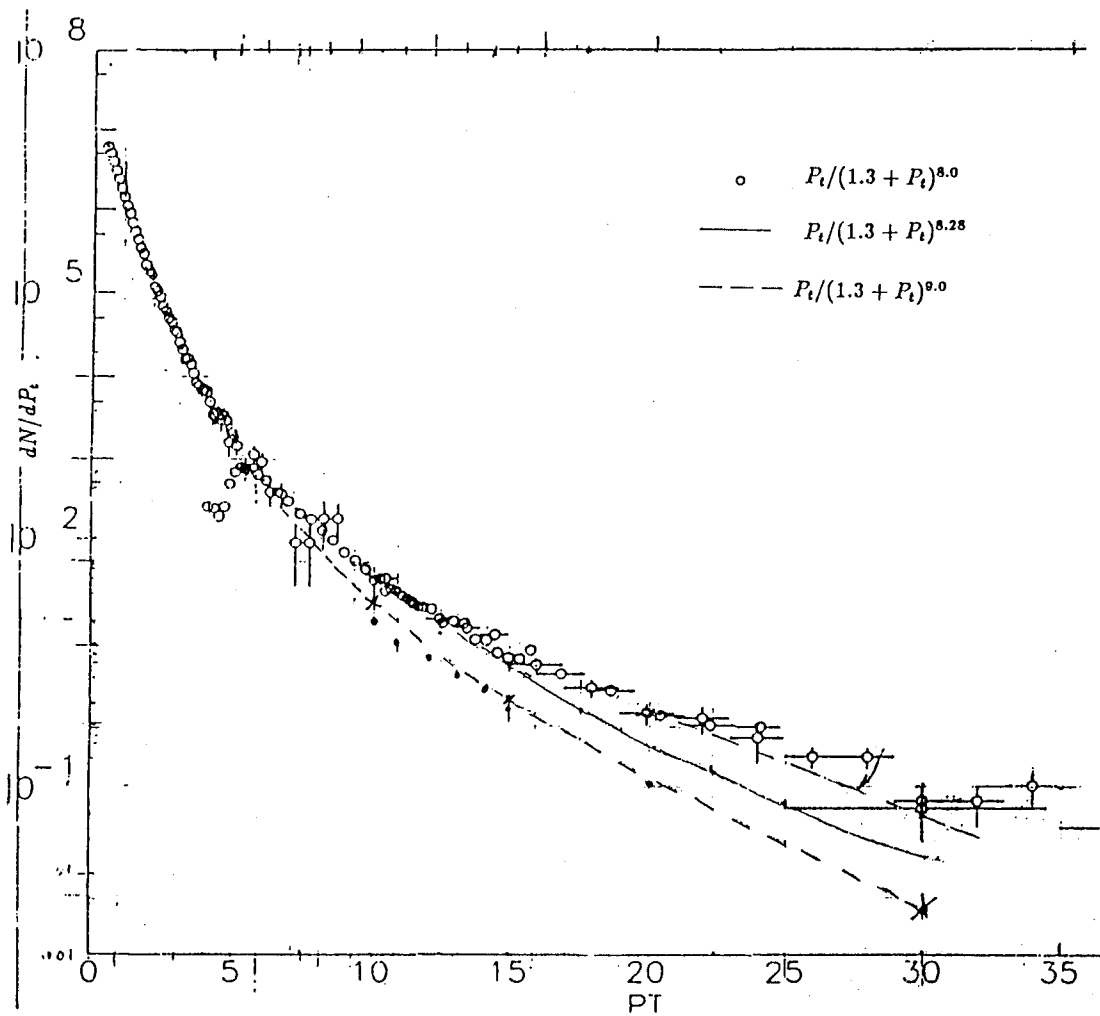


Figure 3.12: dN/dP_t charged particle spectrum obtained from special stiff track trigger runs taken in the 1988-89 period.

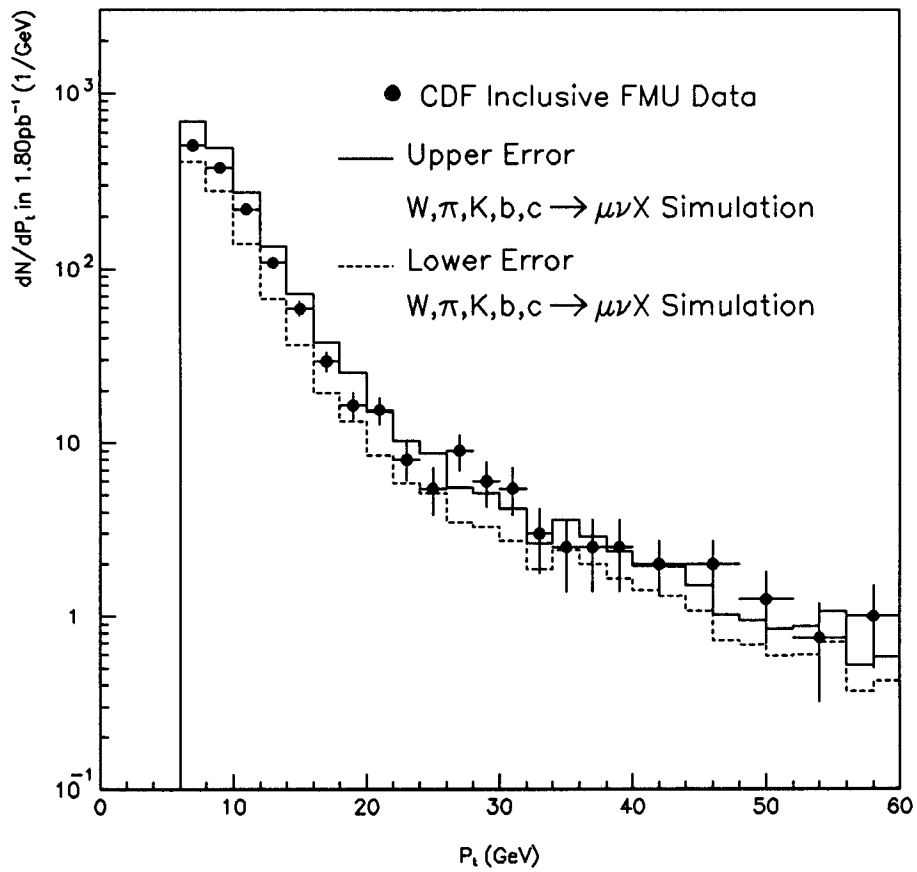


Figure 3.13: dN/dP_t distribution for inclusive forward muons compared to the sum of the simulated processes including the uncertainties.

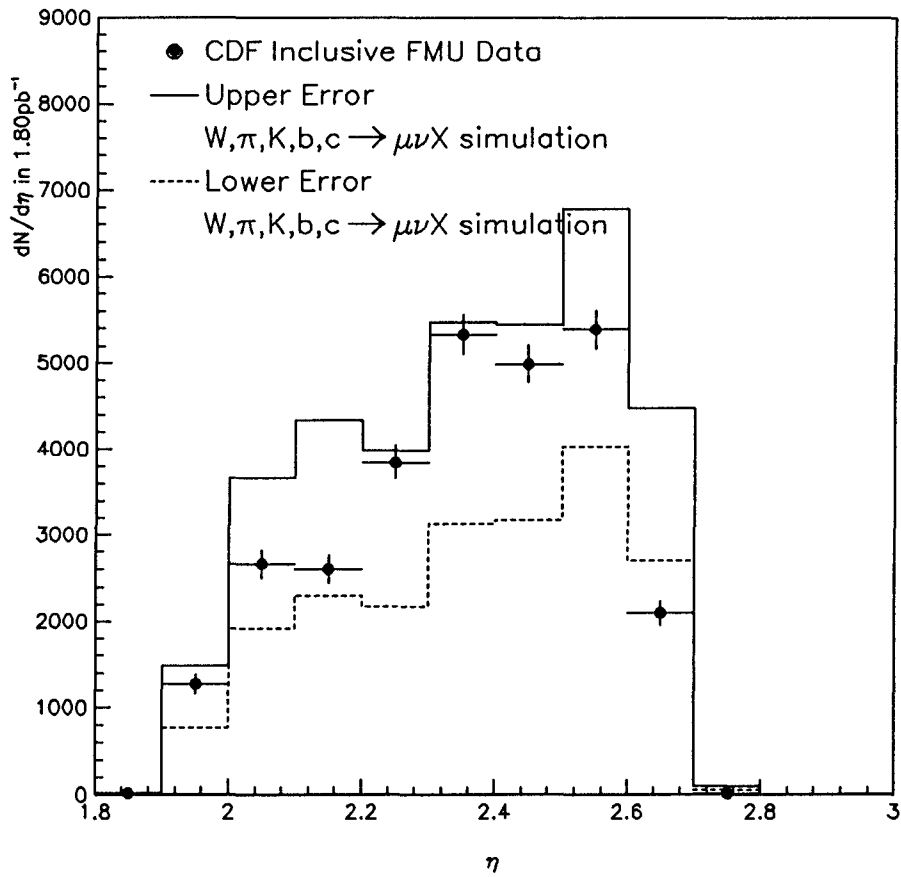


Figure 3.14: Corrected $dN/d\eta$ distribution for inclusive forward muons compared to the sum of the simulated processes including the uncertainties.

Chapter 4

The FMU $W^\pm \rightarrow \mu^\pm \nu$ Spectrum

4.1 Introduction

In this chapter, I study the high P_t forward muon signal. I estimate the number of W candidates in this signal as well as the other background components.

4.2 W Data Selection

The W forward muon data set consists of forward muon events which were selected from the MUO04 data stream using the standard cuts described in Chapter 3 with the exclusion of the $P(\chi^2)$ cut.

Since the characteristic signature of a W decay is a high P_t isolated lepton, the W decay muons are also required to pass the cuts:

- The transverse energy observed within an 11x11 array of calorimeter towers centered on the muon (similar to a cone in $\eta - \phi$ space of radius $R=.55$),

must be less than 5 GeV.

- The muon's transverse momentum satisfies $22 < P_t < 75\text{GeV}/c$.

Additional cuts on the fit χ^2 and on pseudorapidity are used in the final analysis. These cuts are discussed extensively in Section 5. The final sample requires $P(\chi^2) > .02$ and $|\eta| < 2.4$.

4.2.1 The Isolation Cut.

In the η region $1.9 < |\eta| < 3.0$, isolation is determined by the calorimetry. More specifically, we define an isolated muon in terms of the transverse energy observed in the calorimetry in a cone of $R=.55$ surrounding the muon, $E_t(R = .55)$. For this analysis, isolated muons must satisfy $E_t(R = .55) < 5\text{GeV}/c$. This value was determined using the FMU-CMU Z^0 candidates. The forward muon $E_t(R = .55)$ distribution for the Z^0 events is shown in Figure 4.1. From this figure, we see a value of $E_t(R = .55) < 5\text{GeV}/c$ is quite reasonable. This cut was found to be 95% efficient at selecting FMU-CMU Z^0 events.

4.3 Backgrounds

The largest background to W production in the forward region is from low P_t pion and kaon decay muons which are mismeasured as high P_t muons. This occurs in two ways. First, there is a small probability that a low P_t muon will undergo multiple scattering in such a way as to fake a high P_t track. Second,

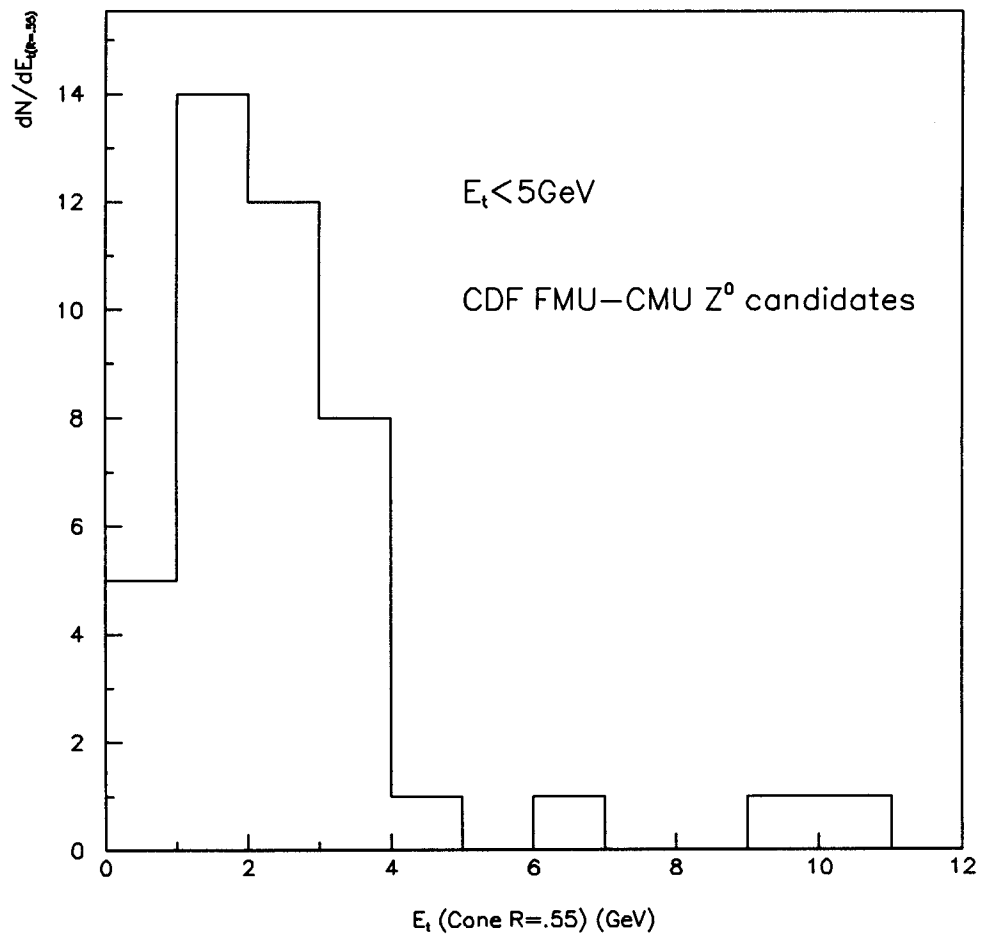


Figure 4.1: Distribution of E_t in a cone of $R = .55$ for FMU-CMU Z^0 candidates.

delta ray electrons accompanying a muon can cause an ambiguity in the muon hit position. Both processes are unlikely for a given muon, but they become significant due to the abundance of low P_t muons. The second largest background is from $Z \rightarrow \mu\mu$ where one muon hits the forward muon chambers and the second muon is undetected. Other backgrounds are negligible compared to the expected W signal. In this chapter, these backgrounds are determined quantitatively.

4.4 The Simulated Isolated Decay-in-flight Spectrum

As mentioned in Chapter 3, there are several uncertainties in extrapolating the charged particle spectrum to the forward region. (The uncertainty in the charged particle spectrum composition and shape were discussed earlier.) For the isolated spectrum, we introduce an additional uncertainty in the spectrum shape once the isolation requirement is used. This is important since an isolation cut will reduce the contribution from high P_t tracks which are more often in jets. To study this, the same stiff-track trigger events (used for analysis of the inclusive muon spectrum in Chapter 3 Section 5.2) were used. The stiff-track trigger events were subjected to a cut on energy contained in nearby tracks. A track was called "isolated" if no other tracks with $P_t > 3\text{GeV}/c$ pointed to a 5×5 array of calorimeter towers centered on the track in question, and if at most two tracks with $P_t < 3\text{GeV}/c$ pointed to this array. The resulting inclusive isolated track spectrum falls more rapidly than the parameterization obtained from Ref[35], effectively changing the exponent parameter from $n=8.28$ to $n=9.0$ (This is also shown in Figure 3.12).

The slope may depart somewhat from $n=9.0$ if the isolation criterion is defined differently, as it is for the forward muon sample.

In the face of the simulation uncertainties in the decay in flight spectrum, (the particle composition uncertainty, the power spectrum for the isolated distribution and the η dependence), we may make two claims for the forward region $2 < |\eta| < 3$. First, the spectrum at low P_t is given by the CDF inclusive spectrum [35]. Secondly, an upper limit on the spectrum for $P_t > 10\text{GeV}/c$ is given by the isolated inclusive spectrum observed in the central region (Figure 3.12), which is characterized by a similar fit with exponent $n=9.0$. The true spectrum in this region is lower by some amount which we decline to estimate.

The decay-in-flight spectrum was studied using the fast simulator which was able to simulate millions of low P_t decay-in-flight muons, down to $P_t > 2\text{GeV}/c$. Even so, there were yet more decay in flight muons (3×10^8 in the 1988-89 run) with $1 < P_t < 2\text{GeV}/c$ which could not be properly simulated with the limited CPU power available. Although unfortunate, this fact will not prevent us from estimating their contribution quantitatively.

4.5 High P_t decay-in-flight Muons.

The background to the W signal from high P_t decay-in-flight muons is estimated directly from an assumed spectrum shape combined with detector effects (Chapter 3, Section 4). The isolated spectrum measured in the central region is used, and the Moliere scattering model is chosen. Both of these choices will lead to

overestimates of the background, so that the result is only an upper limit. The ratio $\frac{N_{mbs}}{(N_{mbs}+N_W)}$ is shown in Table 4.1 where N_{mbs} is the expected number of simulated minimum bias events and N_W is the expected number of simulated W events. From this table, we see the expected minimum bias background contribution is very small. If the inclusive spectrum without the isolation cut is used, the limit grows by a factor 2.

Source	$\frac{N_{mbs}}{(N_{mbs}+N_W)}$ $22 < P_t^{fit} < 75 \frac{GeV}{c}$	$\frac{N_{mbs}}{(N_{mbs}+N_W)}$ $22 < P_t^{fit} < 75 \frac{GeV}{c}$ and $P(\chi^2) > .02$	$\frac{N_{mbs}}{(N_{mbs}+N_W)}$ $22 < P_t^{fit} < 75 \frac{GeV}{c}$ and $P(\chi^2) > .02$ and $ \eta < 2.4$
Isolated μ 's $P_t > 10 \frac{GeV}{c}$.049 \pm .002	.038 \pm .002	.021 \pm .002
Inclusive μ 's $P_t > 10 \frac{GeV}{c}$.089 \pm .004	.073 \pm .004	.042 \pm .003

Table 4.1: Upper limit on background from decay-in-flight muons with $P_t > 10 \text{ GeV}/c$, in the W signal region. The additional cuts on $P(\chi^2)$ and $|\eta|$ are discussed in section 5.

4.6 Low P_t decay-in-flight Muons.

4.6.1 Enrichment Cuts

Given the small background estimated from decay-in-flight muons with $P_t > 10 \frac{\text{GeV}}{c}$, it is not initially obvious that decay-in-flight muons should be a significant background for W decays in the forward region. However, there are a large number of very soft muons, $P_t < 10 \text{GeV}/c$, and at $\eta=2.4$ a mere $900 \text{MeV}/c$ (P_t) muon can penetrate the calorimeters and the toroid steel. Therefore a simulation of this contribution is warranted.

The results of a simulation of low P_t decay-in-flight muons are shown in Figures 4.2 and 4.3, compared to the prediction for W events and to the CDF data. The P_t^{fit} and η distributions are shown only for those events which are measured to be in the W signal region $22 < P_t^{fit} < 75 \text{GeV}/c$. The simulation uses the Moliere scattering model as well as the other effects like extra hits (Chapter 3, section 4). The survey uncertainties have been included in the W simulation and the decay in flight simulation starts with the expected muon spectrum for $P_t > 2 \text{GeV}/c$. The predictions are normalized to the integrated luminosity of the CDF data. According to these figures, not only is the rate from decay-in-flight predicted to be large, but the data show strong evidence of such a contribution in both P_t and η distributions. For example the large number of events at high η is characteristic of decay-in-flight muons, which have a flight path three times longer for $|\eta| > 2.4$ than for $|\eta| < 2.4$.

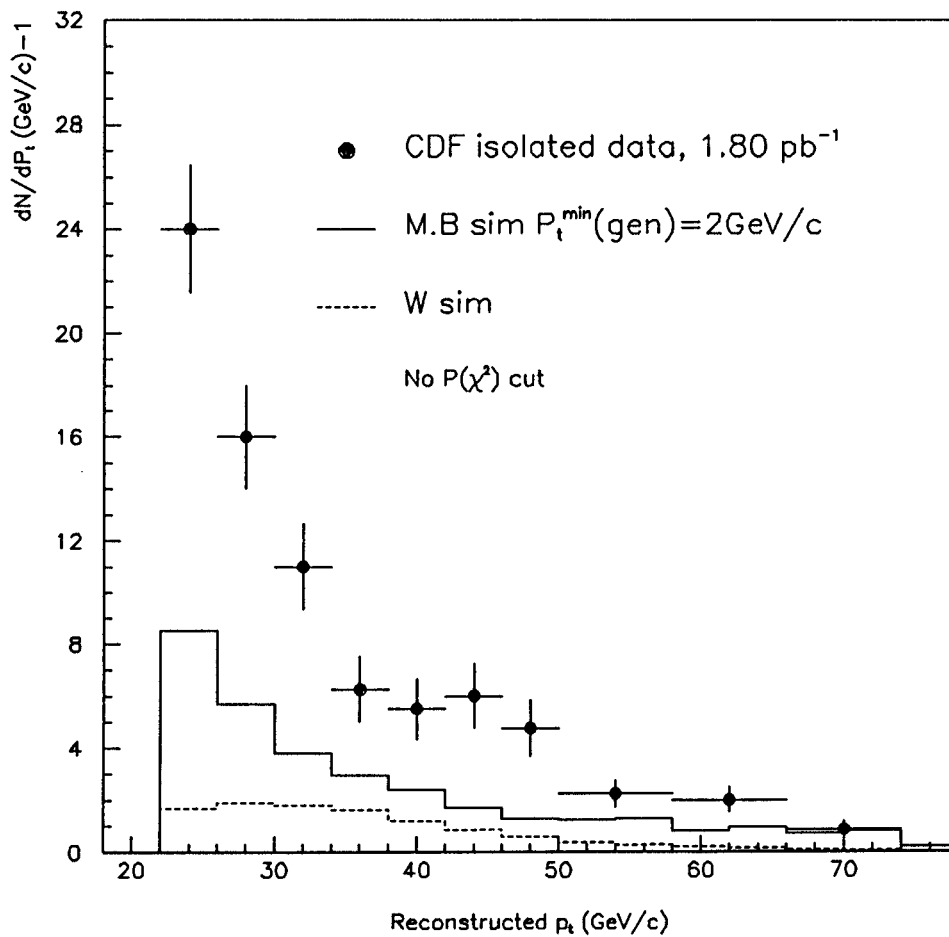


Figure 4.2: Distribution of reconstructed P_t for a simulation of low P_t decay-in-flight muons compared to the prediction for W events and to the CDF 1988-89 data. A minimum muon P_t of 2 GeV/c is used.

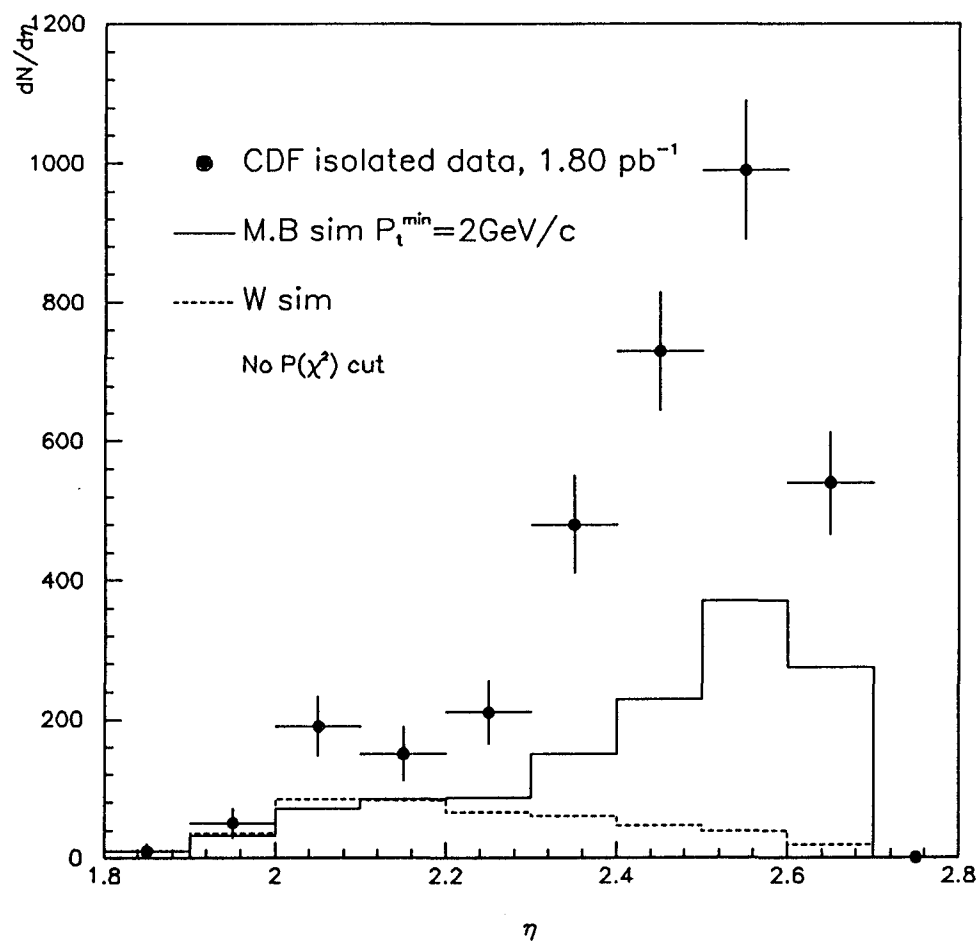


Figure 4.3: Distribution of pseudorapidity for a simulation of low P_t decay-in-flight muons compared to the prediction for W events and to the CDF 1988-89 data. A minimum muon P_t of $2\text{GeV}/c$ is used.

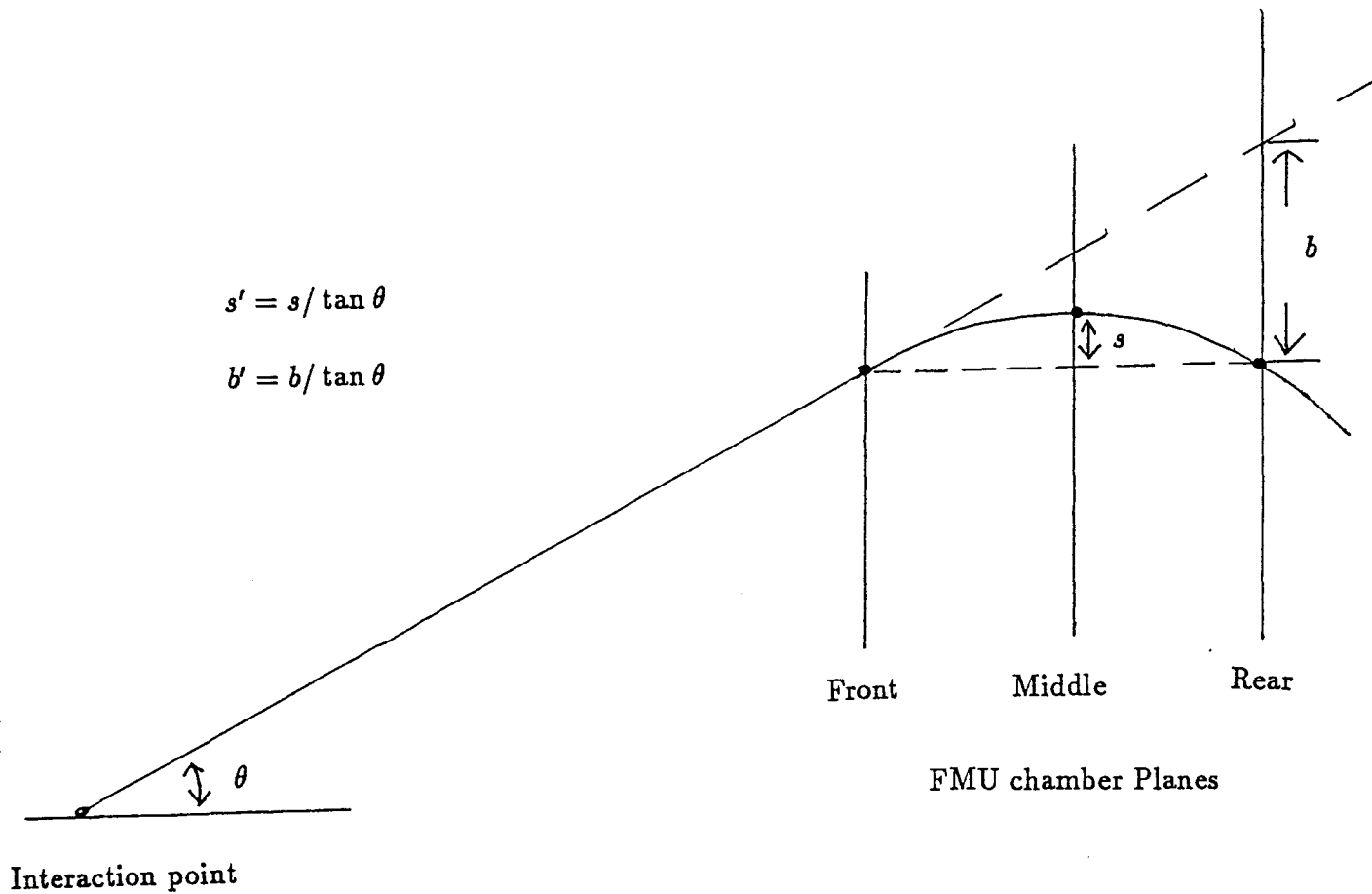
To understand heuristically how a low P_t track could be mismeasured as high P_t , we may observe that the FMU momentum determination relies mostly on the curvature observed between the front, middle and rear chamber planes. Figure 4.4 illustrates the path a particle takes through the detector showing the measured bend and sagitta which are used in determining the measured track P_t . (We imagine each coordinate-ambiguity hit pair to constitute one measurement.) If a track appears straight based on these three points, then it will usually be assigned a high momentum. The event vertex constraint plays only a minor role in this, because of the large amount of material in the calorimeters. Starting with a low P_t track with large curvature then, a single instance of large angle scattering can in principle yield a fairly straight track along the three points, resulting in a high P_t after fitting. The hit confusion due to delta rays adds to the mismeasurement probability.

However such faked straight tracks will generally not point back to the event vertex, as would a true high P_t track. This situation results in a poor overall fit when the event vertex constraint is used, so that a cut on the fit χ^2 should remove most of this background. Figure 4.5 shows the predicted distribution of χ^2 for tracks with $22 < P_t^{fit} < 75$, as measured by the probability integral

$$P(\chi^2) = \int_{\chi^2}^{\infty} d\chi^2 f(\chi^2) \quad (4.1)$$

where $f(\chi^2)$ is the theoretical χ^2 distribution which follows from Gaussian statistics. For the W events (figure 4.5a), $P(\chi^2)$ is expected to be almost flat over the

Figure 4.4: Schematic of bend and sagitta definitions.



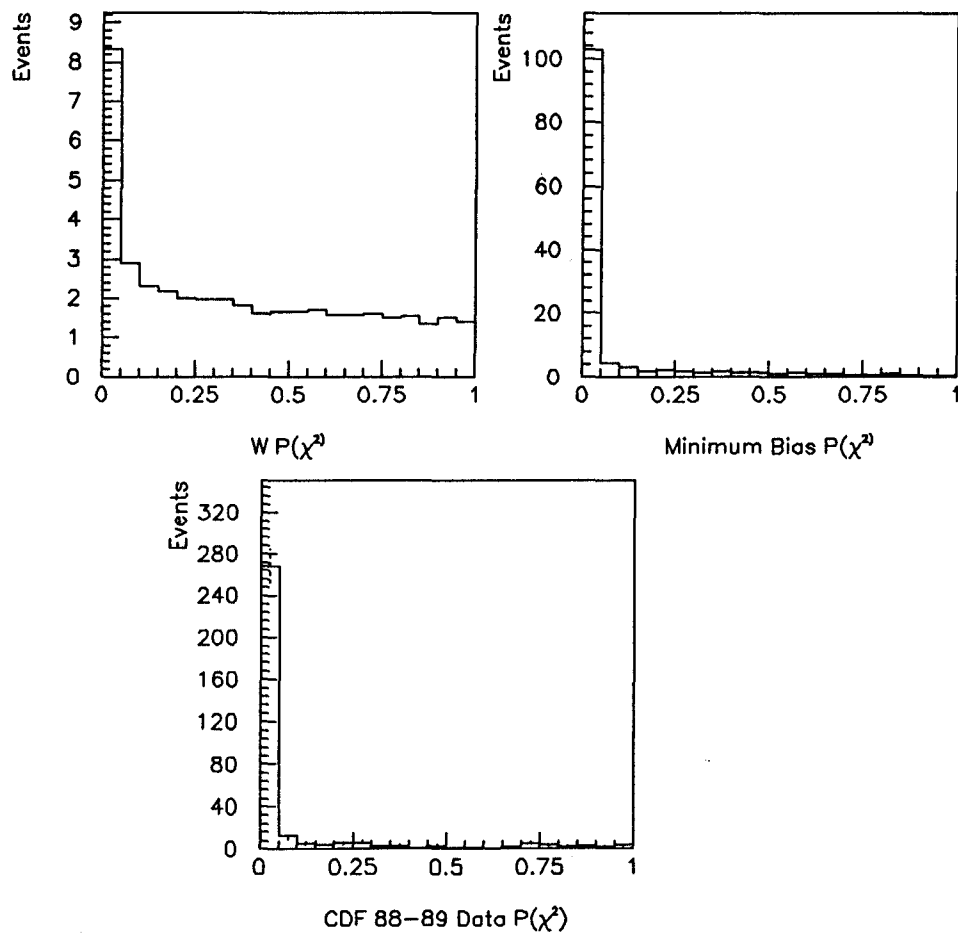


Figure 4.5: $P(\chi^2)$ distribution for low P_t decay-in-flight simulation, a.) W simulation. b.) minimum bias simulation. c.) CDF 88-89 data.

entire range $0 < P(\chi^2) < 1$. This would also hold for any background muons which are truly high P_t . The low $P(\chi^2)$ enhancement is due to such non-gaussian errors as extra hits, survey errors, the 100ns deadtime, and chamber efficiency. In contrast, the distribution for mismeasured low P_t muons (figure 4.5b) shows a large peak at low $P(\chi^2)$, corresponding to very large χ^2 . Figure 4.5c shows that the CDF data are dominated by this same feature.

After making a cut $P(\chi^2) > .02$, a large portion of the background is removed. The resulting P_t^{fit} and η distributions in the CDF data are shown in Figures 4.6 and 4.7. The W signal is finally discernable above the background in the $dN/d\eta$ figure for the region $1.9 < |\eta| < 2.4$, i.e., $10^\circ < \theta < 16^\circ$ where θ is the polar angle. Thus for the final W sample, we use only the enriched region:

$$P(\chi^2) > .02 \tag{4.2}$$

$$1.9 < |\eta| < 2.4 \tag{4.3}$$

The remaining mismeasurement background may be thought of as events where several large scatters or hit confusions occur, so that the event vertex lines up with the projection of the FMU hits. In these cases, the track reconstruction gives a high P_t^{fit} and good χ^2 , so that they look in every way like true high P_t muons.

Admittedly the predicted normalization of the low P_t decay-in-flight contribution and its apparent agreement with the CDF data should be approached with some caution. After all, very rare processes are being simulated. In addition,

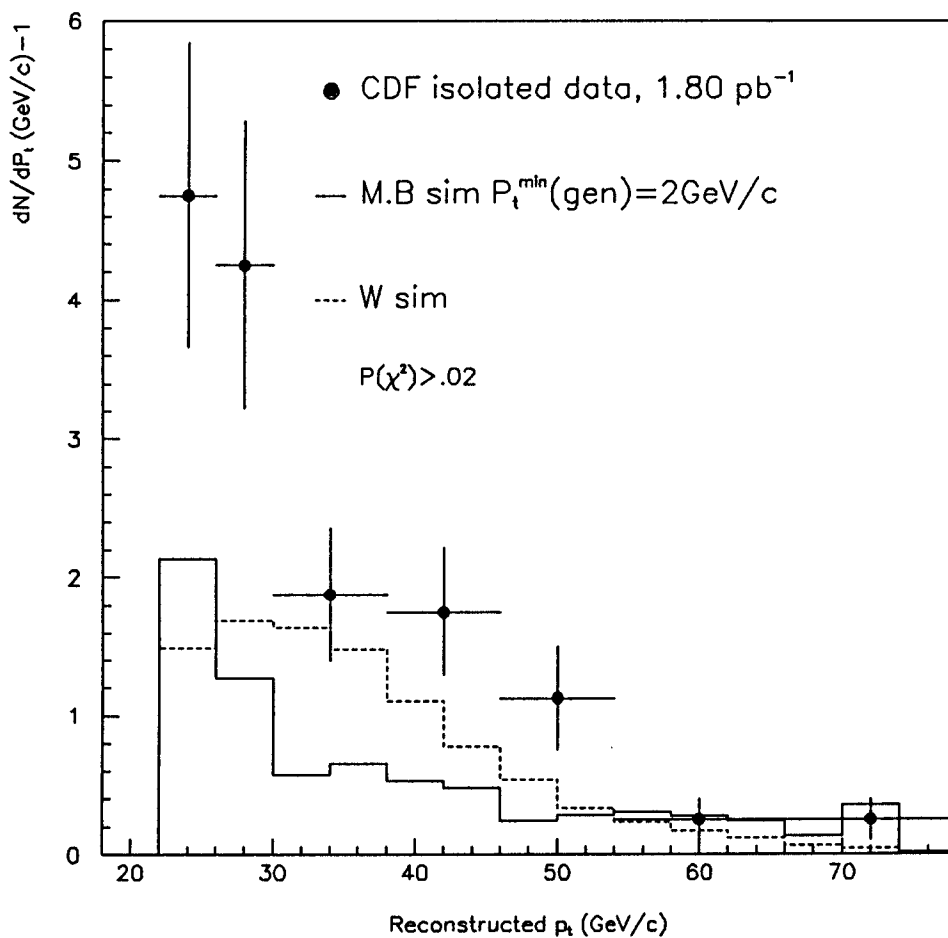


Figure 4.6: Distribution of reconstructed P_t for a simulated low P_t decay-in-flight muons compared to prediction for W events and to the CDF 1988-89 data, for muons satisfying $P(\chi^2) > .02$. A minimum muon P_t of 2GeV/c is used in the decay-in-flight simulation.

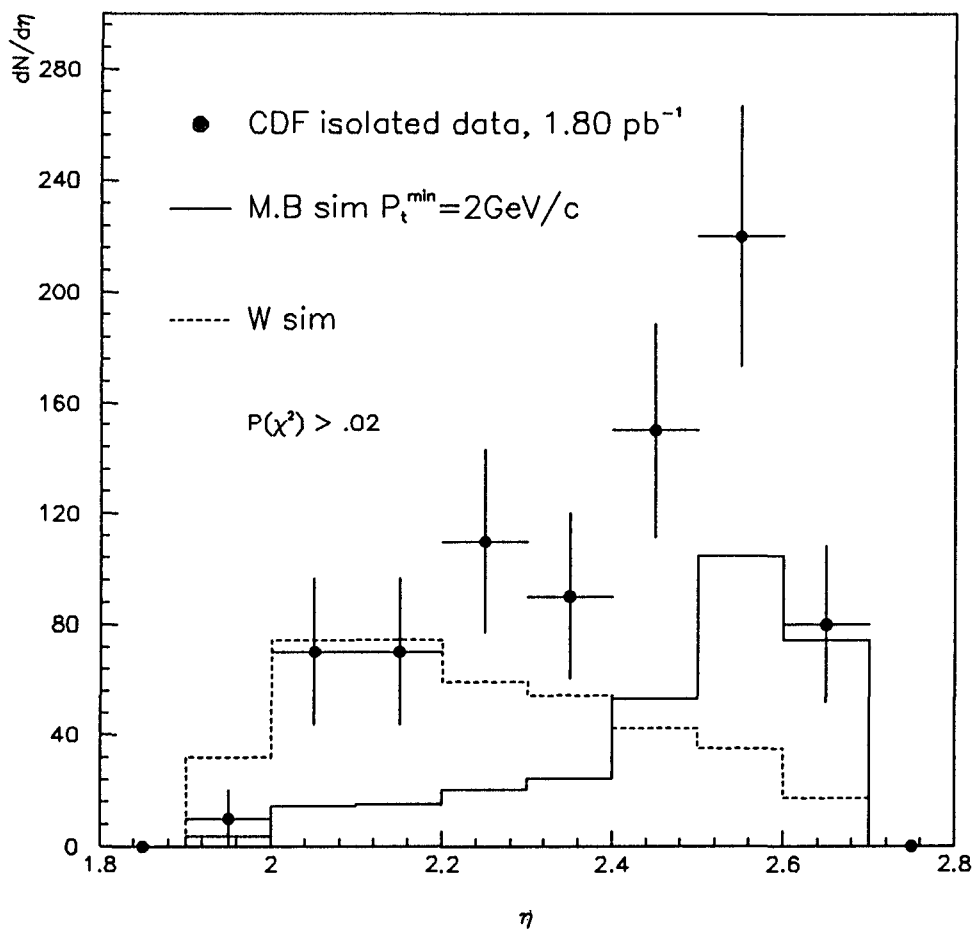


Figure 4.7: Distribution of pseudorapidity for simulated low P_t decay-in-flight muons compared to the prediction for W events and to the CDF 1988-89 data, for muons which satisfy $P(\chi^2) > .02$. A minimum muon P_t of $2\text{GeV}/c$ is used in the decay-in-flight simulation.

muons with $P_t < 2\text{GeV}/c$ were omitted from the simulation. Nevertheless the reality of mismeasured decay-in-flight muons is strongly supported by the excess of events at low P_t and by the appearance of the poor χ^2 tail in the CDF data together with the η distribution.

4.6.2 Fitting for the Background Fraction.

In order to fit the data shown in Figures 4.6 and 4.7 in terms of a linear combination of the two expected components, i.e. the W signal plus decay-in-flight background, we split the data into four bins. The fit signal region is temporarily enlarged to $18 < P_t^{fit} < 75\text{GeV}/c$ to reduce the statistical uncertainty. In addition, a fifth data bin which consists of the total number of events is used. In P_t (Figure 4.6) the plot is divided at $P_t=26\text{GeV}/c$, while in η (Figure 4.7) the division is made at $\eta=2.4$. This procedure produces the numbers listed in Table 4.2.

Each data number is expressed in terms of the two components as follows

$$D_i = aW_i + b(MBS)_i \quad (4.4)$$

where a and b are the multipliers to be determined, D_i are the number of data events, W_i are the number of simulated W events and $(MBS)_i$ are the number of simulated decay-in-flight events.

We perform a least squares fit to determine the fit multipliers a and b using two of the data bins from Table 4.2 plus the data bin consisting of the total

Number of Events in Signal Region of $1.9 < \eta < 2.8$ and $18 < P_t < 75$				
	All η		All P_t	
	$\eta < 2.4$	$\eta > 2.4$	$P_t < 26\text{GeV}/c$	$P_t > 26\text{GeV}/c$
Data	49	62	51	60
MBS Simulation	13.4 ± 1.0	34.9 ± 1.6	26.4 ± 2.0	22.1 ± 2.0
W Simulation	30.7 ± 3	10.1 ± 2	11.1 ± 2	29.7 ± 3

Table 4.2: Breakdown of event counts in two regions of P_t and two regions of η , used to fit for signal and background components in the data.

number of events. We only use two of the data bins in Table 4.2 because of the correlation in both the P_t and η bins with the total number of events. We choose as the two data bins the numbers for $\eta < 2.4$ and $P_t < 26\text{GeV}/c$. The total number of data events is 111 for both the P_t and η distributions. The least squares fit is determined by solving

$$\chi^2 = \sum_i \frac{(D_i - aW_i - b(MBS)_i)^2}{\sigma_i^2}$$

where i denotes the three bins, the total number of events, the number of events with $P_t < 26\text{GeV}/c$ and the number of events with $\eta < 2.4$. σ_i is the statistical error of the data for bin i . χ^2 then has the form

$$\chi^2 = \frac{(111 - 40.8a - 48.3b)^2}{111} + \frac{(49 - 30.7a - 13.4b)^2}{49} + \frac{(51 - 11.1a - 26.4b)^2}{51} \quad (4.5)$$

This gives the results

$$a = 0.93 \pm 0.16 \quad (4.6)$$

$$b = 1.52 \pm 0.17 \quad (4.7)$$

$$\chi^2(a, b) = .007 \quad (4.8)$$

for a and b satisfying $\frac{d\chi^2}{da}=0$, $\frac{d\chi^2}{db}=0$.

Here the number of background events must be increased over the calculated number as determined from the simulation. This is not surprising and is attributed to the unknown contribution from mismeasured muons with $P_t < 2\text{GeV}/c$ not included in the simulation. The χ^2 is very good, indicating an adequate description of the data in terms of the simulated P_t and η shapes.

The final estimate for the decay-in-flight background fraction for the W signal region of $22 < P_t < 75\text{GeV}/c$, $\eta < 2.4$ and $P(\chi^2) > .02$ is found to be $.32 \pm .06 \pm .04$ where $.06$ is the statistical error of the data and $.04$ is the systematic uncertainty and where the background fraction is described by $f = \frac{N_{mba}}{N_W + N_{mba}}$. These numbers are listed in Table 4.3.

4.6.3 Uncertainties in the fitted background fraction

The systematic uncertainties in the fitted background fraction are listed in Table 4.4. The largest uncertainty is statistical, mainly in the data, but also in the simulation. Other systematic uncertainties in the fraction include the effect of the survey errors and the effect of high P_t decay-in-flight muons due the uncertainty

Final Corrected Number of Events in Signal Region of $1.9 < \eta < 2.4, 22 < P_t < 75$ and $P(\chi^2) > .02$	
MBS Simulation	11.91 ± 1.73
W Simulation	25.23 ± 4.35
CDF 1988-89 Data	34 ± 5.92
$N_{mbs}/(N_{mbs} + N_W)$	
background fraction	$.32 \pm .06 \pm .04$

Table 4.3: Final Number of decay-in-flight muons and W muons as determined from the least squares fit. The number of CDF 1988-89 data events is also listed.

in the power spectrum.

Systematic Errors on the Background Fraction	
Statistics of Data	$\pm .06$
Survey Errors	$\pm .03$
Isolated Spectrum Shape	$\pm .02$
Statistics of M.B and W Simulation	$\pm .02$
Overall Systematic Error	$\pm .07$

Table 4.4: Systematic Uncertainty on Minimum Bias Background in FMU region $22 < P_t < 75$, $|\eta| < 2.4$ and $P(\chi^2) > .02$.

4.6.4 Cross-Checks on our Background Estimate

There are a number of cross checks which lend confidence to our background estimate. Simply put, the $P(\chi^2)$, P_t and η distributions are consistent with predictions outside as well as inside the W signal region.

Figure 4.8 shows the $P(\chi^2)$ distribution for simulated minimum bias and W events in the fitted region of $22 < P_t < 75$, $|\eta| < 2.4$ and $P(\chi^2) > .02$ once each contribution has been scaled by the final fit multiplier. The data are also shown. The agreement is very good.

The simulated P_t distribution is shown in Figure 4.9 for decay-in-flight and W decay muons passing selection cuts in the signal region of $|\eta| < 2.4$ and for the

extended P_t range $18 < P_t < 100 \text{ GeV}/c$. The decay-in-flight and W distributions have been multiplied by the fit coefficients. The data are also plotted in this figure for comparison. As shown in this plot, the data match the simulation fairly well both below and above the P_t signal range of $22 < P_t < 75 \text{ GeV}/c$.

The η distribution is shown in Figure 4.10 for the data compared to the sum of simulated signal and background components scaled by the fit multipliers. Again the agreement is very good in both η regions.

Another useful cross check is the number of events with $P_t > 75 \text{ GeV}/c$, $1.9 < |\eta| < 2.4$. In principle this data set could be used as an independent background normalization technique, however the statistics are limited. The number of data events falling in this P_t and η region are listed in Table 4.5. Also listed are the number of decay-in-flight and W events. The data are consistent with expectations, within the statistical uncertainty.

4.7 $Z \rightarrow \mu\mu$

The largest prompt muon background to the W signal is from $Z^0 \rightarrow \mu\mu$ events where one muon hits the forward chambers and the other muon is unobserved. This rate is estimated from a Monte Carlo simulation of $Z^0 \rightarrow \mu^+\mu^-$ events generated using ISAJET and then detector simulated using the either CDFSIM or the fast monte carlo. An absolute normalization which includes both the detector and cut efficiencies as described in Chapter 3 is used to determine the number of Z^0 background events. The first cross check in using this method concerns the

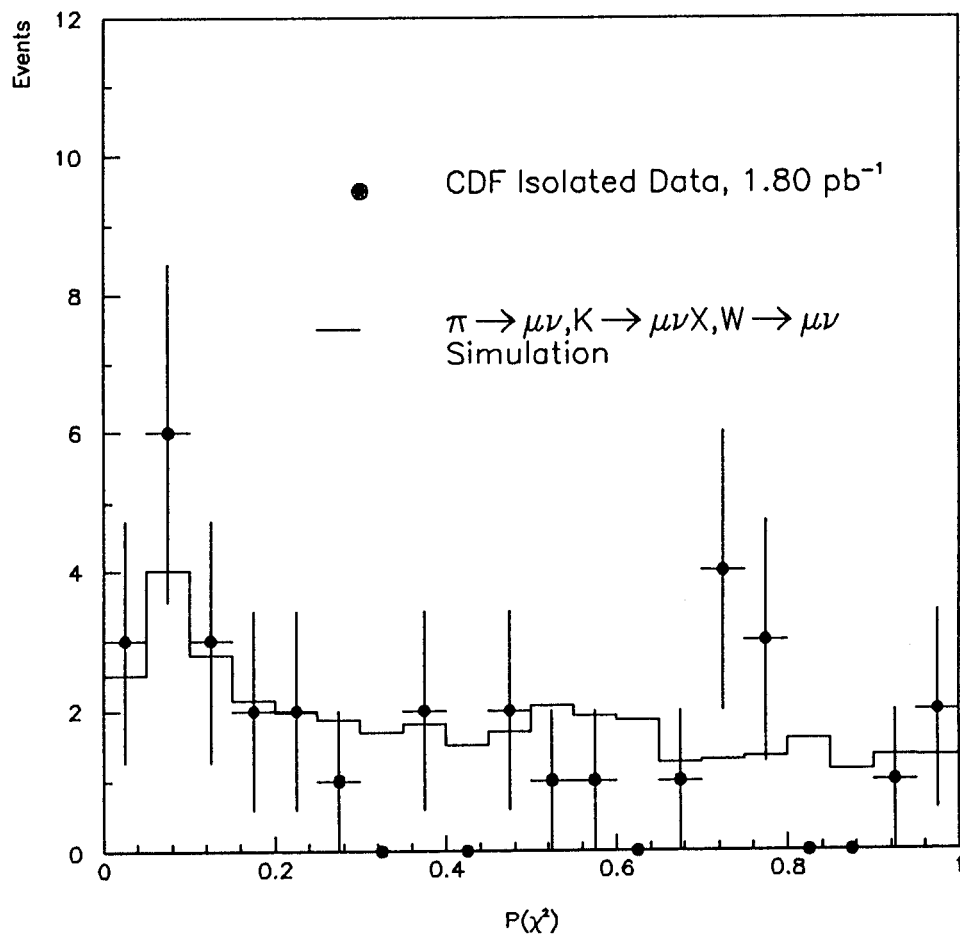


Figure 4.8: $P(\chi^2)$ for muons with $22 < P_t < 75 \text{ GeV}/c$, $|\eta| < 2.4$ and $P(\chi^2) > .02$.

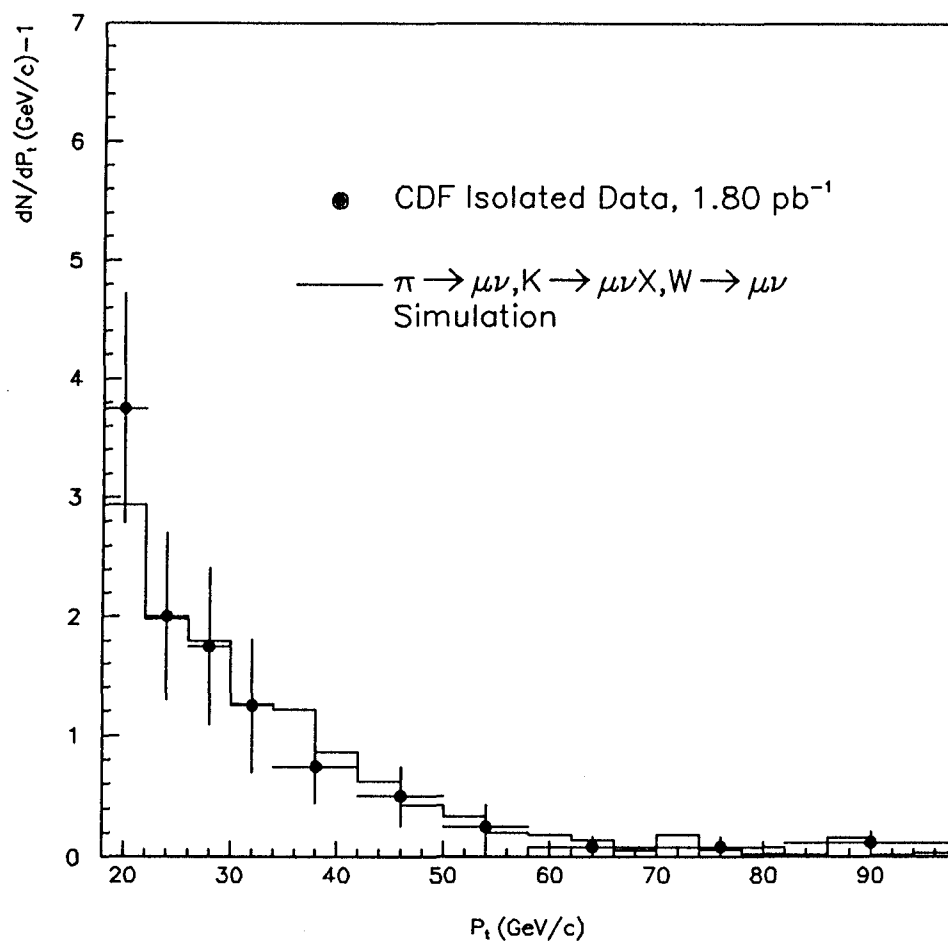


Figure 4.9: P_t Distribution for muons with $P_t > 18 \text{ GeV}/c$, $|\eta| < 2.4$ and $P(\chi^2) > .02$.

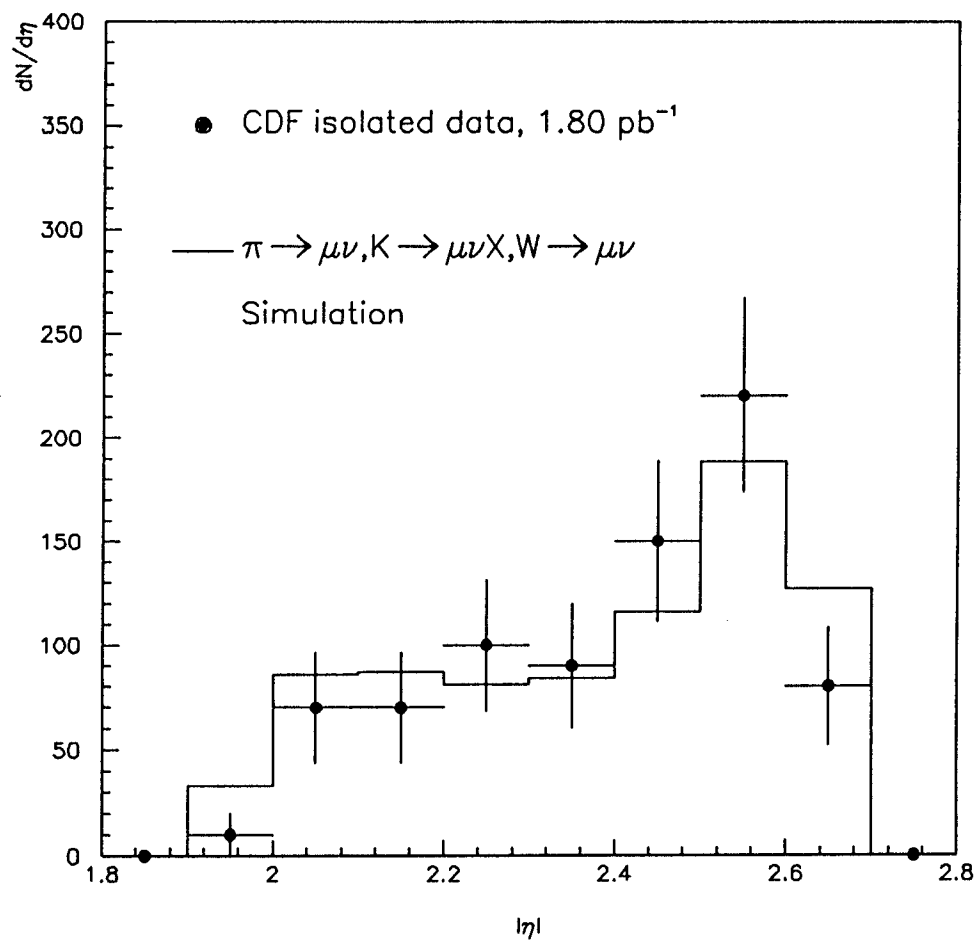


Figure 4.10: Pseudorapidity distribution for muons with $22 < P_t < 75 \text{ GeV}/c$, $|\eta| < 2.8$ and $P(\chi^2) > .02$.

# of Events with $P_t > 75\text{GeV}/c, \eta < 2.4$ and $P(\chi^2) > .02$		
Source	From Simulation	After Multiplying by coefficient
MBS mismeasurement	$1.26 \pm .23$	$1.92 \pm .40$
W Simulation	$.84 \pm .04$	$.78 \pm .15$

MBS + W Simulation	Data
$2.7 \pm .43$ events	5 events

Table 4.5: Number of Events with $P_t > 75\text{GeV}/c$ passing cuts in $|\eta| < 2.4$ region and passing $P(\chi^2) > .02$.

FMU-CMU acceptance. This acceptance was verified without detector effects by an independent analysis [39]. For the final estimate, the forward muons are required to pass the offline cuts used to select W candidates.

Table 4.6 lists the number of Z^0 decay muons passing the selection cuts, where events have been grouped into five categories depending on properties of the second muon. The first group requires the second muon to be observed in the central muon chambers; the central muon to be isolated with $E^{em} < 2\text{GeV}$ and $E^{had} < 6\text{GeV}$ in the muon tower and the border tower energy must be less than 5GeV [40]. (The border tower energy is the transverse energy in a cone of radius $R=.4$ around the muon, excluding the muon tower.) In addition, the FMU-CMU invariant mass is required to be $M > 60\text{GeV}$. The second group requires the second muon to be reconstructed as an isolated minimum ionizing track with $|\eta| < 1.0$ yielding an invariant FMU-CMIO mass with $M > 60\text{GeV}$. The isolation requirement is the same as for group 1. The third group requires the second muon to be reconstructed as an isolated minimum ionizing track with $1.0 < |\eta| < 1.4$, yielding an invariant FMU-CMIO mass with $M > 60\text{GeV}$ where the isolation requirement is again the same as for group 1. The fourth group requires the second muon to be reconstructed in the forward muon chambers with $P_t > 5\text{GeV}/c$. Each of the four groups described above are explicitly removed from the data sample. The fifth group represents the remaining Z^0 background in the W signal and includes all events not included in groups 1-4.

Also listed in Table 4.6 are the observed numbers of data events that satisfy

the requirements listed for each group. While the statistics are very low, the predicted numbers are consistent with the data. The expected number of $Z^0 \rightarrow \mu^+ \mu^-$ background events in our W signal region is thus $1.64 \pm .24$. As mentioned earlier, the Z^0 events are expected to have a $P(\chi^2)$ distribution very similar to W decays (See Appendix 1). Thus the true W signal is equal to the predicted W signal as listed in Table 4.3 minus the predicted Z^0 events.

$Z^0 \rightarrow \mu^+ \mu^-$ Background		
Type of Z^0 Background	Simulation Predicted Evt's	Data Observed Evt's
Group 1 FMU-CMUO	$1.27 \pm .19$	4.0
Group 2 FMU-CMIO ($ \eta_{cmio} < 1.0$)	$1.28 \pm .19$	1.0
Group 3 FMU-CMIO ($1.0 < \eta_{cmio} < 1.4$)	$.44 \pm .06$	0
Group 4 FMU-FMU	$.45 \pm .07$	1.0
Group 5 FMU-other	$1.64 \pm .24$	

Table 4.6: Z^0 Background

4.8 QCD Background

The QCD background to the W signal comes from two sources. The first source is from $b\bar{b}$ and $c\bar{c}$ production where one of the b's (c's) decays into a stiff muon and the energy of the other decay products is small enough that the calorimeter observes $E_t < 5\text{GeV}$ in a cone of radius $R=.55$ surrounding the muon. The second source of QCD background occurs when one of the jets in a dijet event fragments into a stiff kaon or pion which then decays into a muon. However, this second source is already included in the decay-in-flight background.

The azimuthal angle, $\Delta\phi$ between the muon and the cluster with highest transverse energy is used to estimate the QCD background, since this distribution has a different shape for W +jet events than for events produced from QCD processes. Only those clusters with $E_t > 10\text{GeV}$ (uncorrected) are considered.

In Figure 4.11a, we plot $\Delta\phi$ for the FMU W candidates containing a jet with $E_t > 10\text{GeV}$. In Figure 4.11b, we plot the same distribution for non-isolated muons in the range $18 < P_t < 22\text{GeV}/c$. These events should be dominated by the QCD processes listed above. Finally, we use a Papageno Monte Carlo simulation of W^+ +jet, with a cut $P_t(W) > 10\text{GeV}/c$ to correspond to our jet cut. This distribution is shown in Figure 4.11c normalized to the number of observed W candidates. Also shown in Figure 4.11c is the distribution for the W candidates.

The $\Delta\phi$ distribution for the non-isolated sample is peaked at 180° with a small enhancement at 0° and almost nothing inbetween. The observed data on

the other hand look more like the W +jet simulation which is almost flat in $\Delta\phi$. Since there is only one W candidate observed with $\Delta\phi$ near 180° , we set an upper limit of 1 event for the QCD background contribution. Since this is at the same level as the high P_t decay-in-flight estimate, to avoid double counting we do not make a separate correction for it.

4.9 Results

The results of the forward muon background analysis are listed in table 4.7 with the biggest W backgrounds being mismeasured $\pi \rightarrow \mu, K \rightarrow \mu$.

Forward/Backward $W \rightarrow \mu\nu$	
Candidates	34
decay-in-flight Background	10.88 ± 3.02
Z^0 Background	$1.64 \pm .24$
Signal	21.58 ± 3.03

Table 4.7: Measured number of forward muons

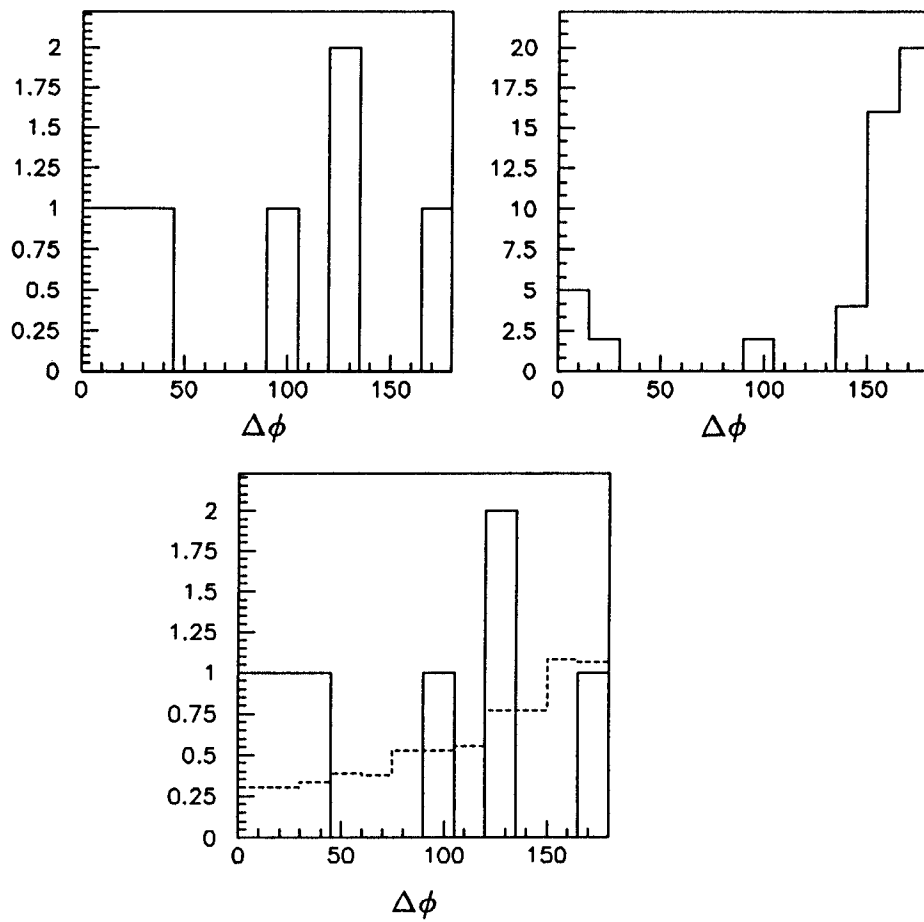


Figure 4.11: Azimuthal separation between muon and the leading jet for events with a jet satisfying $E_t > 10\text{GeV}$. a.) CDF W candidates; b.) CDF non-isolated FMU sample; c.) Papageno events normalized to CDF W candidates.

Chapter 5

The Asymmetry Measurement

The W boson forward muon decay asymmetry is determined in this chapter using the muon events described in Chapter 4. The asymmetry is determined using Equation 1.16 from Chapter 1. This equation can be rewritten in terms of the number of observed signal events, the number of predicted background events, and the efficiencies for muon detection in the east and west ends as follows:

$$A = \frac{\frac{N_S^{+E} - N_{mbs}^{+E} - N_Z^{+E}}{\epsilon_E} + \frac{N_S^{-E} - N_{mbs}^{-E} - N_Z^{-E}}{\epsilon_E} - \frac{N_S^{+W} - N_{mbs}^{+W} - N_Z^{+W}}{\epsilon_W} - \frac{N_S^{-W} - N_{mbs}^{-W} - N_Z^{-W}}{\epsilon_W}}{\frac{N_S^{+E} - N_{mbs}^{+E} - N_Z^{+E}}{\epsilon_E} + \frac{N_S^{-E} - N_{mbs}^{-E} - N_Z^{-E}}{\epsilon_E} + \frac{N_S^{+W} - N_{mbs}^{+W} - N_Z^{+W}}{\epsilon_W} + \frac{N_S^{-W} - N_{mbs}^{-W} - N_Z^{-W}}{\epsilon_W}} \quad (5.1)$$

where $N_S^{+E}, N_S^{-E}, N_S^{+W}, N_S^{-W}$ are the number of observed signal events in each asymmetry bin; $N_{mbs}^{+E}, N_{mbs}^{-E}, N_{mbs}^{+W}, N_{mbs}^{-W}$ are the number of minimum bias background events and $N_Z^{+E}, N_Z^{-E}, N_Z^{+W}, N_Z^{-W}$ are the number of Z^0 background events in each asymmetry bin. The east and west detection efficiencies are ϵ_E and

ϵ_W respectively and were determined in in Chapter 3. We define the following

$$\begin{aligned}
 N_{tot} &= \sum_i N_S^i \\
 N^i &= N_S^i - N_{mbs}^i - N_Z^i \\
 N_{tot}^{corr} &= \frac{N^{+E}}{\epsilon_E} + \frac{N^{-E}}{\epsilon_E} + \frac{N^{+W}}{\epsilon_W} + \frac{N^{-W}}{\epsilon_W}
 \end{aligned} \tag{5.2}$$

where $i = +E, -E, +W, -W$ and rewrite Equation 5.1 as

$$A = \frac{\frac{N^{+B}}{\epsilon_B} + \frac{N^{-W}}{\epsilon_W} - \frac{N^{+W}}{\epsilon_W} - \frac{N^{-B}}{\epsilon_B}}{N_{tot}^{corr}} \tag{5.3}$$

Unlikely as it first seems, the asymmetry is not affected by the inherent charge bias of the trigger. To understand generally why the trigger shouldn't affect the asymmetry, we use a detector simulation. The detector simulation includes both the production of extra hits as well as Moliere scattering and is described in detail in Chapter 3.

Since both forward and backward toroids act to focus negative charges and defocus positive charges, the trigger treats positively charged tracks in the same way for both detector regions. Thus, the lepton asymmetry as determined from the positively charged muons, equals the asymmetry as determined from the negatively charge muons even though the acceptance for negative charges is larger. The asymmetry computed using both charges is equivalent to the average of the asymmetry of positive charges and the asymmetry of negative charges. For that reason, the measurement is not affected by the trigger charge bias.

This result is shown in Figure 5.1 and quantified in Table 5.1. The input asymmetry values shown in Table 5.1 are determined from a detector simulation

using Papageno $W+0$ jet events. For each simulation run, 10^6 events were generated. The first 10^5 events which had a lepton in the detector region $|\eta| > 1.7$ were detector simulated using the fast monte carlo [24] and the simulated events were required to pass offline trigger plus data cuts. The asymmetry was determined for the signal region of $22 < P_t^{fit} < 75 \text{ GeV}/c$ and $2.0 < |\eta| < 2.4$. As shown in the Figure 5.1, there were more negatively charged events due to the trigger efficiency but, as shown in the Table 5.1, the asymmetry for the different charges was not affected by the trigger bias.

The asymmetry as measured by Equation 5.3 is thus corrected for east and west efficiency differences and the background contribution has been subtracted out. This number, in principle, can be compared to predicted lepton asymmetries for our value of pseudorapidity.

5.1 Trigger Bias For Low Statistics.

As it turns out, the results of Table 5.1 are true, but only in the limit of high statistics which is not the case for our measurement. Because of our low statistics, we make a correction to the asymmetry as computed by Equation 5.3 and this is due to the trigger bias. (This doesn't contradict the previous section, since in the limit of high statistics as shown in Table 5.1, this correction is zero.)

The correction is determined by including the trigger efficiencies for negative and positive charges, ϵ^-, ϵ^+ , in Equation 5.3. Since the trigger efficiency is a function of P_t , we expect different ϵ^+, ϵ^- values for signal and background. It

	Asymmetry for +Q	Asymmetry for -Q	Asymmetry for +Q and -Q
EHLQ1			
M.C. Input Run1	-.1781	-.1781	-.178
M.C. Input Run2	-.2051	-.2045	-.205
M.C. Input Run3	-.2237	-.1715	-.198
M.C. Input Mean	$-.202 \pm .011$	$-.185 \pm .010$	$-.194 \pm .008$
Det. Sim. Run1	-.1674	-.1760	-.172
Det. Sim. Run2	-.1570	-.1693	-.163
Det. Sim. Run3	-.1873	-.2255	-.206
Det. Sim. Mean	$-.170 \pm .009$	$-.190 \pm .018$	$-.180 \pm .013$
Martinelli 1			
M.C. Input Run1	-.2141	-.2110	-.213
M.C. Input Run2	-.2325	-.2317	-.232
M.C. Input Run3	-.2135	-.2441	-.229
M.C. Input Mean	$-.230 \pm .006$	$-.229 \pm .010$	$-.225 \pm .006$
Det. Sim. Run1	-.1708	-.1742	-.173
Det. Sim. Run2	-.2332	-.2192	-.226
Det. Sim. Run3	-.1699	-.2500	-.210
Det. Sim. Mean	$-.191 \pm .021$	$-.214 \pm .022$	$-.203 \pm .016$

Table 5.1: The predicted lepton asymmetry from the PAPAGENO monte carlo and after a forward muon detector simulation which includes trigger effects.

turns out, after detector simulation effects are included, the means of these two P_t distributions are approximately equal, being within one standard deviation of each other. (This is for events in the region $22 < P_t < 75\text{GeV}/c$, $|\eta| < 2.4$ and $P(\chi^2) > .02$). Table 5.2 lists the ϵ^+, ϵ^- average efficiencies. These values were determined using the mean P_t and the trigger efficiency curve in Figure 2.13. As shown, the efficiencies for the background and signal are within a standard deviation of each other. We assume the W value for ϵ^+ and ϵ^- .

Source	Mean P_t	ϵ^+	ϵ^-
Min. Bias	34.0 ± 3.1	$.370 \pm .011$	$.540 \pm .011$
W	$36.5 \pm .3$	$.380 \pm .011$	$.540 \pm .011$

Table 5.2: The average trigger efficiency for a specified mean P_t

If we define N'_{corr} to be

$$N'_{corr} = \frac{N^{+E}}{\epsilon_B \epsilon^+} + \frac{N^{-W}}{\epsilon_W \epsilon^-} + \frac{N^{+W}}{\epsilon_W \epsilon^+} + \frac{N^{-E}}{\epsilon_B \epsilon^-} \quad (5.4)$$

then Equation 5.3 can be rewritten to include the trigger efficiencies.

$$A' = \frac{\frac{N^{+B}}{\epsilon_B \epsilon^+} + \frac{N^{-W}}{\epsilon_W \epsilon^-} - \frac{N^{+W}}{\epsilon_W \epsilon^+} - \frac{N^{-B}}{\epsilon_B \epsilon^-}}{N'_{corr}} \quad (5.5)$$

To understand how Equation 5.3 is different than Equation 5.5, we define $\delta = \epsilon^- - \epsilon^+$ and use the approximation that

$$\frac{\delta}{\epsilon^-} \frac{N^{-W}}{\epsilon_W} + \frac{N^{-B}}{\epsilon_B} \quad (5.6)$$

is small. Then Equation 5.5 can be expressed in terms of the asymmetry computed in Equation 5.3.

$$A' - A = A \left(\frac{\delta}{\epsilon^-} \frac{N^{-W} + \frac{N^{-B}}{\epsilon_B}}{N_{tot}^{corr}} + \left(\frac{\delta}{\epsilon^-} \right)^2 \left(\frac{N^{-W} + \frac{N^{-B}}{\epsilon_B}}{N_{tot}^{corr}} \right)^2 \right) - \frac{\delta}{\epsilon^-} \frac{N^{-W} - \frac{N^{-B}}{\epsilon_B}}{N_{tot}^{corr}} \left(1 + \frac{\delta}{\epsilon^-} \frac{N^{-W} + \frac{N^{-B}}{\epsilon_B}}{N_{tot}^{corr}} \right). \quad (5.7)$$

The quantity $A' - A$ is the correction to the observed asymmetry due to the charge bias in the trigger and due to the small statistics of our sample.

5.2 Charge Bias in Track Reconstruction and Tracking Cuts

Besides the trigger, the forward muon track reconstruction and the tracking cuts used for data selection were studied for charge biases. We use a detector simulation to study this.

The FMU track reconstruction is performed by the FMTRK module. This module is used both online as part of the software trigger and offline in data analysis. To determine if there was a charge dependence in the track reconstruction of the FMTRK module, the chamber efficiency in the simulation was set to 100% and survey errors were not included since these processes cannot be charge dependent. Z^0 decay muons generated by ISAJET were detector simulated. The number of tracks which reconstructed with a non zero P_t was recorded for both positive and negative charges. Within statistical uncertainty, the track reconstruction was found to be charge independent with $.9886 \pm .0013$ of nega-

tively charged tracks reconstructing and $.9879 \pm .0015$ of positively charged tracks reconstruction.

Besides the trigger requirement, the data selection include calorimetry plus tracking cuts. The calorimetry cuts should be charge blind and thus not introduce any charge bias into the data.

The tracking cuts used for data selection consist of the $P(\chi^2)$ cut. We note, however, any bias from this cut would be included in the results of Table 5.1 since these events were required to pass the offline data cuts. To study the charge dependence of this $P(\chi^2)$ cut, positive and negatively charged events are required to satisfy the offline data plus trigger requirements with the exclusion of the $P(\chi^2)$ cut. Listed in Table 5.3 are the percentage of events passing different $P(\chi^2)$ cuts. These results are listed separately for positive and negative charges. From this study, we conclude the $P(\chi^2)$ cut has no charge dependence. (The simulated $P(\chi^2)$ distribution is studied in detail in Appendix 1 and is shown to do a good job at modelling the Z^0 data distribution.)

5.3 Background Distributions

To measure the asymmetry, we subtract the background from each bin as formulated in Equation 5.1. This requires knowing the background level as well as the charge distribution of the background. The charge distribution will also be affected by the trigger bias .

The largest background to the W signal is mismeasured low P_t decay in flight

$W \rightarrow \mu\nu$	+Q	-Q
$P(\chi^2) > .0005$	$.929 \pm .003$	$.933 \pm .003$
$P(\chi^2) > .02$	$.845 \pm .005$	$.850 \pm .004$
$P(\chi^2) > .1$	$.721 \pm .006$	$.730 \pm .005$
$\pi, K \rightarrow \mu\nu, X$	+Q	-Q
$P(\chi^2) > .0005$	$.374 \pm .017$	$.396 \pm .017$
$P(\chi^2) > .02$	$.253 \pm .015$	$.256 \pm .015$
$P(\chi^2) > .1$	$.197 \pm .014$	$.190 \pm .014$

Table 5.3: Charge independence of the $P(\chi^2)$ cut.

muons (see Chapter 4). The fraction of muons in the W signal region believed to be from this source was determined in Chapter 4. We define the parameter f_{mbs} to equal this fraction, $f_{mbs} = .32 \pm .07$. Therefore, the number of minimum bias background events is equal to

$$\begin{aligned}
 N_{mbs} &= f_{mbs} N_{tot} \\
 &= 10.9 \pm 3.0
 \end{aligned}
 \tag{5.8}$$

Since there is no charge asymmetry in the production of π, K decays, the trigger bias is expected to determine the charge distribution of this background. We use the detector simulation to determine the measured charge distribution of the minimum bias background. The simulated minimum bias events were

required to pass offline trigger plus data cuts. In the region of $P_t > 15\text{GeV}/c$, the $+Q/-Q$ ratio as predicted from a detector simulation which included trigger effects was found to model the data well (see chapter 3.) We define the fraction of reconstructed minimum bias events which have positive measured charge to be f^+ as determined from the monte carlo. This parameter is equal to $f^+ = .396 \pm .033$. The number of background minimum bias events in the asymmetry bins is thus defined as

$$N_{mbs}^{+E} = \frac{\epsilon_E}{\epsilon_E + \epsilon_W} f^+ f_{mbs} N_{tot} \quad (5.9)$$

$$N_{mbs}^{-E} = \frac{\epsilon_E}{\epsilon_E + \epsilon_W} (1 - f^+) f_{mbs} N_{tot} \quad (5.10)$$

$$N_{mbs}^{+W} = \frac{\epsilon_W}{\epsilon_E + \epsilon_W} f^+ f_{mbs} N_{tot} \quad (5.11)$$

$$N_{mbs}^{-W} = \frac{\epsilon_W}{\epsilon_E + \epsilon_W} (1 - f^+) f_{mbs} N_{tot} \quad (5.12)$$

Table 5.4 lists the predicted minimum bias background for each bin.

Bin	No. of Predicted Minimum Bias Bkgd Events
N_{mbs}^{+E}	$2.0 \pm .6$
N_{mbs}^{-E}	3.0 ± 1.0
N_{mbs}^{+W}	$2.3 \pm .7$
N_{mbs}^{-W}	3.6 ± 1.1

Table 5.4: Minimum bias Background for different asymmetry bins.

The second background to the W signal is from prompt Z^0 decays where one leg hits the forward muon chambers and the other leg is undetected. About 5% of the high P_t muons in the W signal region are predicted to be from Z^0 decays as determined from Monte Carlo. To determine the lepton asymmetry, we also subtract this small background from each bin. Table 5.5 lists the predicted Z^0 background for each bin.

Bin	No. of Predicted Z^0 Bkgd Events
N_Z^{+E}	$.30 \pm .04$
N_Z^{-E}	$.50 \pm .06$
N_Z^{+W}	$.31 \pm .04$
N_Z^{-W}	$.45 \pm .05$

Table 5.5: Z^0 Background for different asymmetry bins.

5.4 The Asymmetry.

The lepton asymmetry is determined using both Equation 5.3 and Equation 5.5. The asymmetry is computed for the signal region of $2.0 < |\eta| < 2.4$ and $22 < P_t < 75 \text{ GeV}/c$. Equation 5.5 predicts an asymmetry equal to $-.06 \pm .27 \pm .01$ where $.27$ is the statistical error and $.01$ is the systematic error. Table 5.6 is a summary of the number of observed events in each bin, the number of Z^0 background

events, the efficiencies used for computing the asymmetry and the asymmetries themselves. Figure 5.2 shows the forward muon lepton asymmetry compared to a leading order calculation as a function of pseudorapidity for different structure functions. This calculation numerically integrates the W rapidity spectrum of the leptons in the W rest frame with the angular distribution proportional to $(1 - \cos \theta_{cm})^2$, which is expected for V-A couplings [42]. Unfortunately, due to the statistical error the present measurement is unable to distinguish between structure functions. However, this measurement is consistent with the predictions of all structure functions.

5.5 The Asymmetry Error

The uncertainty in the asymmetry is completely dominated by the statistical size of the data. The actual error is computed by solving

$$dA = \sqrt{\sum_i \left(\frac{dA}{dX_i} \Delta X_i \right)^2} \quad (5.13)$$

where dA/dX_i is the partial derivative of Equation 5.5 and where X_i are the various variables in Equation 5.5. Table 5.7 shows the weight for each partial derivative term in Equation 5.13. From this table, we see the first four rows contribute the most to the error and it is these rows which are the statistical portion.

To understand how the size of the background affects the statistical error we simplify Equation 5.13 to include only the largest contributions. Equation 5.13

	N^{+E} bin	N^{-E} bin	N^{+W} bin	N^{-W} bin
Observed EvtS	6 ± 2.4	6 ± 2.4	11 ± 3.3	11 ± 3.3
mbs background	$2.0 \pm .6$	3.0 ± 1.0	2.3 ± 0.7	3.6 ± 1.1
Z^0 background	$.30 \pm .04$	$.50 \pm .06$	$.31 \pm .04$	$.45 \pm .05$

N_{tot}	= 34	Total number of observed events.
f_{mbs}	= $.32 \pm .07$	fraction of evts which are MBS bkgd.
f^+	= $.396 \pm .044$	fraction of MBS evts with +Q.
ϵ_E	= $.302 \pm .021$	East detector efficiency.
ϵ_W	= $.356 \pm .023$	West detector efficiency.
ϵ^+	= $.38 \pm .01$	Positive Q trigger efficiency.
ϵ^-	= $.54 \pm .01$	Negative Q trigger efficiency.
A	= $.004 \pm .274 \pm .005$	Computed using Equation 5.3
A'	= $-.06 \pm .27 \pm .01$	Computed using Equation 5.5

Table 5.6: Summary of the number of observed events in each bin, the number of Z^0 background events and the efficiencies used for computing the asymmetry and the asymmetries themselves.

Partial Derivative	Weight
$\frac{dA}{dN_S^{+E}} \Delta N_S^{+E}$	2.27E-2
$\frac{dA}{dN_S^{-E}} \Delta N_S^{-E}$	9.84E-3
$\frac{dA}{dN_S^{-W}} \Delta N_S^{-W}$	1.49E-2
$\frac{dA}{dN_S^{+W}} \Delta N_S^{+W}$	2.61E-2
$\frac{dA}{dE_e} \Delta E_e$	8.02E-5
$\frac{dA}{dE_w} \Delta E_w$	6.93E-5
$\frac{dA}{dE^+} \Delta E^+$	1.88E-5
$\frac{dA}{dE^-} \Delta E^-$	6.43E-6
$\frac{dA}{df_{mbs}} \Delta f_{mbs}$	3.63E-5
$\frac{dA}{df^+} \Delta f^+$	1.07E-7
$\frac{dA}{dN_Z^{+E}} \Delta N_Z^{+E}$	6.37E-6
$\frac{dA}{dN_Z^{+W}} \Delta N_Z^{+W}$	3.66E-6
$\frac{dA}{dN_Z^{-E}} \Delta N_Z^{-E}$	3.94E-6
$\frac{dA}{dN_Z^{-W}} \Delta N_Z^{-W}$	5.11E-6

Table 5.7: Weights for each partial derivative term used for computing the asymmetry error.

is thus very nearly equal to

$$dA = \frac{\sqrt{\frac{N_S^{+B}}{(\epsilon_B \epsilon^+)^2} + \frac{N_S^{-B}}{(\epsilon_B \epsilon^-)^2} + \frac{N_S^{+W}}{(\epsilon_W \epsilon^+)^2} + \frac{N_S^{-W}}{(\epsilon_W \epsilon^-)^2}}}{N_{tot}^{corr}} \quad (5.14)$$

where N_{tot}^{corr} is the corrected total number of W candidates. From this equation, we see how a larger background leads to a larger statistical error. In Table 5.8, we show the error on the statistical error as we vary the background fraction by one standard deviation.

f_{mbs}	N_{tot}^{corr}	dA
.32	145.8	.27
.39	130.2	.30
.25	161.5	.24

Table 5.8: The error on the statistical error of the asymmetry is shown by varying the background fraction by one standard deviation.

Table 5.9 lists values for the different statistical and systematic errors.

5.6 Corrections to the Asymmetry

5.6.1 Higher Order Corrections.

As shown in Chapter 1, since the $K(y)$ factor associated with the higher order contributions to QCD is basically independent of W rapidity for the region $|\eta| < 2.5$,

Source of Error	Value
Statistical error alone $dN_S^i \neq 0$	$\pm.271$
Systematic error in background fraction $f_{mbs}=.04$	$\pm.003$
Systematic error due to the charge uncertainty in minimum bias bkgd	$\pm.003$
Systematic error due to the east/west efficiency uncertainty	$\pm.012$
Systematic error due to uncertainty in trigger efficiency	$\pm.005$
Systematic error associated with Z^0 background uncertainty	$\pm.004$
Total Systematic error	$\pm.014$
Total Error on Asymmetry	$\pm.272$

Table 5.9: The statistical and systematic errors to the lepton asymmetry.

we do not expect the higher order correction to the W asymmetry (Equation 1.8 of Chapter 1) to be large. The $K(y)$ factor was defined in Equation 1.17 and this distribution was shown in Figure 1.12.

However, we measure the lepton asymmetry (Equation 1.16 of Chapter 1). Since higher order contributions tend to give the W transverse motion which can wash out the lepton decay asymmetry (See Chapter 1), a study of the effects of $P_t(W)$ is warranted. To investigate the effects of the transverse motion of the W on the observed lepton asymmetry, I used the Papageno Monte Carlo [43] by studying $W+1$ jet events for W 's with finite P_t . The Papageno generator contains the complete production/decay matrix elements for the process $p\bar{p} \rightarrow W + X, W \rightarrow \mu\nu$ at both zeroth and first order in α_s .

The lepton asymmetry is determined by generating events with a particular $(P_t)_W^{min}$ value and then using a very restricted $(P_t)_W$ region for the EHLQ1, MRS and Martinelli structure functions. In the various simulation runs, each event was required to pass cuts used in the W asymmetry analysis, $22 < P_t(\text{lepton}) < 75\text{GeV}$. I generate three runs each of 10^6 Papageno events. The error on each asymmetry point was determined from the statistical mean and sigma of the three measurements. The resulting asymmetry is expressed as a function of $(P_t)_W$ and is shown in Figure 5.4. The points at $(P_t)_W^{min} = 0$ are just the zeroth order W production.

The $P_t(W)$ distribution for our sample is shown in Figure 5.3 with a mean $P_t(W) = 10.0\text{GeV}/c$. The $P_t(W)$ distribution is determined using the transverse

motion of the muon and the neutrino. The neutrino transverse motion is determined from the missing energy vector, \vec{E}_t as observed in the calorimeter.

The \vec{E}_t is first corrected to remove the muon energy deposition in the calorimeter. The muon transverse energy in a 3x3 array of calorimeter towers centered on the muon is used for this correction (See Figure 3.1 of Chapter 3 for total energy distributions). The \vec{E}_t is also corrected by introducing a "fudge factor" of 1.4 to correct the energy scale for non-linearities in the calorimeter [44]. The final corrected \vec{E}_t contains the energy missing from both the muon and the neutrino and is described as follows

$$\vec{E}'_t = 1.4 \vec{E}_t + \vec{E}_t^\mu \text{ (3x3 array of towers).}$$

To determine the transverse motion of the neutrino, we subtract the effect of the muon and then we define the $P_t(W)$.

$$\vec{P}_t^\nu = \vec{E}'_t - \vec{P}_t^\mu \quad (5.15)$$

$$\vec{P}_t(W) = \vec{P}_t^\nu + \vec{P}_t^\mu \quad (5.16)$$

Using the mean from our sample of 10GeV/c, we estimate the size of the first order correction to be less than 10% with this correction tending to decrease the asymmetry. Because of the large statistical uncertainty of our sample, however we only point out the expected behavior of the asymmetry once first order diagrams are included.

5.6.2 Mismeasured Charged Tracks

Since the asymmetry relies on the charge of the lepton, a mismeasurement of this charge could obscure the asymmetry result. There are primarily two ways in which a charge mismeasurement can occur. The first way occurs when extra hits in the muon chambers due to the production of delta rays are used by the track fitter instead of the true muon hits (see Appendix 2). The second way occurs when the muon Moliere scatters in such a way that the hits reconstruct with opposite charge. Of course, a combination of these two possibilities will increase the probability of charge mismeasurement.

To investigate the reliability of the charge measurement of the forward muon fitter, we again use a detector simulation. Reconstructed events are required to pass offline cuts including the trigger requirement. We list those results in Table 5.10 where we show the percentage of events which have mismeasured charge. We see the fitter does a good job at correctly measuring the charge for W decay muons. Only $.20 \pm .06\%$ of these events are reconstructed in the signal region with the wrong charge. This result is also supported by the measured charge of the 44 FMU-CMU Z^0 candidates. There are no same sign charge events in this sample.

The mismeasured decay-in-flight muons, however are frequently measured with the wrong charge. This is not too surprising since, by definition, these events already have mismeasured P_t . Since the mismeasured charge occurs when

tracks are badly scattered, as many positive charged tracks are measured negatively as negative charged tracks are measured positively. We use the measured charge in reconstructed monte carlo events to determine the charge distribution for the mismeasured decay-in-flight background and it is this distribution which is used for subtracting the minimum bias background from the data. For this reason the minimum bias events with mismeasured charge do not distort the asymmetry measurement.

Muon Source	Fraction of events with mismeasured charge
<i>W</i> Decays	$.0020 \pm .0006$
Decay-in-flight	$.265 \pm .032$

Table 5.10: Probability of fitter to mismeasure the charge.

5.7 CDF Asymmetry Results from other Detector Regions.

In parallel with the forward muon analysis, the *W* lepton asymmetry has been measured using central muons [45], central electrons [46] and plug electrons [47]. While this analysis is different from the central measurements (because we use a different P_t cut with no M_t requirement) the central muon data points can still be combined with the forward muon data point for an overall comparison once

the predicted asymmetry curves are corrected for these different cuts. (The effect of the M_t and P_t cuts was described in Chapter 1). Figure 5.5a shows the combined electron asymmetry and Figure 5.5b shows the combined muon asymmetry compared to asymmetries predicted by various structure functions. The jump between the central and plug region in the theoretical electron asymmetry curves is explained by the difference in data selection cuts for these two samples. The same reason also explains the jump between the central and forward region in the theoretical muon asymmetry curves.

5.8 Conclusions

In conclusion, muons events from $W^\pm \rightarrow \mu^\pm \nu$ decays were collected in the forward-backward region by the Collider Detector at Fermilab during the 1988-89 run and these events have been used to measure the lepton charge asymmetry. While the measurement is too statistically limited to distinguish between structure functions, the result is consistent with the current standard model for all structure functions as well as consistent with the asymmetry measurement from other lepton samples at CDF.

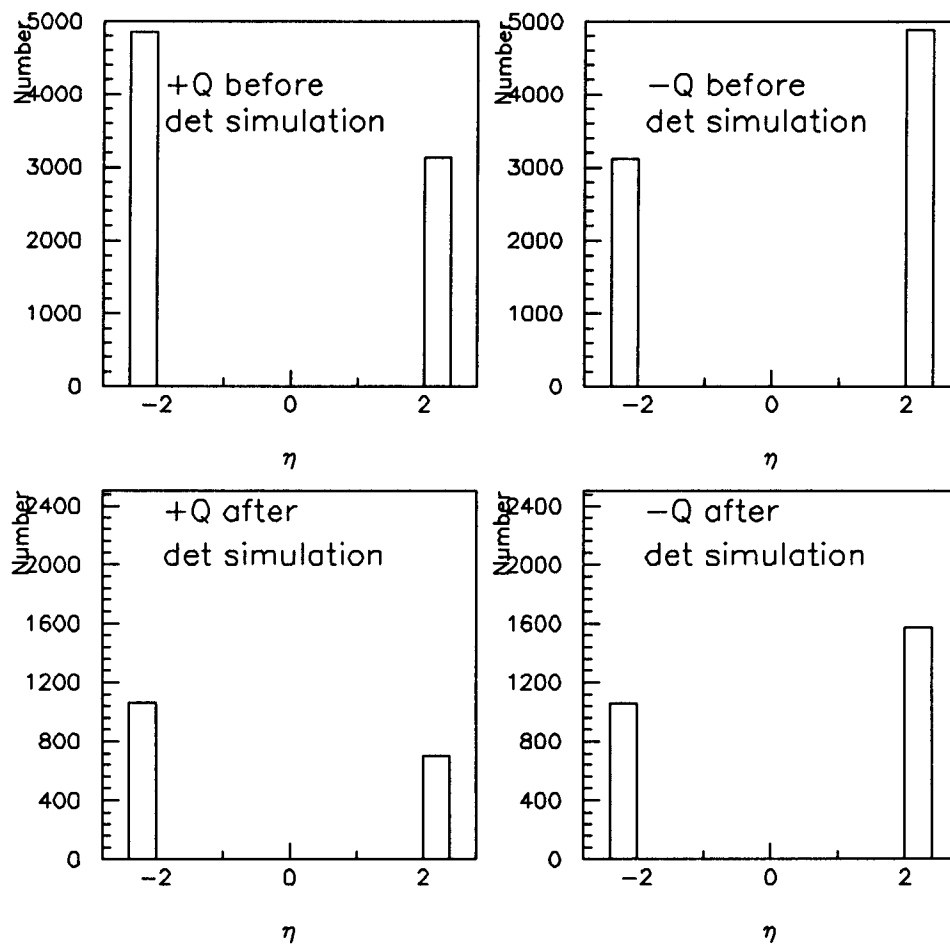


Figure 5.1: Schematic of Trigger Detector Effects to W Decay Asymmetry.

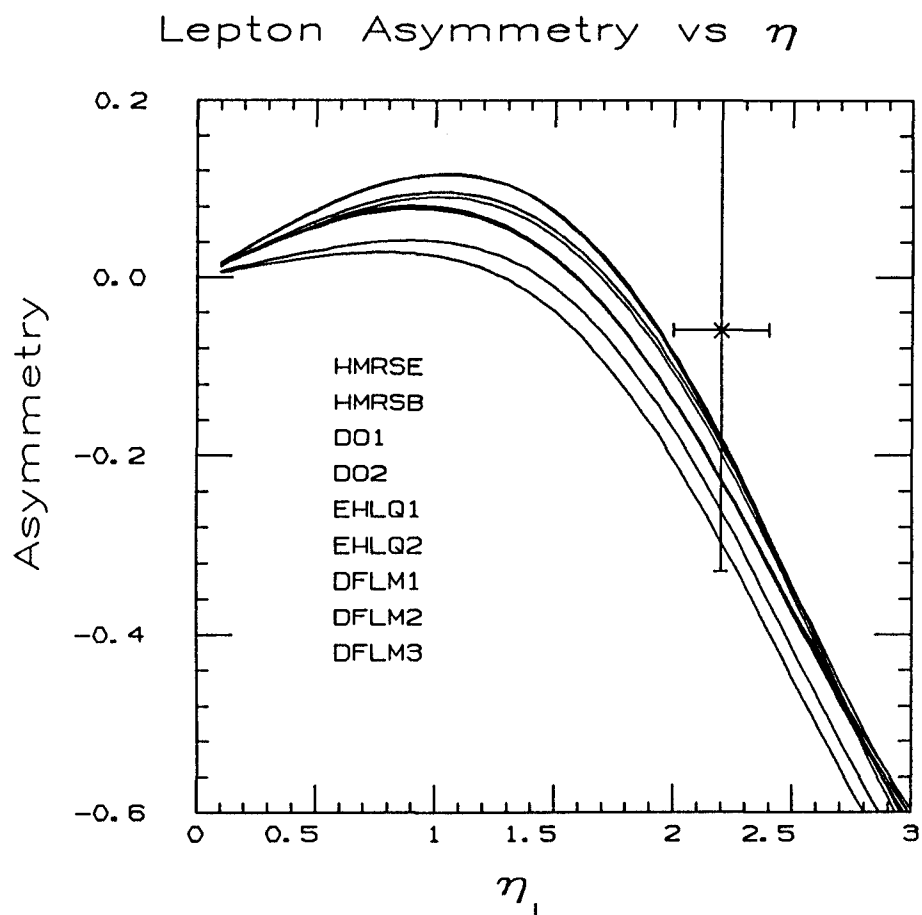


Figure 5.2: Forward Muon Lepton Asymmetry compared to Zeroth order theory Predictions.

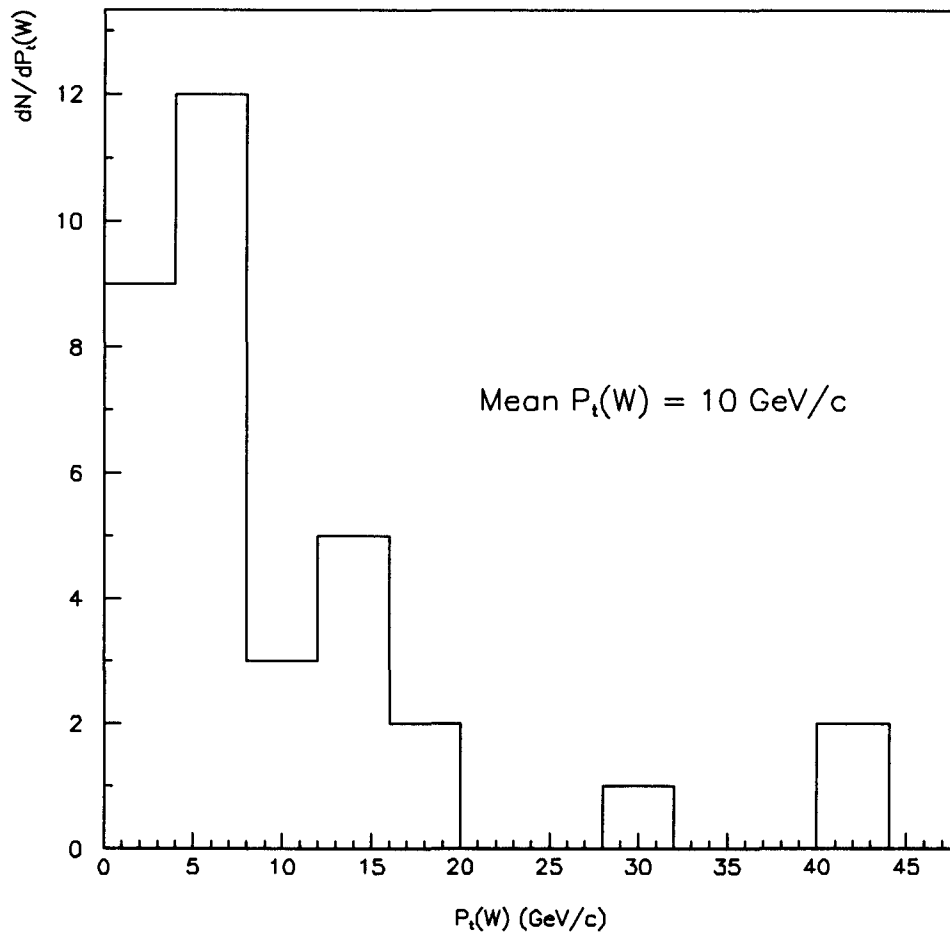


Figure 5.3: Forward Muon $P_t(W)$ Distribution (GeV/c)

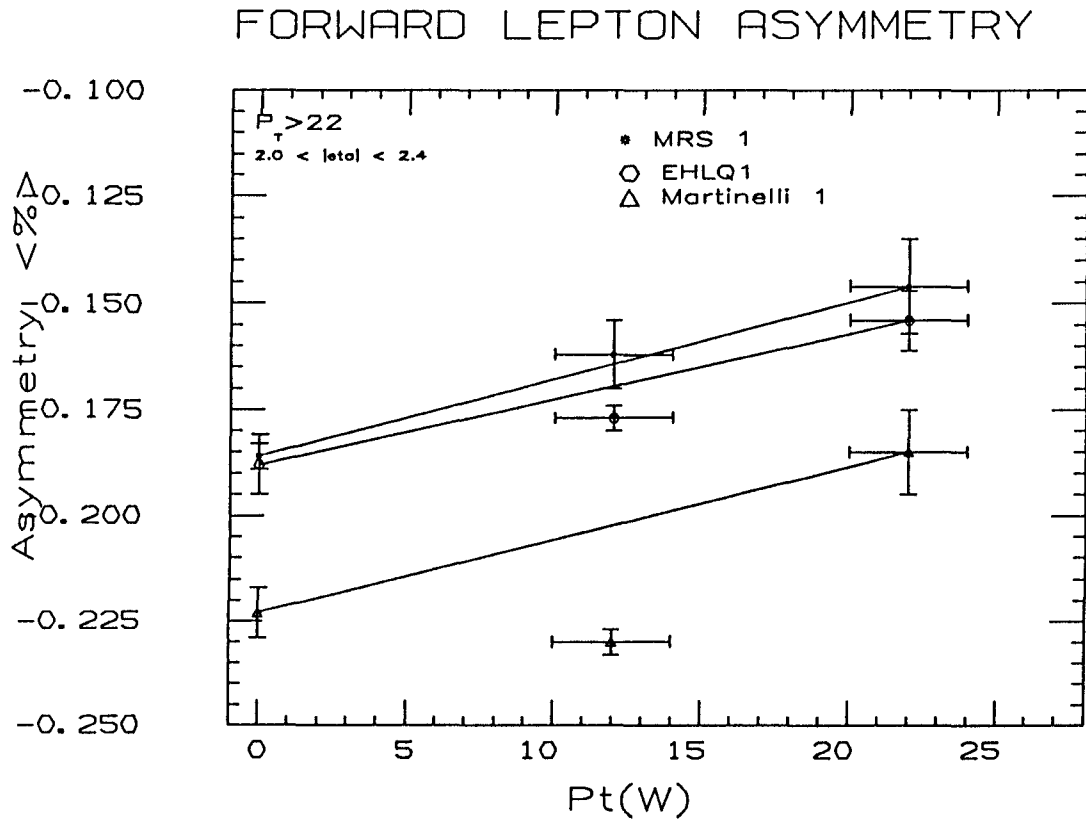


Figure 5.4: Forward Muon Lepton Asymmetry as a function of $P_t(W)$ for the rapidity interval $2 < |\eta| < 2.4$ and $P_t^\mu > 22 \text{ GeV}/c$.

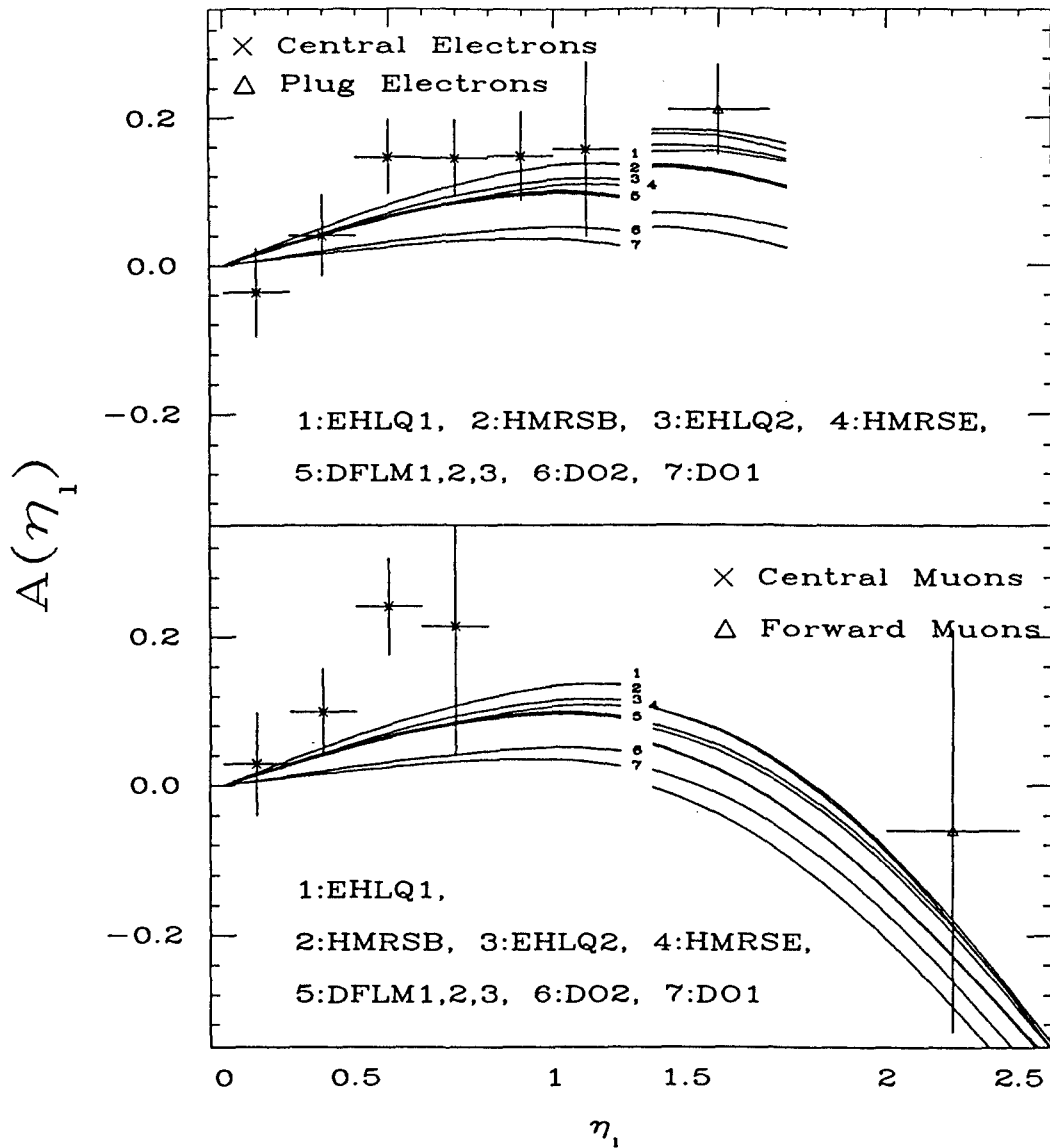


Figure 5.5: CDF Lepton Asymmetry compared to Zeroth order theory Predictions.

Appendix A

Efficiency of the Forward Muon

$P(\chi^2)$ Cut

A.1 Introduction

This appendix describes the efficiency of the χ^2 probability ($P(\chi^2)$) cut used for selecting forward muons. The $P(\chi^2)$ is determined from the normal χ^2 distribution by the relation

$$P(\chi^2 > \chi_i^2) = \frac{\int_{\chi_i^2}^{\infty} F(\chi^2) d\chi^2}{\int_0^{\infty} F(\chi^2) d\chi^2} \quad (\text{A.1})$$

where $F(\chi^2)$ is the normal χ^2 distribution described by

$$F(\chi^2) = \frac{1}{2^{(\nu/2)-1} \Gamma(\nu/2)} (\chi^2)^{(\nu/2)-1} \exp^{-\chi^2/2} \quad (\text{A.2})$$

for $\chi^2 > 0$ and ν a positive integer equal to the degrees of freedom (dof). The χ^2 of the muon track is determined by the fitting algorithm and if this algorithm

correctly models the real world, then the χ^2 distribution should equal the normal χ^2 distribution. The FMU fitting algorithm uses either 3 or 4 dof depending on whether the track uses 5 or 6 hit positions in the fit. There are 3 dof for a 5 hit track and 4 dof for a 6 hit track.

If the normal χ^2 distribution is used in equation A.1, then the $P(\chi^2)$ distribution is flat from 0 to 1 and the efficiency of selecting a track with $\chi^2 < \chi_i^2$ is directly equal to the quantity

$$\epsilon(\chi^2 < \chi_i^2) = 1 - P(\chi_i^2) \quad (\text{A.3})$$

A.2 Z^0 Data Compared to Simulation

One method of studying the efficiency of the $P(\chi^2)$ cut, is to compare the CDF 1988-89 FMU-CMU Z^0 data to a monte carlo simulation. The detector simulation is described in Chapter 2. The FMU-CMU Z^0 data events were selected using central muon quantities, [39] with an additional requirement on the invariant mass ($60 < M_{fmu-cmu} < 130 GeV/c^2$). The selection criteria for these events was described in Chapter 2.

The χ^2 distribution of the Z^0 simulated data compared to that of the theoretical curve is shown in Figure A.1a (for 3 dof) and in Figure A.1b (for 4 dof). Figure A.1c shows the distribution for the simulated data compared to the CDF 88-89 data. These distributions show that the forward muon track fitting algorithm does a good job at approximating the normal χ^2 distribution for Z^0 events.

This is easier to see in the $P(\chi^2)$ distribution which is shown in figure A.1d for the simulated data compared to the FMU-CMU Z^0 data. Table A.1 shows the efficiency of the $P(\chi^2)$ cut using the FMU-CMU Z^0 events and compares these values to the simulation. Statistically, the data are consistent with the monte carlo. The slightly lower $P(\chi^2)$ efficiency of the data could possibly be explained by the chamber resolution since presumably, this distribution is not a perfect gaussian as is assumed in the monte carlo. Another possible explanation could be the momentum dependence in the distribution of extra hits distribution. The simulation models the production of extra hits using multiplicity and spatial distributions produced from a muon with momentum of 100GeV/c while the average Z^0 forward muon has a momentum of 150GeV/c.

Ideally, the $P(\chi^2)$ distribution should be flat with only .02 of the data satisfying $P(\chi^2) < .02$. The enhancement in both the data and simulation in the lowest $P(\chi^2)$ bin occurs for several reasons. First, there is a chance that a muon hit will not be observed due to chamber inefficiencies. Second, the production of extra hits in the vicinity of the muon hit coupled with the chamber resolution can cause the track fitting algorithm to misidentify the true muon hit. Third, the effect of the 100ns deadtime required by the FMU TDC's for identifying multiple hits in a single drift cell acts like an additional inefficiency. The first hit is recorded and then any hit arriving within 100ns of the first hit is lost. Fourth, the effect of survey uncertainties is similar to that of the measurement error produced by the chamber resolution, although the survey error is most sensitive to higher mo-

Data Set	$P(\chi^2) > .05$ < % >	$P(\chi^2) > .02$ < % >
Simulated Z^0		
wire1 ≥ 33	.83 \pm .02	.89 \pm .01
CDF 88-89 Z^0		
wire1 ≥ 33	.79 \pm .06	.81 \pm .06

Table A.1: A Comparison of the Efficiency of the χ^2 Probability Cut for the Z^0 Data to the Simulation.

menta tracks. Table A.2 shows how the efficiency of the $P(\chi^2)$ cut changes as each contribution described above is included in a simulation of $W \rightarrow \mu\nu$.

In conclusion, while the $P(\chi^2)$ cut efficiency of the data is lower than that predicted by the monte carlo, they are within the statistical errors. The enhancement of events with low $P(\chi^2)$ can be accounted for by known effects.

A.3 Minimum Bias Data Compared to Simulation

The majority of forward muon events are either minimum bias decays or bottom or charm decays and these processes produce muons with a softer P_t distribution. To investigate the performance of the forward muon fitting algorithm on these muons, I compare the minimum bias simulation to the minimum bias data. The

Simulated Processes	$P(\chi^2) > .05$ < % >	$P(\chi^2) > .02$ < % >
Multiple Scattering with Moliere tails (M.S.) Chamber Resolution (C.R.)	.952±.007	.977±.005
M.S., C.R. Chamber eff. (C.E.), Extra hit Production (Xhit)	.938±.008	.963±.006
M.S.,C.R.,C.E.,Xhit 100ns TDC deadtime (TDC)	.902±.007	.933±.008
M.S.,C.R.,C.E.,Xhit,TDC Survey Misalignment	.840±.012	.887±.010

Table A.2: The Efficiency of the χ^2 Probability Cut for Simulated W muon decays as different simulated processes are included.

minimum bias simulation was described in Chapter 3. The minimum bias muons were selected using the inclusive cuts (also described in Chapter 3) with the exclusion of the $P(\chi^2)$ cut. In addition, the muons were required to have a strip pad signal (ADC counts > 1000) in the $\eta - \phi$ tower associated with the muon in two of the three chamber planes as well as have an accompanying stub in the VTPC chambers with track matching parameters satisfying $|\theta_{fmu} - \theta_{vtpc}| < 1.5^\circ$ and $|\phi_{fmu} - \phi_{vtpc}| < 15^\circ$. To select on minimum bias decays, the events were required to have the maximum jet cluster $E_t < 6\text{GeV}$. Figures A.2a-f show the distributions for the track cut variables for the minimum bias events selected using the above requirements.

To demonstrate the difficulties of misidentification of muons with very soft momentum, Figure A.3a shows a $P_t(\text{fitted})$ vs $P_t(\text{generated})$ scatter plot for simulated minimum bias muons. From this figure, we see that most of the muons with fitted $P_t > 20\text{GeV}/c$ are in fact mismeasured muons with generated $P_t < 4\text{GeV}/c$. This is primarily due to wide angle Moliere scatters. These muons multiply scatter into the trigger road and are then accepted by the forward muon trigger. The main difference between these misreconstructed tracks and prompt high P_t muons is the χ^2 of the fit which is predominately larger the mismeasured muons. To support this claim, Figure A.3b shows the χ^2 distribution of events with reconstructed $P_t > 20\text{GeV}/c$ and simulated $P_t < 4\text{GeV}/c$. As shown in this figure, the χ^2 distribution for these events is very broad. Figure A.3c shows the χ^2 distribution of the simulated minimum bias data compared to the CDF 88-89

minimum bias data. Also shown in this figure is the theoretical normal χ^2 distribution. The distributions are arbitrarily normalized to each other. While the Z^0 data closely matched the normal χ^2 distribution, the minimum bias distribution follows the broad distribution predicted due to mismeasured soft muons. The comparison of the $P(\chi^2)$ distribution is shown in Figure A.3d. The simulated distribution is normalized to the number of events in the data distribution. The large enhancement in the first bin is due to the much broader χ^2 distribution.

Shown in the columns of Table A.3 are the fraction of events with $P(\chi^2) > .02$ for data and monte carlo as a function of the P_t of the muon. The rows of Table A.3 show how this number changes as the generated minimum muon P_t is increased. This table qualitatively shows a difference between data and monte carlo for the fraction of events passing $P(\chi^2) > .02$. As can be seen, however, there is a strong dependence on the minimum P_t of muons in the simulation. The lowest muon momentum able to traverse the toroids is $P = 5\text{GeV}/c$. This corresponds to $P_t^{\theta=8}(\text{min}) = .7\text{GeV}/c$ and to $P_t^{\theta=16}(\text{min}) = 1.38\text{GeV}/c$. (Due to constraints on the available computer time, the lowest muon P_t used in the simulation was $2\text{GeV}/c$.)

Looking at Table A.3, one notices that once the minimum muon P_t is increased above $P_t > 6\text{GeV}/c$, the minimum bias $P(\chi^2)$ efficiency reaches a value consistent with the FMU-CMU Z^0 $P(\chi^2)$ efficiency. This indicates that while the overall minimum bias $P(\chi^2)$ efficiency is strongly degraded due to mismeasured muons, the efficiency for selecting muons with true P_t 's above a threshold of $6\text{GeV}/c$ is similar for minimum bias and Z^0 decay muons.

In addition to the strong dependence on the minimum muon P_t used in the simulation, the minimum bias $P(\chi^2)$ efficiency is also dependent on the power spectrum used. As shown in Chapter 4, the minimum bias power spectrum for isolated muons is softer than the CDF published value. (Isolation was determined by muons passing $\Sigma E_t(R = .7) < 5\text{GeV}$ where $\Delta R = \sqrt{\Delta\phi_{mu-jt}^2 - \Delta\eta_{mu-jt}^2}$) The CDF published minimum bias is proportional to $C/(1.3 + P_t)^{8.28}$ whereas the isolated minimum bias spectrum is proportional to $C/(1.3 + P_t)^{9.0}$ for C a constant. The dependence on spectrum shape in the $P(\chi^2)$ efficiency is demonstrated in Figure A.4 where the $P(\chi^2)$ efficiency is plotted as a function of minimum muon $P_t(\text{measured})$ for several spectrum shapes.

As shown in this figure, the softer spectrums predict lower $P(\chi^2)$ fractions. This is because in the softer spectrums events with lower P_t are given more weight and it is these softer muons which are more frequently mismeasured. Because of the strict requirement of no jets used to select the minimum bias data used here (largest jet cluster must satisfy $E_t < 6\text{GeV}$), the spectrum shape for the data events is assumed to be different from the CDF published power spectrum used in the monte carlo, possibly even softer than the isolated power spectrum of $C/(1.3 + P_t)^{9.0}$.

Finally, the $P(\chi^2)$ efficiency is also slightly dependent on the multiple scattering and production of extra hits modeled in the monte carlo. The size of this dependence is shown in Figure A.5 for different extra hit and scattering models. (Recall from Chapter 4 that the Moliere scattering model is known to over

estimate the number of wide angle scatters.)

In conclusion, the minimum bias simulation predicts $P(\chi^2)$ efficiencies which are greatly degraded due to contamination of mismeasured muons. The absolute value of this efficiency is strongly dependent on the modelling parameters used in the monte carlo and for this reason, cannot be precisely compared to data. From a qualitative comparison however, the monte carlo shows that once the simulated minimum muon P_t is increased above $P_t=6\text{GeV}/c$, the minimum bias $P(\chi^2)$ efficiency reaches a value consistent with the simulated FMU-CMU Z^0 $P(\chi^2)$ efficiency.

A.4 Muon-In-Jet Data Compared to Simulation

Finally, the muon in jet data set (presumably, largely enhanced with bottom and charm decays) is studied. Since the P_t distribution for bottom and charm decay is harder than that of minimum bias events, an absolute comparison to the minimum bias spectrum is not fair. A sample of clean muons in jets were selected using the inclusive cuts (as described in Chapter 3) with the exclusion of the $P(\chi^2)$ cut. In addition, the muons were required to have a strip pad signal (ADC counts > 1000) in the $\eta - \phi$ tower associate with the muon in two of the three chamber planes as well as have an accompanying stub in the VTPC chambers with track matching parameters satisfying $|\theta_{fmu} - \theta_{vtpc}| < 1.5^\circ$ and $|\phi_{fmu} - \phi_{vtpc}| < 15^\circ$. To select on muon-in-jet events, the muons were required to satisfy $\Delta R < .6$ as

$P(\chi^2) > .02$ Fraction				
	CDF 88-89 MB Data	Sim MB generated $P_t > 2$	Sim MB generated $P_t > 6$	Sim MB generated $P_t > 10$
measured $P_t > 6$.415±.014	.673±.003	.878±.003	.887±.009
measured $P_t > 8$.358±.017	.596±.004	.864±.004	.888±.009
measured $P_t > 10$.263±.020	.490±.005	.825±.007	.881±.010
measured $P_t > 12$.200±.022	.398±.006	.785±.011	.869±.013

Table A.3: The fraction of event passing $P(\chi^2) > .05$ both as a function of the measured muon P_t and as a function of the generated P_t for minimum bias events.

well as require the maximum jet cluster $E_t > 10\text{GeV}$. Figures A.6a-f show the distributions for the track cut variables for the muon-in-jet events selected using the quality cuts described above.

Shown in the columns of Table A.4 are the $P(\chi^2) > .02$ efficiencies for the muon-in-jet data set as a function of the measured muon P_t . As in the minimum bias simulation, an absolute comparison of the $P(\chi^2)$ efficiency is not correct since the two spectrum shapes are presumably different due to the jet requirement in the data. The muon-in-jet data qualitatively agree with the simulation, with the data actually showing a larger $P(\chi^2)$ efficiency than predicted by the monte carlo. This most likely indicates that the presence of the jet E_t cut in the data acts like a minimum muon P_t cut thus eliminating the softer muons which are more likely to be mismeasured.

Also shown in the Table are the efficiencies for the $P(\chi^2)$ cut once a minimum simulated muon P_t is required. From the table, we see the bottom and charm $P(\chi^2)$ efficiency values for muons above $P_t > 6\text{GeV}/c$ are very similar to the $P(\chi^2)$ efficiencies of both minimum bias muons with simulated $P_t > 6\text{GeV}/c$ and of the FMU-CMU Z^0 decay muons.

A.5 Conclusion

In conclusion, the forward muon track fitting algorithm is able to reproduce the tails in the FMU-CMU Z^0 χ^2 distribution using known effects. There is some

$P(\chi^2) > .02$ Fraction				
	CDF 88-89 Mu-in-jet Data	Sim No $P_t(\text{gen})$ Min cut	Sim $P_t(\text{gen}) > 4\text{GeV}/c$	Sim $P_t(\text{gen}) > 4\text{GeV}/6$
measured $P_t > 6$	$.826 \pm .018$	$.804 \pm .004$	$.835 \pm .004$	$.863 \pm .004$
measured $P_t > 8$	$.832 \pm .021$	$.797 \pm .005$	$.831 \pm .005$	$.860 \pm .005$
measured $P_t > 10$	$.803 \pm .028$	$.757 \pm .008$	$.806 \pm .007$	$.845 \pm .007$
measured $P_t > 12$	$.780 \pm .038$	$.696 \pm .010$	$.761 \pm .010$	$.812 \pm .010$

Table A.4: The efficiency of the $P(\chi^2)$ probability cut as a function of the measured muon P_t for both triggered and volunteer muon in jet events.

indication that the tails in the Z^0 data are larger than the monte carlo, however this is not statically significant. The minimum bias data qualitatively agrees with the monte carlo. An absolute agreement in the $P(\chi^2)$ efficiencies is not possible due to the strong dependence on the minimum simulated muon P_t as well as due to the weaker dependence on spectrum power, multiple scattering and production of extra hits models used in the simulation. As the minimum muon P_t is raised, the $P(\chi^2)$ efficiency approaches a value that is consistent with the FMU-CMU $P(\chi^2)$ efficiency. The muon in jet data also qualitatively agrees with the simulation with the data showing a larger $P(\chi^2)$ efficiency than the monte carlo. This difference is consistent with the jet cut in the data acting like a minimum muon P_t cut. Furthermore, if the simulated muon P_t is required to be greater $P_t(\text{gen}) > 6\text{GeV}/c$, the efficiency also approaches the values predicted from the other simulated data sets.

Since we are interested in measuring muons whose initial $P_t > 6\text{GeV}/c$, the $P(\chi^2)$ efficiency for this signal is $.88 \pm .02$ as obtained from the three different muon studies.

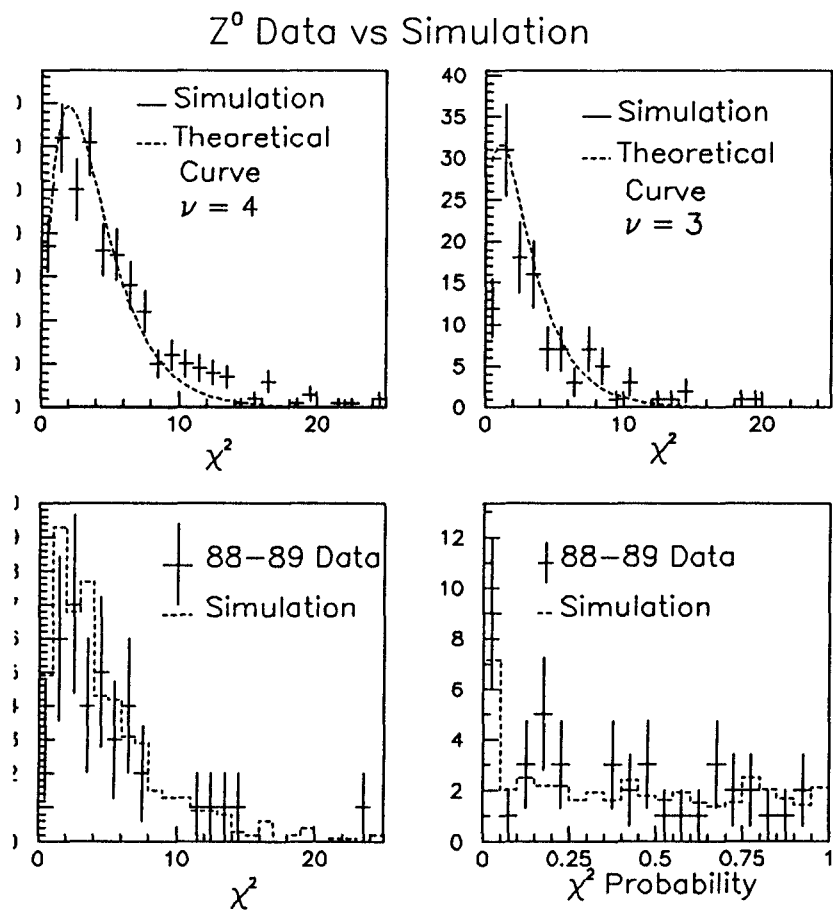


Figure A.1: The χ^2 distribution from the simulated data set of $Z \rightarrow \mu\mu$ a.) for 3 degrees of freedom. b.) for 4 degrees of freedom. A comparison between monte carlo and CDF 88-89 data c. χ^2 d. $P(\chi^2)$.

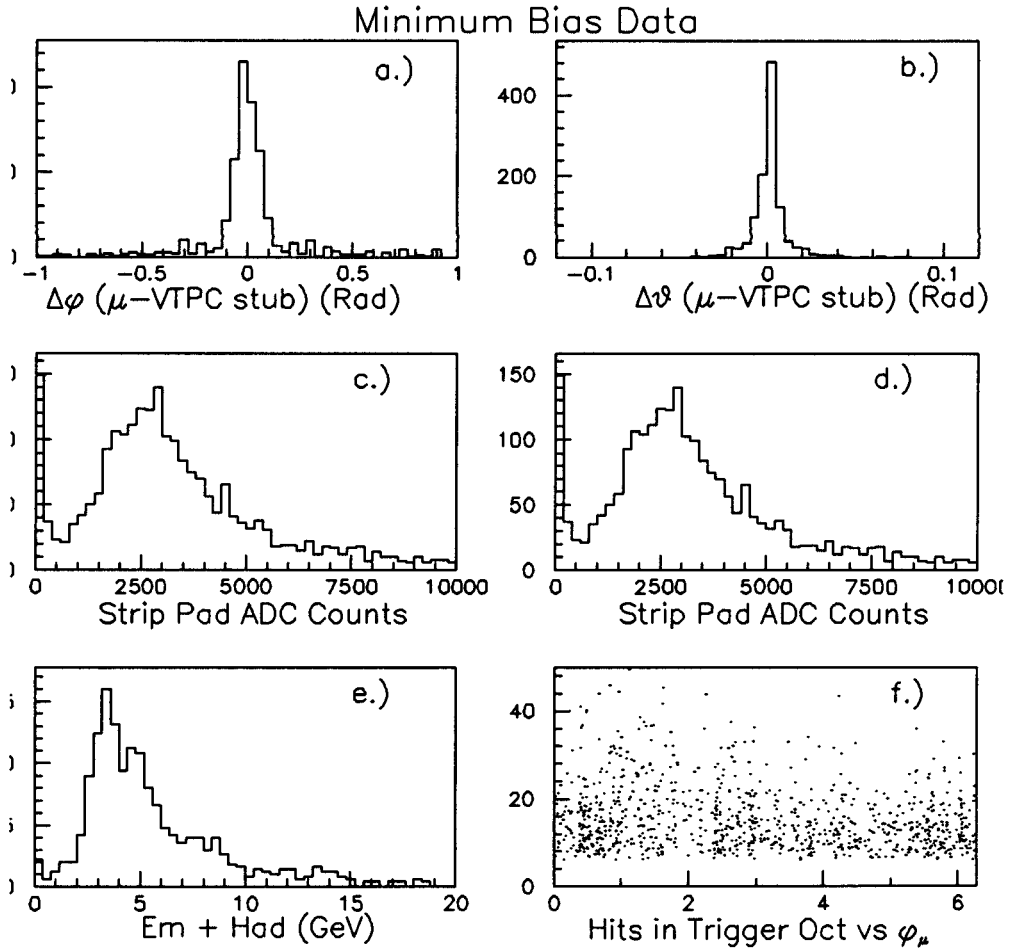


Figure A.2: Event Quantities for the CDF 88-89 Minimum Bias Data Set.

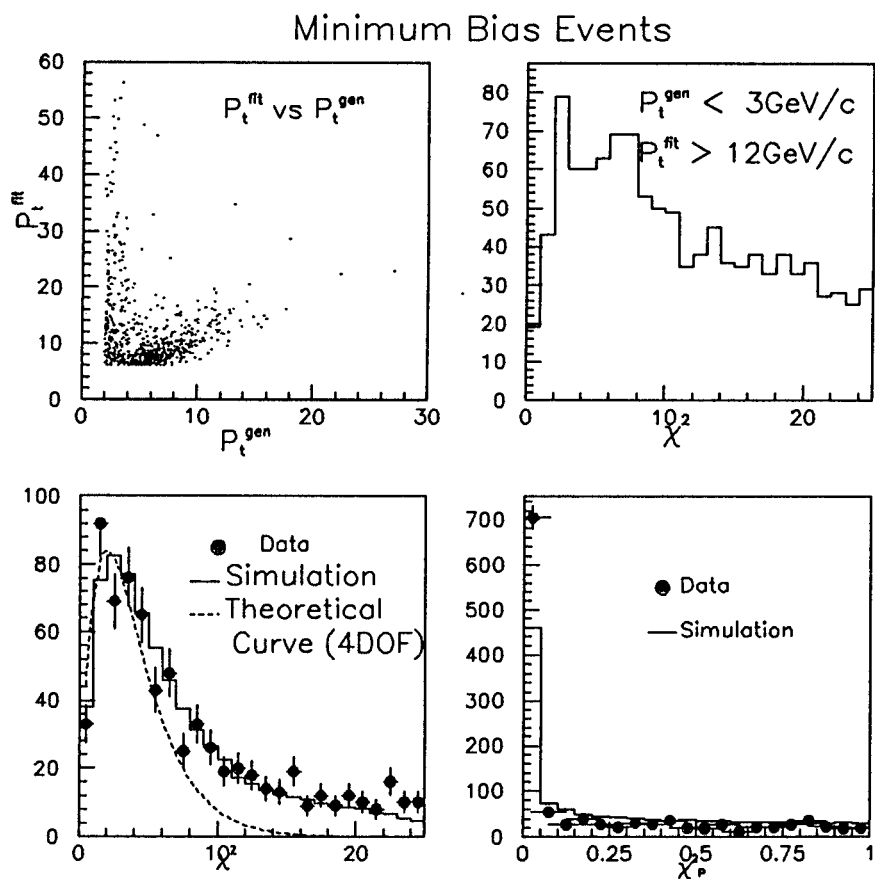


Figure A.3: The χ^2 distribution from the minimum bias simulated data a.) for 4 degrees of freedom. b.) for badly mismeasured events. A comparison between monte carlo and CDF 88-89 data c. χ^2 d. $P(\chi^2)$.

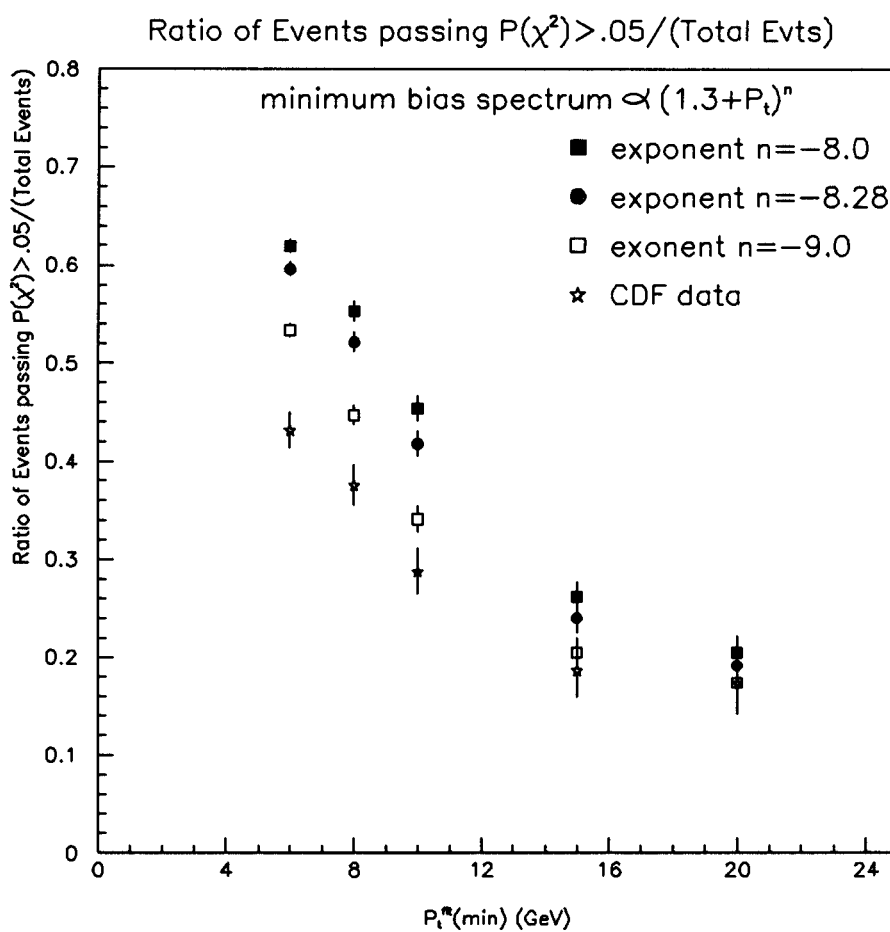


Figure A.4: Fraction of events passing the $P(\chi^2) > .05$ for different minimum bias spectrum shapes.

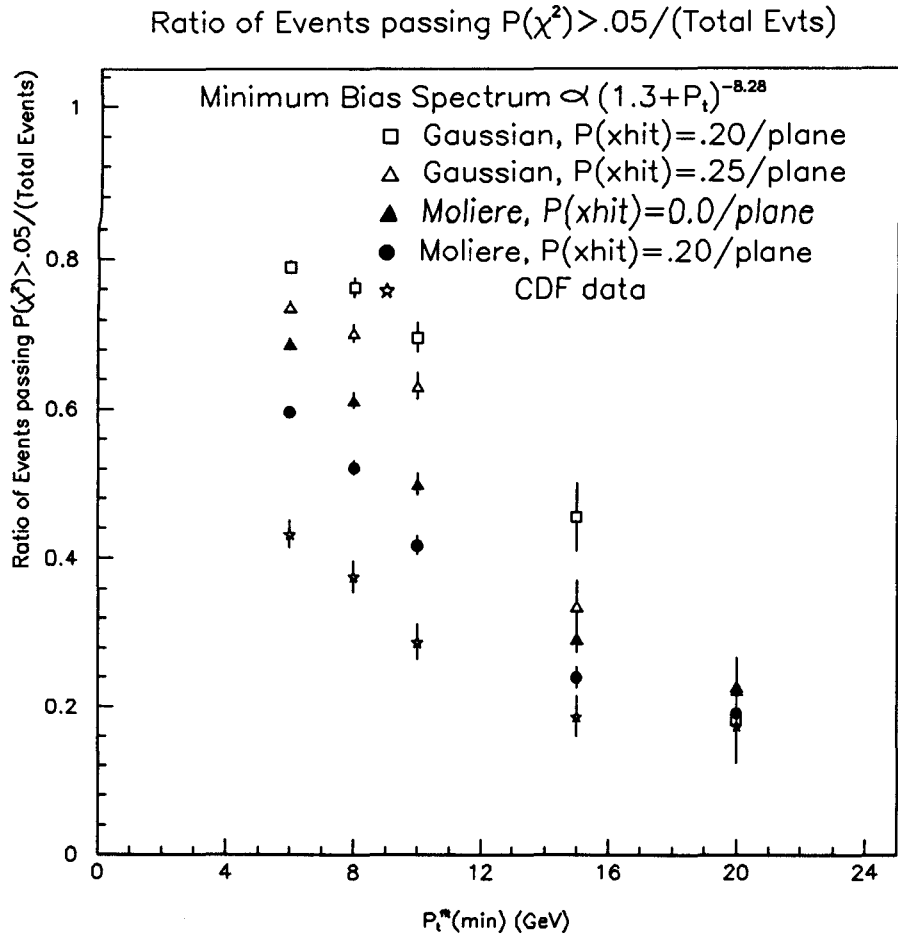


Figure A.5: Fraction of events passing the $P(\chi^2) > .05$ for different scattering and extra hit models.

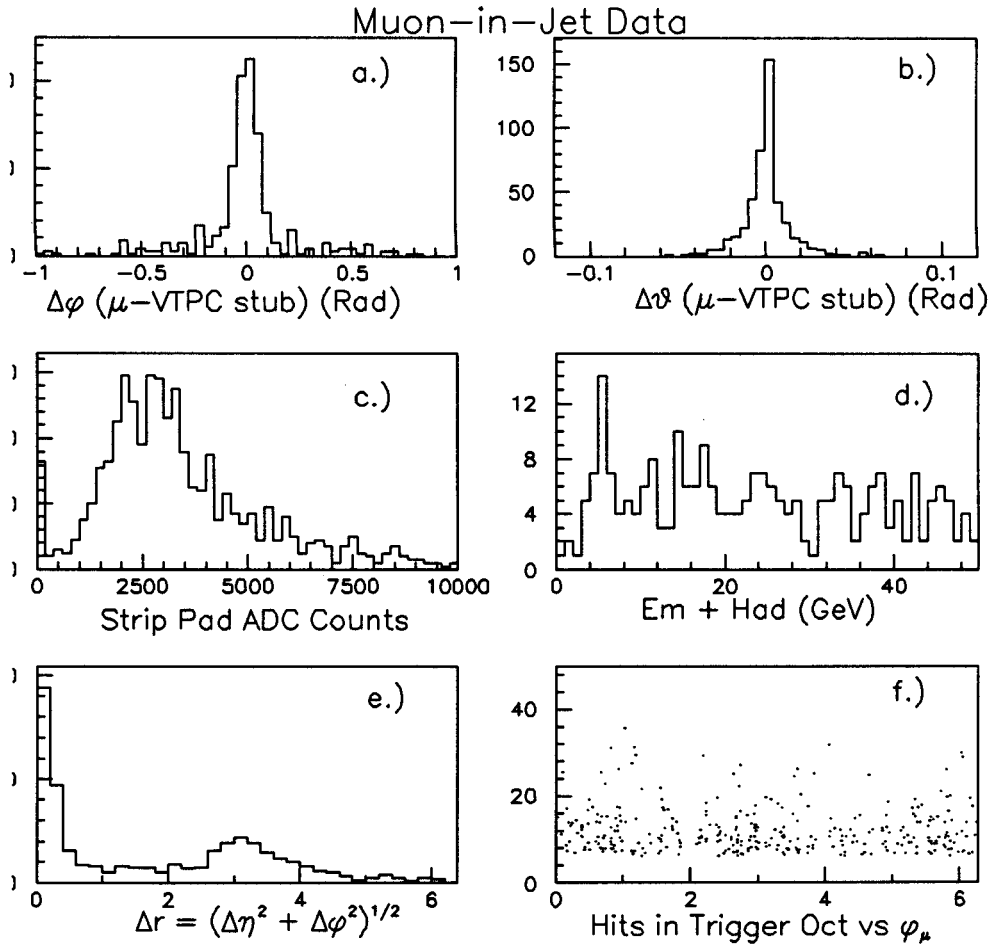


Figure A.6: Event Quantities for the CDF 88-89 Muon-in-Jet Data Set.

Appendix B

Delta rays, photon conversions, bremsstrahlung and other physics processes responsible for the production of extra hits in the FMU drift cells

A delta-ray electron accompanying a muon can cause an ambiguity in the muon hit position. Other physics processes such as photon conversions, bremsstrahlung or nuclear conversions can also leave an ionization signal in the muon chambers thus confusing identification of the true muon hit position. These extra hit

processes have been studied using a forward muon detector simulation with the GEANT Monte Carlo. [33] A parameterization was determined from the GEANT extra hit distributions for use in both CDFSIM and a faster forward muon Monte Carlo simulation program.

B.1 Origins

The extra hits that surround the muon's true hit position can be produced in one of two regions. They can be produced in the last 8 - 10 cm of the iron in either the toroids or forward calorimeter or they can be produced in the drift chamber walls. The distribution of extra hit vertex positions is shown in figure 2.1. The biggest peak in plots a.), c.), and d.) is due to the extra hits produced in the last 8-10 cm of the iron. The smaller double peaks are due to extra hits produced in the chamber walls. A double peak occurs because the chambers are staggered every 15° in ϕ to avoid detector dead spots in the azimuthal acceptance. Plot b.) shows the (x,y) vertex position for extra hits in the front plane which have originated prior to the last 10 cm of the rear calorimeter face. These extra hits were produced at the edges of the square forward calorimeter which is 200cm X 200cm in size. Essentially none of the extra hits reaching the forward drift cells have originated in the plug calorimeter. This is because the lever arm from the plug to the front plane of the drift cells is so large.

The momentum distribution for extra hits originating in the iron is harder

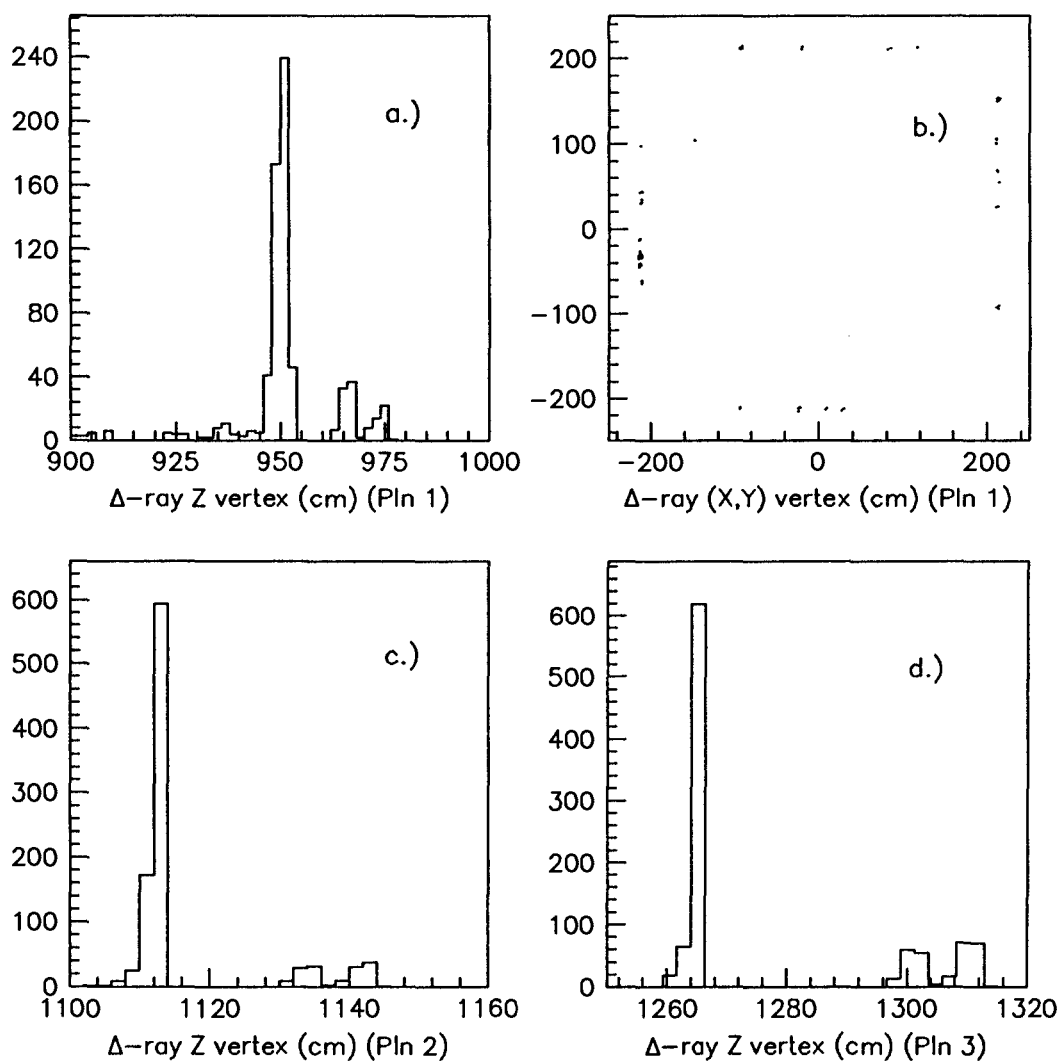


Figure B.1: Vertex Positions for Extra Hits in units of cm. a.) Front Plane Z positions. b.) Front Plane X,Y positions. c.) Mid Plane Z positions. d.) Rear Plane Z positions.

than for extra hits originating in the chamber walls. This is shown in figure 2.2. The fringe field at the front and rear plane chamber cells is about 25 Gauss and the field at the middle plane chamber cells is twice as large. The distance between the iron and the chamber cells varies depending on which plane is considered, but this distance is 10 - 18 cm for the front plane, 18 - 26 cm for the mid plane and 34 - 42 cm for the rear plane. Softer delta rays originating in the iron are thus swept away prior to reaching the drift cells.

Delta rays with a larger momentum can penetrate both the coordinate and the ambiguity drift cells to form a pair of hits that have matched hit positions. A correlated extra hit pair is thus more likely to confuse the tracking algorithm since there is a coordinate-ambiguity match requirement. A pair of uncorrelated hits (i.e. one uncorrelated hit in the coordinate cell and one uncorrelated hit in the ambiguity cell) are not likely to have similar hit positions and thus will fail the tracking algorithms coordinate-ambiguity match requirement. Table 2.1 lists the percentage of extra hits originating in the iron and at the chamber walls for both correlated and uncorrelated delta rays. As seen in this table, about 60% of the delta-rays are produced in the iron and penetrate both coordinate and ambiguity drift cells to produce a correlated extra hit pair.

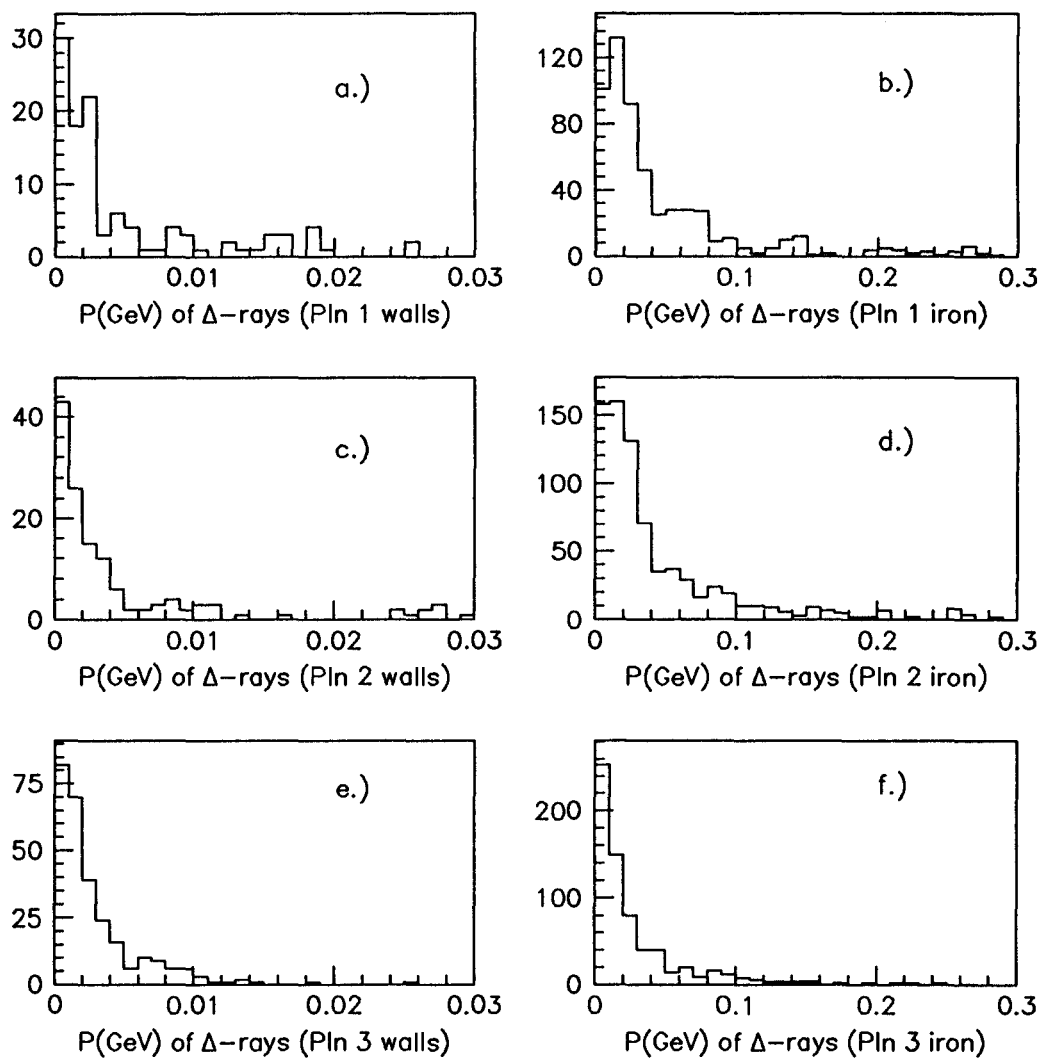


Figure B.2: Momentum distribution for extra hits originating in either the chamber walls (figures a., c. and e.) or the iron (figures b., d., and f.)

	Correlated Extra Hits	Uncorrelated Extra Hits
Iron	$59.8 \pm 1.1\%$	$6.2 \pm .5\%$
Chamber Wall	$8.6 \pm .6\%$	$25.3 \pm 1.0\%$

Table B.1: Percentage of extra hits which are correlated or uncorrelated produced in either the iron or in the chamber walls

B.2 Multiplicity Distributions

About 1000 minimum bias events generated using the GEANT monte carlo with a muon minimum p_t of 10 GeV/c were analyzed to provide plane multiplicity distributions as well as spatial distributions. The hit position of delta rays which ionized in the drift cells was recorded as well as the muon hit positions. The number of extra hits observed on each plane was also recorded. If more than one extra hit was found, pairs of hits were searched to identify correlated matches. A pair of hits were said to be correlated if they originated from the same vertex. If no correlated match could be found, the hit was labeled as uncorrelated.

Several tables were constructed. Table 2.2 lists the fraction of events that had a specified number of extra hits. This information is listed for each plane, however since these distributions do not differ between planes, the multiplicity distribution used for parameterization purposes was plane averaged. Table 2.3 lists the percentage of extra hits that were found to be correlated or uncorrelated.

Number of Extra Hits in Events	Plane 1 (%)	Plane 2 (%)	Plane 3 (%)
0	79.81±1.43	80.83±1.25	80.72±1.25
1	7.57±.84	8.88±.90	7.37±.83
2	7.16±.82	6.26±.77	7.06±.81
3	1.72±.41	1.31±.36	.71±.26
4	1.51±.39	1.11±.33	1.51±.39
5	.40±.20	.20±.14	.71±.26

Table B.2: Fraction of events that have extra hits

This percentage starts at 2 extra hits since one extra hit must be uncorrelated. The latter table is important because two extra hits which are correlated will have a very similar spatial distribution whereas uncorrelated hits will be random. Not listed in the table are the correlated percentages for 4 and 5 extra hits. These numbers were also computed. For example, in the case of 4 extra hits, you can have two pairs of correlated hits or you can have one correlated pair of hits and two uncorrelated hits or all four hits can be uncorrelated.

In the fast Monte Carlo, the multiplicity table was used to determine the number of extra hits to generate at each chamber plane for each muon track. If more than one extra hit was generated at a plane, the correlation tables were used to determine if the extra hits should be correlated or not.

No of Extra Hits	Correlated Plane Averaged (%)	Not Correlated Plane Averaged (%)
2	80.79±2.77	19.21±2.77
3	83.78±6.06	16.21±6.06

Table B.3: Fraction of extra hits that are correlated with other extra hits.

B.3 Spatial Distributions

B.3.1 $\Delta\phi$ Distributions

For generation of the spatial $\Delta\phi$ distribution between muon hits and delta rays hits, I use the approximation that the ϕ of the muon hit is the same as the ϕ of the delta ray. This is a good approximation as illustrated in figure 2.3. This figure shows the $\Delta\phi$ distributions for delta-rays which are both correlated and uncorrelated relative to the muon hit. The $\Delta\phi$ distribution between the coordinate hit relative to the ambiguity hit for a correlated delta-ray is also shown.

The approximation that $\Delta\phi = 0$. is further supported since the ϕ resolution of the muon chambers is $\pm 5^\circ$, ϕ differences of an amount less than this are not resolved by the chambers. Also, since the toroidal field is in the R direction, extra hits in the ϕ direction should not confuse the tracking algorithm in its momentum

determination.

B.3.2 ΔR Distributions

Finally, the Δr spatial distributions for the correlated and uncorrelated extra hits are plotted in figure 2.4. To determine the radial distance between the delta-ray hit and the muon hit position, three cases were considered. Case one determined the spatial distribution of an uncorrelated delta-ray hit relative to a muon hit. The second case determined the distribution of a correlated delta-ray hit relative to the muon hit position and the third case determined the position of the correlated delta-ray on the ambiguity plane relative to the correlated delta ray on the coordinate plane. These distributions were plotted for each plane separately and then fit to the functional forms which were combinations of gaussian and second order polynomial distributions.

The parameters to the functional forms used are shown in table 2.4. The functional form used in the spatial fit of ΔR between a correlated hit in the coordinate cell to a correlated hit in the ambiguity cell was

$$\begin{aligned} \Delta R = & \frac{c1}{c3} e^{-(\Delta R - c2)^2 / 2c3^2} \\ & + \frac{c4}{c6} e^{-(\Delta R - c5)^2 / 2c6^2} \end{aligned} \quad (\text{B.1})$$

The functional form used for the other parameterizations, namely ΔR between a correlated extra hit in the coordinate cell and the muon, and ΔR between an

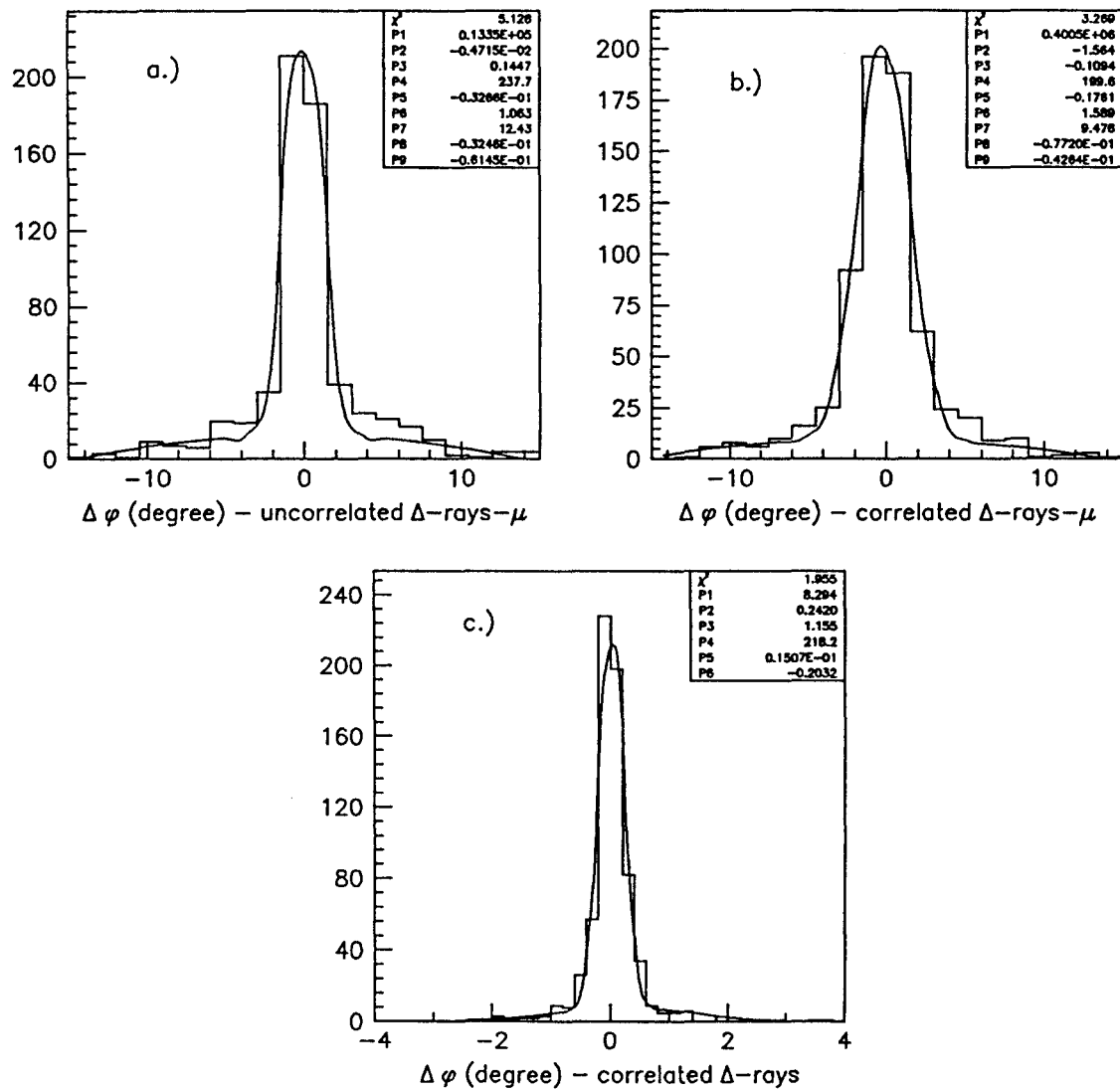


Figure B.3: a.) $\Delta\phi$ between uncorrelated delta-ray and muon hit. b.) $\Delta\phi$ between correlated delta-ray and muon hit. c.) $\Delta\phi$ between correlated coordinate delta-ray hit and ambiguity delta-ray hit.

uncorrelated extra hit in either cell and the muon, was

$$\begin{aligned} \Delta R = & \frac{c1}{c3} e^{-(\Delta R - c2)^2 / 2c3^2} \\ & + \frac{c4}{c8} e^{-(\Delta R - c5)^2 / 2c6^2} \\ & + c7 + c8\Delta R + c9\Delta R^2 \end{aligned} \quad (\text{B.2})$$

The plane to plane distributions were the same within errors so that a plane averaged distribution was used for the final parameterization.

Each functional form was analytically integrated from -20cm to 20cm and this value was used as a normalization to construct a probability table. The probability table was computed using the following equation.

$$P(\Delta R) = \frac{\int_{-20}^{\Delta R} FF}{\int_{-20}^{+20} FF} \quad (\text{B.3})$$

where FF is one of the functional forms. A random number was then used in conjunction with the probability table to determine the spatial distribution of an extra hit. The tails of several of the spatial distributions extended beyond ± 20 cm, however this contribution was small.

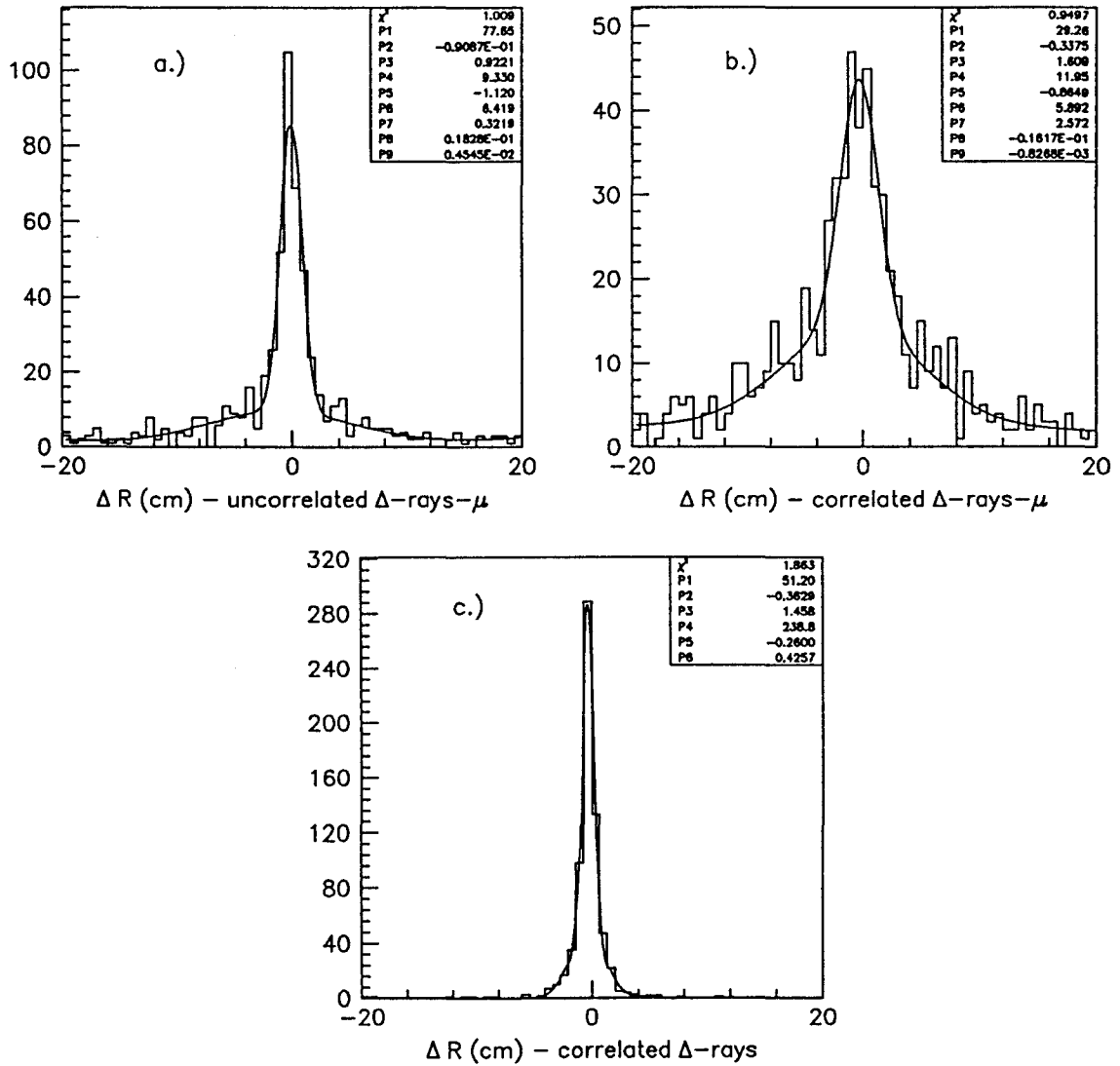


Figure B.4: a.) Δr between uncorrelated delta-ray and muon hit. b.) Δr between correlated delta-ray and muon hit. c.) Δr between correlated coordinate delta-ray hit and ambiguity delta-ray hit.

	Case 1	Case 2	Case 3
Fit Parameters	$x=g+g+p^2$	$x=g+g+p^2+p^2$	$x=g+g$
χ^2	1.009	.9497	1.863
no points in fit	51	54	20
c1	77.65	29.26	51.2
c2	-.091	-.34	-.36
c3	.92	1.61	1.45
c4	9.33	11.95	238.8
c5	-1.12	-.86	-.26
c6	6.42	5.89	.43
c7	.32	2.57	-
c8	.018	-.016	-
c9	.0045	.0008	-

Table B.4: Parameterization of equations describing the radial spatial distributions for the 3 cases mention above.

Appendix C

The Predicted Decay in Flight Spectrum

C.1 The FMU Decay In Flight Normalization

[23] The number of muons originating from pions and kaons is calculated using the CDF published minimum bias spectrum [35]. This distribution is based on the inclusive spectrum of charged hadrons produced in the eta region $|\eta| < 1.0$ and is given by

$$E \frac{d^3\sigma}{d^3P^h} = \frac{A}{(1 + P_t^h/P_o)^n} \quad (\text{C.1})$$

The parameters of the fit to this spectrum are given by $A = .45 \pm .01 \times 10^{-24} \text{ cm}^2 \text{ c}^3/\text{GeV}^2$, and $n = 8.28 \pm .02$. A fixed value of $P_o = 1.3$ was also used.

It is convenient to express this Lorentz invariant differential in terms of the

rapidity variable, Y .

$$E \frac{d^3\sigma}{d^3P^h} = c \frac{d^3\sigma}{dY d^2P_t^h} \quad (\text{C.2})$$

To match the absolute normalization and shape of the inclusive charged muon spectrum, equation C.1 is multiplied by a factor of 2 to account for both charges of hadrons. Another factor of .83 is introduced since we are considering hadrons produced in .83 units of rapidity. The inclusive muon spectrum is expressed as follows

$$\sigma_{h \rightarrow \mu} = \frac{1.66}{c} \int \int \int \frac{AP_t^h}{(1 + P_t^h/P_o)^n} \epsilon_1^h(P_t^h, \theta) \epsilon_2^h \epsilon_3^h dP_t^h dY d\phi \quad (\text{C.3})$$

where ϵ_1^h is the hadron decay probability, ϵ_2^h is the hadron branching ratio to muons and ϵ_3^h is the hadron species composition percentage in the charged hadron spectrum.

The hadron decay probability, ϵ_1^h , is given by

$$\epsilon_1^h(P_t^h, \theta) = 1 - e^{X/\lambda} \quad (\text{C.4})$$

where X is the distance the hadron travels and λ is the decay constant given by $\lambda = \gamma\beta c\tau = \beta P^h\tau/m^h$. At the energies of the $p\bar{p}$ collider, $\beta = 1$. The ratio $X/c\tau \approx 1$ as shown in table C.1. The ratio $m^h/P^h \ll 1$ since the muons require at least 5 GeV/c of momentum in order to penetrate the forward toroids. ϵ_1^h is therefore approximately equal to

$$\epsilon_1^h(P_t^h, \theta) \approx \frac{m^h X \sin \theta}{P_t^h \tau} \quad (\text{C.5})$$

hadron	mass	$c \tau$	X	ϵ_2^h	ϵ_3^h
	(GeV/C ²)	(cm)	(cm)	(%)	(%)
pion	.1396	780.3	710.	1.00	.58±.12
kaon	.4936	370.9	220.	.6351±.0016	.21±.04

Table C.1: Constants used in the decay in flight formula.

ϵ_2^h is the hadron branching ratio to muons. This branching ratio is known to be 100 % for $\pi \rightarrow \mu$ and 63.51±.16% for kaons $\rightarrow \mu$. [3]

The hadron charged particle composition for minimum bias events, ϵ_3^h , is best estimated to contain 58±12.% pions, 21±4% kaons and 26% protons. [48], [23]

The inclusive charged muon spectrum can now be written

$$\sigma_{h \rightarrow \mu} = \frac{1.66A}{c} \epsilon_2^h \epsilon_3^h \int \int \frac{P_t^h m^h X \sin \theta dP_t^h d\phi dY}{(1 + P_t^h/P_o)^n P_t^h \tau} \quad (\text{C.6})$$

The phi integration of equation C.6 is simple since there is no phi dependence.

$$\int d\phi = 2\pi$$

By making a change of variables, the eta integration can also be simplified.

$$\begin{aligned} Y &= \tanh^{-1}\left(\frac{P_z}{E}\right) \\ &= \tanh^{-1}\left(\frac{P_t \cot \theta}{\sqrt{(P_t/\sin \theta)^2 + m^2}}\right) \end{aligned} \quad (\text{C.7})$$

For particles where $m \ll E$ which is true for the charged hadrons at the energies we are considering, $Y = \eta$ and then equation C.7 becomes

$$\eta \approx \tanh^{-1}(\cos \theta) \quad (\text{C.8})$$

so that $d\eta$ is simply:

$$d\eta = \frac{d\theta}{\sin \theta}$$

Using this change of variables, equation C.6 becomes

$$\sigma_{h \rightarrow \mu} = \frac{3.32\pi Am_h}{c\tau_h} \epsilon_2^h \epsilon_3^h \int d\theta X \int \frac{dP_t^h}{(1 + P_t^h/P_o)^n} \quad (\text{C.9})$$

In the angular region $7^\circ < \theta < 10^\circ$, the calorimeter is located at 710 cm from the interaction point, while in the angular region $10^\circ < \theta < 16^\circ$, the calorimeter is located at 220 cm from the interaction point. The distance a hadron travels, X , therefore depends on which calorimeter it points at. The $d\theta$ integral is determined by treating the two regions separately.

$$\begin{aligned} \int X d\theta &= 2 * \left(\int_{7^\circ}^{10^\circ} 710\text{cm} d\theta + \int_{10^\circ}^{16^\circ} 220\text{cm} d\theta \right) \quad (\text{C.10}) \\ &= 2 * (710\text{cm} * 3^\circ + 220\text{cm} * 6^\circ) \frac{\pi}{180^\circ} \\ &= 120\text{cm-rad} = \Psi(X) \end{aligned}$$

The factor of 2 is required to include both the forward and backward muon regions.

At each possible P_t^h value, the muon can assume some fraction of P_t^h . The range of values depends on the specific parent hadron. The muon P_t distribution is flat between the kinematic limits $aP_t^h < P_t^\mu < bP_t^h$ where the constants a and b are defined

$$\pi \rightarrow \mu = .57P_t^h < P_t^\mu < P_t^h$$

$$K \rightarrow \mu = .05P_t^h < P_t^\mu < P_t^h \quad (\text{C.11})$$

To model the muon P_t^μ , the P_t^h integral of equation C.9 can be written as follows

$$\int \frac{dP_t^h}{(1 + P_t^h/P_o)^n} = \int dP_t^\mu \int_{P_t^\mu/a}^{P_t^\mu/b} \frac{dP_t^h}{(b-a)P_t^h(1 + P_t^h/P_o)^n} \quad (\text{C.12})$$

where a and b are the allowed muon maximum and minimum P_t^h percentage given by equation C.11.

The exact form of equation C.12 is derived as follows [24]. Suppose you have a monochromatic pion beam from which all the pions decay to muons. Then

$$\frac{d\sigma}{dP_t^h} = \delta(P_t^h - x)\alpha$$

$$\sigma = \int dP_t^h \frac{d\sigma}{dP_t^h} = 1 \quad (\text{C.13})$$

$$(\text{C.14})$$

where x is the transverse energy of the hadron and σ is the total cross section. α is a constant equal to 1 in units of cm^2s/GeV . Since the muon distribution is flat over the region $ax < P_t^\mu < bx$, $d\sigma/dP_t^\mu$ can be written as

$$\begin{aligned} \frac{d\sigma}{dP_t^\mu} &= \frac{\sigma\theta(P_t^\mu/ax - ax)\theta(bx - P_t^\mu)}{P_t^\mu(Max) - P_t^\mu(Min)} \\ &= \frac{\theta(P_t^\mu - ax)\theta(bx - P_t^\mu)}{x(b-a)} \end{aligned} \quad (\text{C.15})$$

where the θ functions define the range over which the muon P_t^μ is allowed and the $1/(x*(b-a))$ coefficient is determined by requiring the integral to equal 1.

If the pion spectrum is modeled as a superposition of δ -functions over all transverse energies, the actual muon spectrum can be obtained. We start with

the general expression

$$\frac{d\sigma}{dP_t^h} = f(P_t^h) = \int dx f(x) \delta(P_t^h - x) \quad (\text{C.16})$$

where the function $f(P_t^h)$ is described by the minimum bias fit to the inclusive charged hadron spectrum. The muon spectrum can then be written as

$$\sigma_{h \rightarrow \mu} = \int dP_t^\mu \int_{P_t^\mu/b}^{P_t^\mu/a} dP_t^h f(P_t^h) \frac{1}{P_t^h(b-a)} \quad (\text{C.17})$$

For the minimum bias spectrum, $f(P_t^h) = 1/(1 + P_t^h/P_0)^n$. Therefore, combining equations C.9 and C.12 gives for the final inclusive charged muon spectrum

$$\sigma_{h \rightarrow \mu} = \frac{3.32\pi A m_h \Psi(X) \epsilon_2^h \epsilon_3^h}{c\tau_h(b-a)} \int_{P_t^\mu(\min)}^{\infty} \int_{P_t^h/b}^{P_t^h/a} \frac{dP_t^h}{P_t^h(1 + P_t^h/P_0)^n} \quad (\text{C.18})$$

The integrals are evaluated numerically. Table C.2 shows the computed cross section for muons into the forward detector for various $P_t^\mu(\min)$ values.

To determine the expected number of decay-in-flight muons, the cross section's of table C.2 are multiplied by the integrated luminosity into the forward muon detector. The integrated luminosity into the FMU system was $1733 \pm 260 (nb)^{-1}$.

C.2 The FMU $d\sigma/dP_t^\mu$ Distribution

To simulate the resultant muon P_t spectrum with detector effects, an integral probability table was constructed using the normalizations in Table C.2. Each probability table was constructed by solving the normalized integral equation

$$F(x) = \frac{\int_{x_{\min}}^x f(x') dx'}{\int_{x_{\min}}^{\infty} f(x') dx'} \quad (\text{C.19})$$

$P_t^\mu(\text{min})$	σ_π	σ_K	σ_{Tot}
$\langle \text{GeV}/c \rangle$	(nb)	(nb)	(nb)
1	79020.	65063.	144083.
2	4681.0	3744.0	8425.
5	35.223	27.751	62.974
10	.46289	.36318	.82607
20	.004388	.003436	.007824

Table C.2: Integral inclusive cross section for various P_t^μ thresholds.

where $\int_{x_{min}}^{\infty} f(x')dx'$ is the P_t integral of equation C.18, which is just the inclusive charged P_t spectrum.

By definition, $dF(x)/dx = f(x)$. A common Monte Carlo technique uses this in conjunction with a random number to generate the preferred spectrum. By letting $F(x)$ equal the random number and $f(x)$ equal the inclusive charged muon P_t spectrum, then a change in the random number is defined by the shape of the inclusive charged muon P_t spectrum. The inclusive charged muon probability table was created in this way. In practice, the probability table of charged muons produced from kaons was added to the probability table of charged muons produced from pions.

C.3 The FMU $d\sigma/d\theta$ Distribution

As shown in equation C.11, the θ dependence in the inclusive muon distribution is flat with the forward calorimetry region weighted more than the plug calorimetry region. The weighting difference is proportional to the average distance a hadron travels times the θ interval of the region. The average distance a hadron travels, X , is defined as the length to the front face of the electromagnetic calorimeter plus one interaction length. (One interaction length is the distance in a material where the flux of hadrons is reduced to $1/e$ of its original value.) The electromagnetic calorimeters were designed to be one interaction length so that the distance X is equal to the distance to the front face of the hadron calorimeter.

Bibliography

- [1] A.Martin,R.Roberts,W.Stirling *Modern Physics Letters A Vol.4, No.12 (1989) 1135-1142*
- [2] E.L.Berger,F.Halzen,C.S.Kim,and S.Willenbrock. *Physical Review D, Vol 40, No. 1, 7-89.*
- [3] Particle Properties Data Book *from "Review of Particle Properties, Phys. Lett. B204, 88*
- [4] C.Campagnari *25th International Conference on Physics, Singapore 1990*
- [5] D. Decamp, et al. *Phys. Lett. B235, 399*
- [6] G Arnison et al. *Phys. Lett. 122B, (1983) 103*
- [7] M.Dobayashi and T. Maskawa *Prog. Theor. Phys. 49 (1973) 652.*
- [8] F. Halzen, A. Martin *"Quarks and Leptons" John Wiley and Sons, 1984*
- [9] E.Eichten,I.Hinchliffe,K.Lane and C.Quigg *Rev. Mod. Phys. Vol 56, pg. 579 (1984)*

- [10] P.N.Harriman,A.D.Martin,W.J.Stirling and R.G.Roberts *DTP/90/04 and RAL/90/007* (1990)
- [11] V.Barger, Phillips *Collider Physics*. Addison-Wesley Publishing Company, (1987)
- [12] "A Measurement of the Spin Asymmetry and Determination of Structure Functions $G(1)$ in DIMuon-Proton Scattering" *Phys. Lett. B206. (1988) 206*.
- [13] T. Muller CERN-EP/88-48 *Production Properties of the Intermediate Vector Bosons W and Z at the CERN $p\bar{p}$ Collider*
- [14] UA2 Collaboration *Phys. Lett. B194: 158 (1987)*
- [15] J.Kubar,M.Bellac,J.Meunier and G.Plaut *Nuclear Physics B175 (1980) 251-275*
- [16] W.J.Stirling *Plot produced by Stirling during private conversation.*
- [17] F.Snider et.al The Cdf Vertex Time Projection Chamber System *Nuclear Instruments and Methods, A(268) 1988,75-91.*
- [18] C.Grosso-Pilcher,S.White CDF-1202 *CDF Luminosity Calibration*
- [19] L.G. Pondrom. *SSC/LHC Muon Detectors Workshop Madison, Wisconsin (April 1984).*
- [20] K.Byrum, et el. *NIM A268 (1988) 46-49, The Cdf Forward Muon System*

- [21] D.Carlsmith, et.al.; *CDF-518 (1987) unpublished.*
- [22] K.Byrum, et. al. CDF-1343 *Forward Muon Chamber Efficiency, Gain and Resolution Studies.*
- [23] J.Skarha *Ph.D. Thesis.*
- [24] C.Wendt. *Author of Fast Monte Carlo.*
- [25] K.Byrum,J.Lamoureux. CDF-1594 *The Forward Muon Inclusive Spectrum.*
- [26] J.Lamoureux,K.Byrum CDF-1597 *Forward Muon Detector Efficiency for the 1988-89 Run.*
- [27] C.Wendt *Private Conversations*
- [28] J.Lamoureux *Ph.D. Thesis unpublished.*
- [29] Physical Review Letters *Vol 64, pgs 991-994*
- [30] Physical Review D *Vol 40, pgs 3791-3794*
- [31] S.Eno,D.Smith,C.Newmann-Holmes *Unpublished Combined Boson Cross Sections, Ewk Meeting 11-Jul-1991.*
- [32] P.Nason,S.Dawson,R.K.Ellis *Nuclear Physics, B327 (1989) pg 49-92*
- [33] J. Bellinger. *FMU simulation using GEANT.*
- [34] D. Carlsmith *FMU Review to godfather committee.*

- [35] F.Abe, et al. *Physical Review Letters*, Vol 61, No. 16 10-88.
- [36] F.Abe et al. (CDF Collaboration) in *Pseudorapidity Distribution of Charge Particles Produced in $p\bar{p}$ Interactions at $\sqrt{s} = 630$ and 1800 GeV*, *Phys. Rev Lett.*
- [37] A.Para *Unpublished Figure from minimum bias studies.*
- [38] Wicklund et. al, *Measuring the Bottom Quark Cross Section Using the Inclusive Electrons*, *CDF Note-1253*
- [39] L.Markosky *Private communication.*
- [40] S.Edner, et.al. CDF-1279 *Search for $W \rightarrow \mu\nu$*
- [41] C.Wendt *These plots are produced by C.Wendt.*
- [42] J.Hauser *Plots produced by code from J.Hauser*
- [43] I.Hinchliffe *Papageno Monte Carlo, version 3.30*
- [44] P.Schlabach *W Mass Measurement with Muons at $\sqrt{s}=1.8$ TeV; Ph.D. Thesis 1990.*
- [45] S.Leone Masters Thesis *INFN, Sezione di Pisa August 1990*
- [46] F.Abe, et. al *"Lepton Asymmetry in W decays from $p\bar{p}$ Collisions at $\sqrt{s} = 1.8$ TeV" Submitted to Phys. Rev. Lett, 9-91.*

- [47] S.Sogawa *Ph.D. Thesis, to be published.*
- [48] T.Alexopoulos et.al 1990 *Physical Review Letters Vol64, No 9 991-994*
- [49] C. Wendt *Private conversation and Calculation which models the muon spectrum from a monochromatic pion beam*